Doctoral Dissertation
Doctoral Program Material Science and Technology (38th Cycle)

Design of advanced biobased photocurable formulations: from dynamic covalent network to composite scaffold for tissue engineering

Matteo Bergoglio

* * * * * *

Supervisors

- Prof. Marco Sangermano, Supervisor, Politecnico di Torino, Department of Applied Science and Technology, Torino, Italy
- Prof. Marta Miola, Co-Supervisor, Politecnico di Torino, Department of Applied Science and Technology, Torino, Italy

Doctoral Examination Committee

- Massimo Messori
- Jesus Cristian Mendes Felipe
- Federico Davide Costantino Mussano

Politecnico di Torino
2026

This dissertation is presented in partial fulfillment of the requirements for **Ph.D. degree** in the Graduate School of Politecnico di Torino (ScuDo)

I hereby declare that, the contents and organisation of this dissertation constitute my own original work and does not compromise in any way the rights of third parties, including those relating to the security of personal data.

Matteo Bergoglio

Torino, 2026

Acknowledgment

I would first like to acknowledge Professor Marco Sangermano, who has supported me from the very beginning of my master's thesis and continued to extend his trust and guidance throughout my PhD journey. He always encouraged me to do more and allowed me to travel across and beyond Europe, making this PhD a truly international experience, from the small city of Leoben to the far reaches of Australia. Through these experiences, I've lived some of the most beautiful moments of my life so far. Thank you, Marco.

A special acknowledgement goes to Professor Marta Miola, my co-supervisor, who guided and supported me, both in the lab and beyond.

I would also like to thank my Austrian colleagues, David, Ellie, Szymon, Walter, Katia, Rita, Alex, and many others, as well as Professors Sandra Schlögl and Thomas Griesser, who made the Austrian experience possible and warmly welcomed me into their lab.

A warm thanks also to Professor Neil Cameron, who made my Australian experience possible and made me feel at home by hosting and supporting me on the other side of the world. Thanks as well to Saarthak, Sadjad, Jeremy, and Cintia. The Australian period was truly special, not only for the research but also because I met my Italian-Australian friend, Matteo, one of the best friendships I've ever had, born in such a short time with someone surprisingly similar to me.

Then come all my lifelong Italian friends: Paolo, Silvia, Lurens, Liuke, Pif, Andre, Bene, Manu, Ale, and Michi, who have shared this journey with me before and after childhood.

My colleagues also played a crucial role in my path: Michael, Lore, Christian, Ross, Dumi, Mati, and Albi. Thank you for the great time spent together in the lab and in the office.

Thanks to my two little sisters, Greta and Sofia, and to all my family, including Giulia's family. A special thanks goes to my parents, who have always encouraged me to do my best and supported me through every phase of my life, even and especially when I didn't ask for it.

The same gratitude goes to my grandparents, Nonna Carla and Nonno Ferruccio, as well as Nonna Onesta and Nonno Antonio. Some of them are no longer with me, but their lessons and love remain. Thank you, nonno Ferruccio, for teaching me grace and patience, and thank you, nonno Antonio, for the invaluable moments we shared. You will always be in my heart.

Finally, thank you to Giulia. You were always there for me, supporting me through everything. Thank you for all the moments we've shared and for those still to come.

Summary

The transition towards sustainable materials has become a global priority, driven by environmental concerns, restrictive laws, and the increasing demand for high-performance systems that minimise their ecological footprint. Thermosets, although widely used in industrial and biomedical fields due to their excellent stability and mechanical properties, suffer from different limitations: their permanent crosslinked structure prevents reprocessing, while their fossil-based origin poses an additional challenge to sustainability. This thesis was elaborated to address these challenges through the design of bio-based, UV-curable, and reprocessable polymer networks tailored for industrial and biomedical applications.

The work is organised into two main research subjects. The first part focuses on bio-based dynamic polymer epoxy networks derived from epoxidised castor oil. By employing a transesterification catalyst, covalent adaptable networks (CANs) were obtained. These materials preserved the high mechanical properties of traditional thermosets while introducing dynamic bond exchange reactions that enabled reprocessing, reshaping, and recyclability, aligning with circular economy principles. Their properties were further enhanced through the incorporation of multiwalled carbon nanotubes (MWCNTs), which imparted electrical conductivity and improved mechanical stability. The resulting composites not only maintained high bio-based content but also offered multifunctionality, with potential applications in coatings, conductive adhesives, and structural components where repairability and performance are equally required.

The second research line shifted the focus towards biomedical applications, where sustainability was integrated with bioactivity and functionality. The initial studies explored chitosan-based hydrogels reinforced with tellurium-doped and silanized bioactive glasses (BGs). These systems combined the natural

biocompatibility of chitosan with the osteoconductive, antioxidant, and antimicrobial properties of modified bioactive glasses (BGs), creating promising candidates for soft and hard tissue regeneration.

Building upon this basis, the work advanced towards the fabrication of highly porous scaffolds using high internal phase emulsion (HIPE) templating and UV-induced thiol–ene photopolymerization of acrylated epoxidised soybean oil (AESO) with Trimethylolpropane tris(3-mercaptopropionate) (TMPTMP). The obtained polyHIPE scaffolds exhibited a highly interconnected open-cell morphology, closely resembling cancellous bone and thus well-suited for tissue engineering. The incorporation of bioactive glasses enabled the modification of both mechanical properties and biological performance, providing improved osteointegration. In parallel, the use of additive manufacturing provided control over scaffold architecture, allowing the production of customised 3D-printed constructs with tunable porosity gradients and patient-specific geometries.

Moving forward, the systems used shifted to AESO-based scaffolds 3D printed and reinforced with different compositions of bioactive glasses. The BGs were first doped with Cu and Te to provide angiogenic and antimicrobial properties, and then were silanized to enhance the interface with the polymeric matrix. Every work provided a closer look at the properties of each formulation with different BG quantities and types, analysing how the properties changed when varying elemental composition and component quantity.

The final stage of the thesis integrated the two research lines by introducing reprocessing functionality into AESO-based scaffolds, also in this case, BG reinforced. This work merged biodegradability, bioactivity, and reprocessability into a single system, demonstrating that the principles of covalent adaptable networks can be extended to the biomedical field.

In conclusion, this thesis exposed how the combination of renewable monomers, dynamic covalent chemistry, functional fillers, and advanced fabrication methods can yield thermosets and scaffolds that are simultaneously sustainable, high-performing, and application oriented. The reprocessable composites with covalent adaptable networks and the bioactive scaffolds for tissue engineering exemplify how biobased products can be utilised in practical solutions across diverse sectors.

Overall, the outcomes of this work highlight that sustainability and materials for specific applications are not mutually exclusive, but rather complementary drivers for future studies in polymeric materials.

Contents

List of Tables

List of Figures

Chapter 1: Introduction

Modern society is deeply linked with polymeric materials, which are essential in a wide range of applications, from textiles and aerospace composites to life-saving medical devices and high-performance electronics. Despite increasing attention toward the environmental impact of these materials, global polymer production continues to rise, as shown in Figure 1.

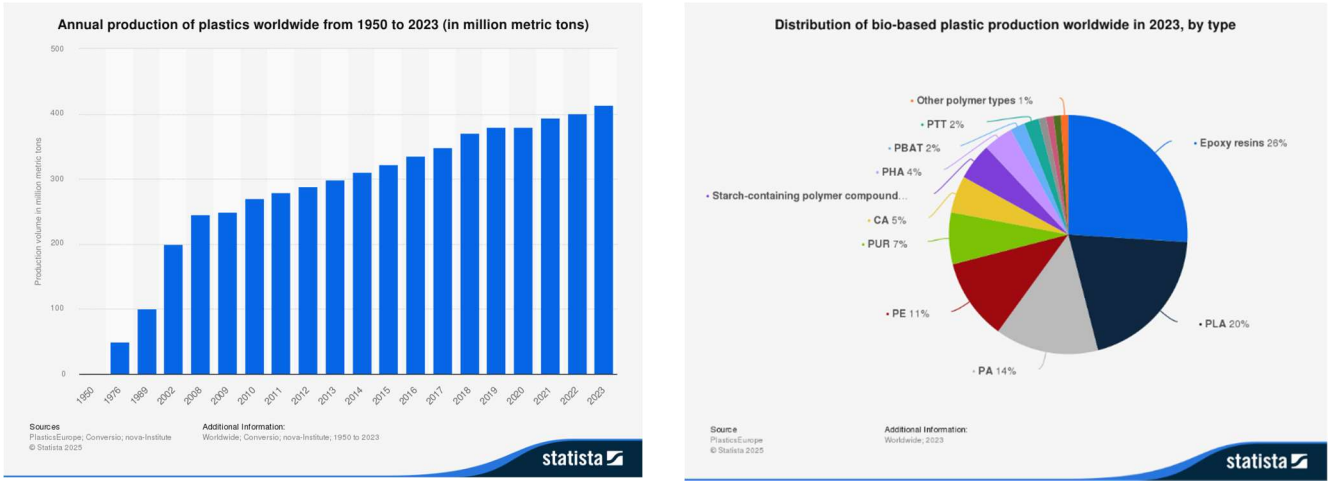

(a) (b)

Figure 1. (a) Global production of polymeric materials from 1950 to 2033 [1]. (b) Distribution of bio-based plastic production worldwide in 2023, by type [2].

The majority of these polymers are derived from petrochemicals, but their use remains widespread since many of them contribute to an improved quality of life, and the cost of production is still lower than that of alternatives.

However, the continued reliance on fossil-based resources and the need to replace them have encouraged researchers and industries to explore more sustainable alternatives. One of the most promising strategies is the development of bio-based polymers, produced from renewable biomass feedstocks, and designed to be either recyclable or biodegradable.

These "bioderived" or "bio-based" polymers are derived from plant biomass, but the shift to such alternatives is still limited by several challenges. For instance, not all bio-based polymers are biodegradable, and many suffer from high production costs and insufficient thermo-mechanical properties. As a result, only a

small fraction of the global polymer output is currently bio-based, just 1.7 megatonnes out of over 300 megatonnes produced in 2014, with polyethene terephthalate (PET), polyethene, and polylactide representing the largest shares [3].

Nowadays, the bio-based polymer industry has focused primarily on thermoplastics, materials composed of long polymer chains held together by non-covalent interactions. In contrast, bio-based thermosets, which are formed via permanent covalent crosslinks, have received less attention and remain a small fraction of both research and commercial markets, as illustrated in Figure 1b. However, bio-based thermosets hold great promise, particularly for high-value applications that demand advanced performance, such as structural composites or electronics, where economics are more favourable than in commodity uses like packaging, for which thermoplastics are used [4].

The nature of the bio-based feedstock is crucial in determining both the industrial viability and the properties of the resulting thermosets. Among renewable resources, triglyceride-rich vegetable oils are especially attractive due to their abundance and chemical functionality. The four most commonly used oil crops, soybean (Glycine max), oil palm (Elaeis), oilseed rape (Brassica napus), and sunflower (Helianthus), are produced on a massive scale, yielding about 156 megatonnes in 2012. While the majority is consumed as food, around 30 megatonnes are used for biofuels and another 20 megatonnes as chemical feedstocks [5]. Oils are composed of triglycerides, which consist of three fatty acids linked via ester bonds to a glycerol backbone. Although they are present in nearly all plant oils, their composition and yield vary significantly across plant types. For example, soybeans typically yield only about 20 wt% triglycerides. Furthermore, the chemical diversity of the fatty acids within a given crop adds complexity but also opportunity: the structural variety enables modification of polymer properties, making triglycerides a versatile platform for bio-based monomer synthesis. Castor oil is another particularly valuable biomass source due to the presence of a secondary hydroxyl group within its fatty acid chains, which facilitates efficient functionalization and polymerisation.

In this thesis, two key bio-based monomers are employed: acrylated epoxidised soybean oil (AESO) and epoxidised castor oil (ECO), whose chemical structures are presented in Figure 2.

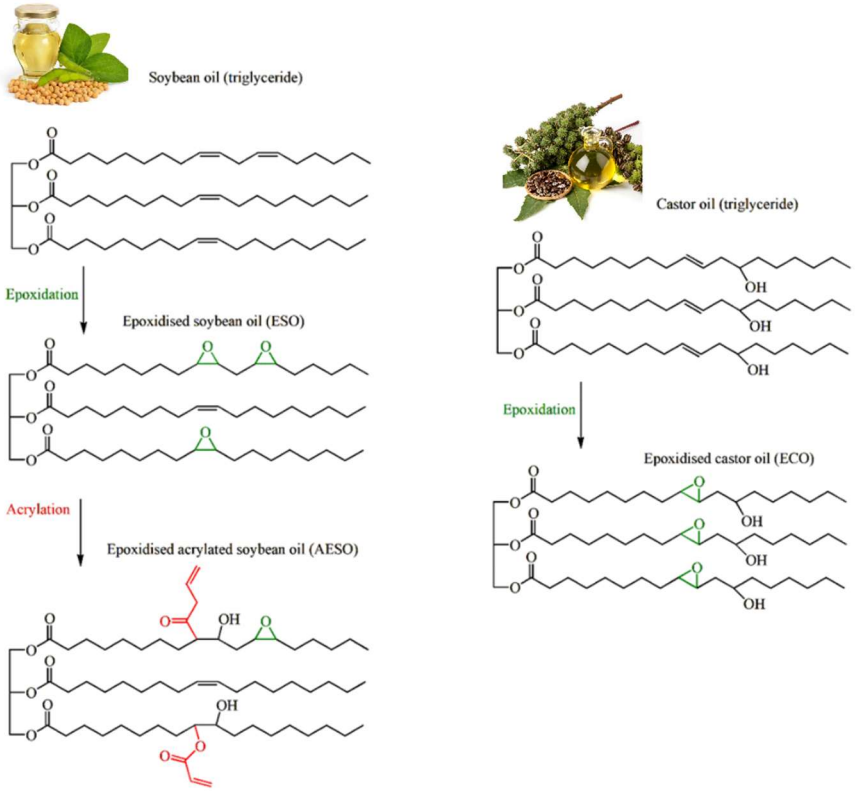

Figure 2. Chemical structure of expoxidised acrylated soybean oil and epoxidised castor oil.

Although triglycerides are found in almost all plants, the quantity available varies, and even crops such as soybeans are estimated to yield only 20 wt% of triglycerides. Another challenge is that the chemical compositions of triglycerides vary both between and within a particular crop. Triglycerides are composed of three, often distinct, fatty-acid groups that are linked together through ester bonds to a glycerol unit.

Despite the challenges associated with variable feedstock quality and composition, fatty acids derived from triglycerides present interesting opportunities in the design of advanced polymers. For instance, recent developments have shown that fatty-acid-based monomers can be used to create reprocessable thermosets, also called vitrimers, a class of polymers with dynamic covalent bonds that enable thermoset to thermoplastic transitions properties under thermal stimuli, which activate peculiar reactions, such as transesterification reactions [6,7]. This dynamic behaviour opens the door to reprocessable, repairable, and recyclable thermosets.

The development of high-performance, bio-based thermoset polymers remains a significant challenge for both academia and industry. Unlike thermoplastics, thermosets require liquid monomers or oligomers with multiple reactive sites that

undergo crosslinking, typically triggered by heat or light, to form a permanent, insoluble network. Among various curing strategies, photocrosslinking stands out as the most environmentally friendly option due to its fast curing rates and low energy consumption [8,9]. Building upon these advantages, this thesis focuses on the design and synthesis of UV-curable, bio-based thermoset polymers and composites derived from renewable resources such as AESO and ECO. Through this approach, the aim is to develop sustainable materials with tailored properties suitable for coating and tissue engineering applications while addressing the need for greener alternatives to conventional thermosets.

1.1 Photocuring processes

Ultraviolet (UV) light offers a highly efficient and environmentally friendly method for producing thermoset networks directly from resin formulations. In these systems, small amounts of photoinitiator (PI), a molecule which absorbs UV light and generates a reactive species that is transferred to the monomer resin, absorb a photon and are promoted from their electronic ground state (S_0) to a short-lived excited singlet state (S_1). From S_1, the photoinitiator can return to S_0 either by emitting fluorescence, undergoing non-radiative decay, or by undergoing intersystem crossing and therefore entering a longer-lived triplet state (T_1). In the excited states, the PI may fragment (bond-breaking) or otherwise rearrange to yield highly reactive radicals or ionic species, which in turn trigger chain-growth or step-growth polymerisation, forming an interconnected and crosslinked network [10].

The primary photochemical events, whether isomerisation [11,12], [2+2] cycloaddition [13,14], or bond cleavage [15–17], are all manifestations of one-photon adsorption (OPA), as shown in the Jablonski diagram [18].

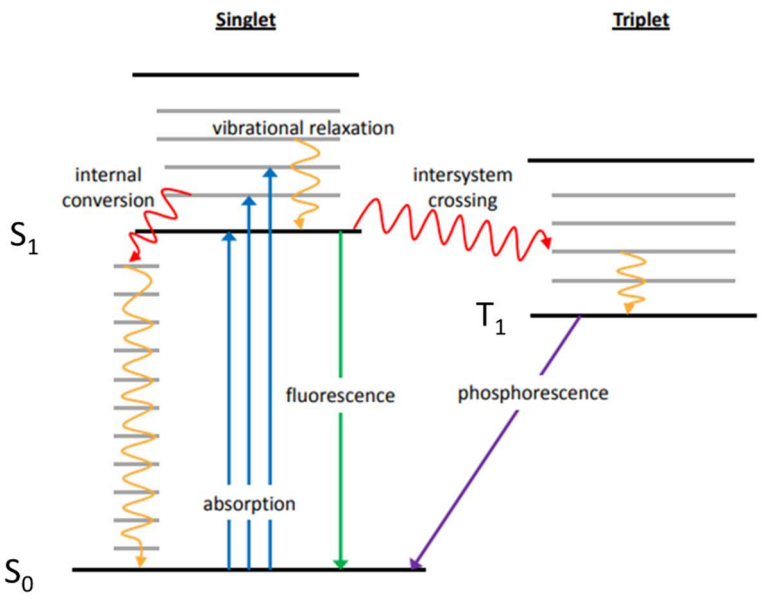

Figure 3. Jablonski diagram representation. Radiative transitions are represented by continuous lines, while non-radiative transitions by wavy lines.

A PI performance relies on key photophysical parameters: a strong molar extinction coefficient at the irradiation wavelength, a high quantum yield for reactive species generation, and an excited-state lifetime long enough to effect bond cleavage but short enough to minimise quenching by oxygen or other additives. As soon as the PI absorbs light and enters an excited state, competing quenching pathways, the energy transfer to other formulation components or oxygen, must be minimised. Therefore, careful selection of both photoinitiator chemistry and curing wavelength (UV vs. visible light) is essential to maximise light penetration, initiation rate, and uniformity of cure throughout the resin layer.

Over the past few decades, photopolymerization has become a fundamental technique, especially in the industries of coatings, adhesives, dental, and microelectronics. Its spreading is due to the exceptionally rapid curing rates, usually completed within a few seconds under moderate UV light exposure, combined with room-temperature processing, negligible volatile organic compound (VOC) emissions, and low overall energy demand [19]. These environmental and productivity advantages pushed the adoption of solvent-free, UV-curable formulations.

When radicals are generated (radical photopolymerization) or when cationic or acid species form (cationic photopolymerization), these reactive centres attack monomer units like acrylate, epoxy, or other polymerisable functionalities, propagating the crosslinking reaction until a solid thermoset is obtained [20].

Radical UV curing can proceed through either a chain-growth or a step-growth mechanism. The chain growth mechanism typically employs acrylate or methacrylate chemistries, offering rapid kinetics that endorse the acrylate double bond. The PI used in this type of reaction are aromatic ketone photoinitiators, which can undergo fast homolytic cleavage upon UV exposure, generating free radicals that will initiate the polymerisation following a Norrish I mechanism, represented in Figure 4.

One of the main limitations of radical photopolymerization is its sensitivity to oxygen inhibition, which is particularly problematic for high-surface-area applications such as coatings. Oxygen readily reacts with the propagating radicals, forming relatively unreactive peroxy radicals that effectively terminate chain growth and hinder the formation of a network. Several strategies have been developed to mitigate this issue, such as using an inert atmosphere during UV curing (e.g., nitrogen or argon), increasing the concentration of the photoinitiator or the intensity of the light source to accelerate polymerisation and overtake oxygen diffusion, and applying physical barriers, such as water or a wax layer, to block oxygen from reaching the reactive surface [21–23].

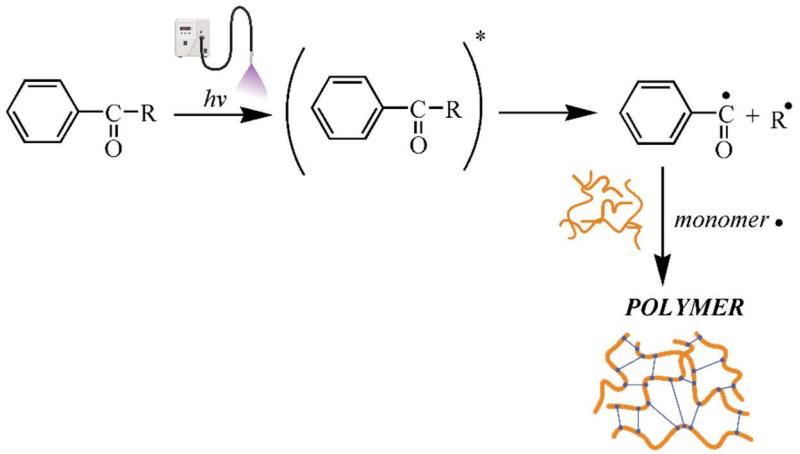

Figure 4. Photoinitiation of a radical-type polymerisation.

On the other hand, the step-growth mechanism involves mainly the thiol-ene "click" reactions, which are a coupling interaction between a thiol and an alkene to form an alkyl sulphide. After UV irradiation, the PI forms a thiyl radical, which propagates by addition to the unsaturated alkene substrate, and the formation of a carbon-centred radical intermediate. After this step, polymerisation can follow two mechanisms: the radical carbon can extract a hydrogen from a thiol, giving a chain transfer, or it may attack a similar alkene, leading to homopolymerisation. The

scheme is reported in Figure 4. The choice of pathways depends on both the nature of the alkene and the carbon-centred radical intermediate [24–27].

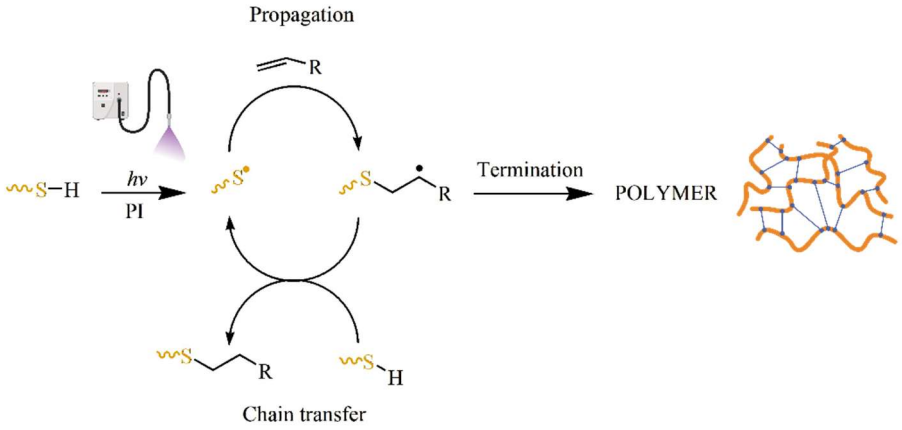

Figure 5. Propagation and chain transfer steps of thiol-ene click reaction.

Cationic UV-curing, commonly used with epoxy resins, proceeds via acid generation and is largely immune to oxygen quenching, though it may require longer induction periods [28]. It possesses diverse advantages, such as post-polymerisation in the dark, low shrinkage, high mechanical performance of the cured material, and good adhesion on various substrates, including metals. The photoinitiated cationic polymerisation has been investigated thoroughly over the past decades, especially by Crivello et.al, who pioneered this technology by developing triarylsulfonium and diaryliodonium photoinitiators, as well as appropriate photosensitizers [29–35]. The reaction scheme is reported in Figure 6.

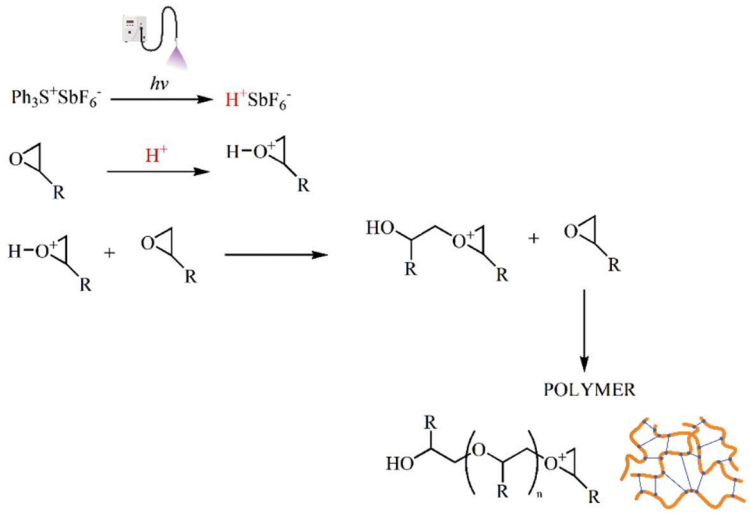

Figure 6. Cationic photopolymerisation reaction starting from a sulfonium-based photoinitiator.

In all cases, UV curing stands as the most sustainable curing technology available, enabling the production of high-performance thermosets with minimal environmental impact.

1.2 UV curing applied to additive manufacturing

Additive manufacturing (AM) processes enable the fabrication of complex structures through 3D printing, often with significant material savings compared to traditional manufacturing techniques. For this reason, both research and industry are increasingly implementing AM as a preferred production method [36–38].

AM technologies are generally categorised into seven main groups: vat photopolymerization (VP), material extrusion, powder bed fusion, material jetting, binder jetting, directed energy deposition, and sheet lamination (Figure 7).

Figure 7. Seven main groups of AM technologies.

Among these, vat photopolymerization stands out for its use of UV light to cure resin layer by layer, and it is further divided based on the light source into stereolithography (SLA), digital light processing (DLP), two-photon polymerisation (2PP), and volumetric 3D printing [39].

Two-photon polymerisation (2PP) offers exceptional spatial control and high resolution. It utilises near-infrared (NIR) femtosecond laser pulses, during which two photons are absorbed simultaneously by a photoinitiator. This event mimics the effect of a single energy photon, initiating polymerisation at a precise focal point within the resin. As a result, 2PP allows for the direct writing of complex 3D architectures deep within photosensitive materials that are transparent to NIR and highly absorptive in the UV range [40–42].

Volumetric 3D printing, differently, enables the creation of entire objects in three dimensions. This method involves a rotating vat filled with an index-matched resin and the projection of six distinct views of the target object from specific angles. By rapidly cycling these views during rotation, the full 3D geometry is formed simultaneously throughout the resin volume [43–45]. However, these first two methods bring drawbacks: 2PP offers superior control and higher resolution compared to SLA or DLP, but it is slower, while volumetric 3D printing requires more resin to effectively print with respect to a layer-by-layer method, and both methods require machines that are still expensive. For these reasons, SLA and DLP methods remain the most widely adopted techniques.

SLA and DLP both rely on layer-by-layer curing of photosensitive resins via UV light, but they differ in their exposure mechanisms. SLA uses a focused laser beam to cure the resin point by point, while DLP projects the entire layer at once using a digital micromirror device (DMD). This allows DLP to achieve faster printing speeds than SLA [46–48]. Moreover, the light sources used in DLP have evolved from conventional lamps to energy-efficient light-emitting diodes (LEDs), which offer broader spectral coverage and reduced operational costs [49].

To further reduce manufacturing costs while maintaining resolution, masked stereolithography (mSLA) has emerged as a promising alternative. mSLA follows the same working principle as DLP but replaces the DMD with an LCD panel that selectively blocks UV light, enabling the curing of only the desired areas of each layer [50,51]. A schematic representation of the different methods is shown in Figure 8.

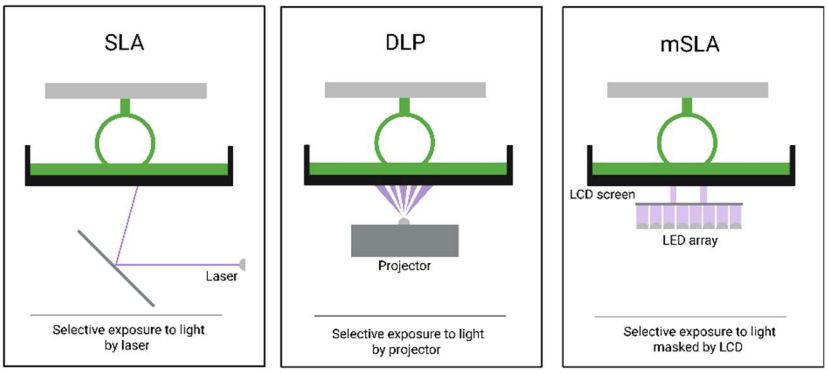

Figure 8. Principal vat photopolymerisation methods with their characteristics.

Various thermosetting polymers can be used in these processes, relying either on cationic photocuring via epoxy ring opening [48,49] or radical polymerisation using acrylate groups [50]. In particular, vegetable oils have gained attention in AM due to their high content of double bonds and hydroxyl groups, which can be readily converted into acrylate or epoxy functionalities. These biobased precursors have been used to fabricate a wide range of materials, including scaffolds for tissue engineering applications [52–55]. Among them, acrylated soybean oil has shown particular promise, thanks to its reactivity, biodegradability, and availability [54,56–60].

Tissue engineering (TE) is one of the most promising fields for applying mSLA technology. TE requires biomaterials with highly tunable physicochemical properties tailored to the target tissue. For instance, the liver, as a soft tissue, benefits from materials with low stiffness that allow flexibility and deformation to replicate its native mechanical behaviour. Cartilage, a medium-hard tissue, requires a balance between cushioning and structural integrity, with compressive Young's moduli typically ranging from 0.1 MPa to 1 GPa, depending on the type and location. Specifically, articular cartilage exhibits moduli between 0.3 and 30 MPa, with ultimate strains ranging from 9% to 40% [61]. Using mSLA, it is possible to meet patient-specific shape requirements and achieve precise control over scaffold geometry and porosity. This technique enables the fabrication of custom implants that conform to complex, irregular defects, enhancing scaffold–tissue integration while eliminating the need for expensive moulding or tooling processes.

1.3 Focus of the thesis

Inspired by the promising results achieved through UV curing and its associated manufacturing techniques, this thesis aims to design and develop novel bio-based

resin formulations derived from renewable monomers, with the main objective of promoting sustainability in thermoset manufacturing.

The work is organised into thematic chapters, starting from biobased reprocessable thermosets employing dynamic covalent networks, and progressing to biobased composite scaffolds intended for tissue engineering applications.

The first thematic chapter (Chapter 2) focuses on the development of reprocessable resins by means of covalent adaptable networks (CANs). The bio-based monomer used as the starting material was epoxidized castor oil. By taking advantage of the hydroxyl and ester groups already present in its chemical structure, and introducing a transesterification catalyst, the transesterification reaction could be activated, imparting reprocessing capabilities to the material. Building on this system, a reprocessable composite was produced using multi-walled carbon nanotubes (MWCNTs). This composite system enabled the fabrication of coatings with enhanced functionalities, including electrical conductivity.

The second thematic chapter (Chapter 3) shifts the focus to the formulation of composite materials for tissue engineering. In this context, bio-based monomers were combined with bioactive glasses synthesised via the sol–gel method and chemically functionalised to improve biological performance and compatibility. The work began with the fabrication of a composite hydrogel using chitosan as a bio-based polymer. This hydrogel was loaded with tellurium-doped, silanised bioactive glass particles to provide a dual function: antimicrobial activity from the Te-doping and osteoconductivity from the bioactive glass itself.

In the transition from soft to rigid tissue engineering platforms, polyHIPEs (high internal phase emulsions) were introduced. The starting monomer in this case shifted to acrylated epoxidized soybean oil (AESO), which was combined with trimethylolpropane tris(3-mercaptopropionate) (TMPTMP) to undergo a thiol–ene reaction, producing a sponge-like material with extremely high porosity. As before, the material was filled with bioactive glass to produce a composite scaffold, which was then successfully 3D printed.

Finally, AESO was also employed as a single bio-based monomer in the final set of projects. In this platform, AESO was combined with a reactive diluent to reduce viscosity and enable 3D printing. Three different formulations were developed: the first reinforced with SiO_2-CaO-P_2O_5 based bioactive glass; the second with Cu-doped, silanised bioactive glass; and the third with Te-doped, silanised bioactive glass. In the concluding work, the transesterification chemistry introduced in Chapter 2 was integrated into the AESO-based composites, imparting reprocessability to the 3D-printed scaffolds. This final development bridges the two main research themes of the thesis, bonding the design principles of bio-based

reprocessable thermosets with the functional requirements of scaffolds for tissue engineering.

Chapter 2: Biobased Covalent Adaptable Network (CANs)

Paper I: Sustainable Bio-Based UV-Cured Epoxy Vitrimer from Castor Oil

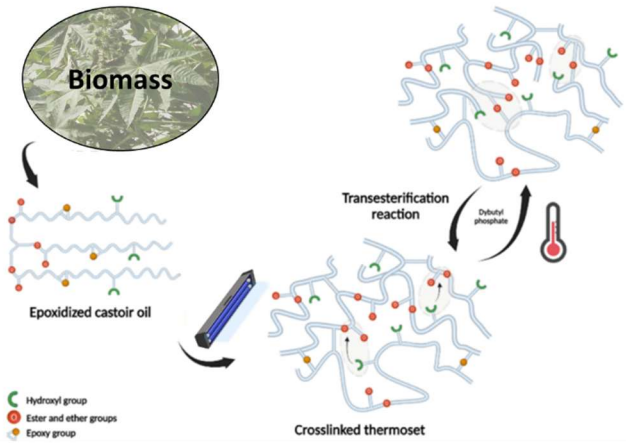

Paper II: Cationic UV-curing of bio-based epoxidized castor oil vitrimers with electrically conductive properties

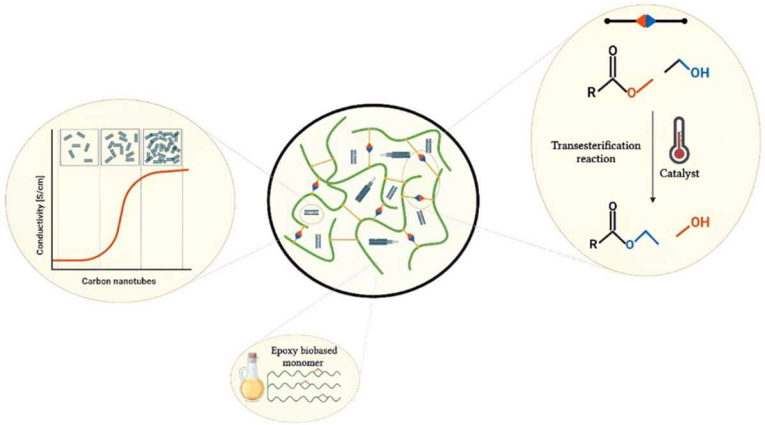

Review I: Biobased Vitrimeric Epoxy Networks

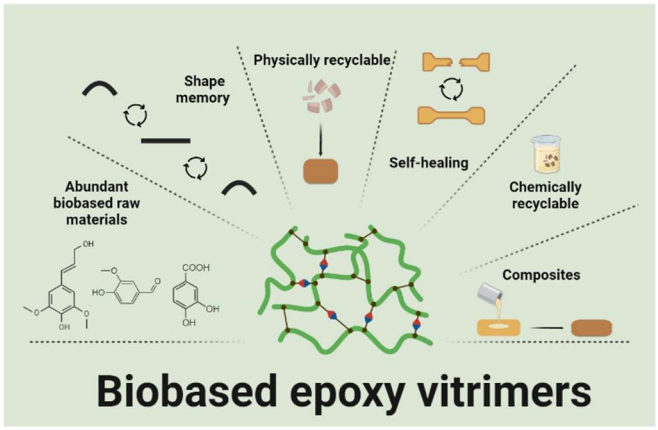

2.1 Introduction

Covalent Adaptable Networks (CANs) consist of permanent crosslinked polymeric networks that include in their structure reversible covalent bonds. The reversibility of the covalent bonds allows the network to rearrange in response to an external stimulus, such as heat or light, while still maintaining the network intact [62,63]. These "smart" materials act as a bridge between thermosets and thermoplastics, as they exhibit unusual properties, such as recyclability, self-healing, and shape change, not found in traditional thermosets (Figure 9). This allows these materials to possess the high-performance properties typical of thermoset and the reprocessability typical of thermoplastic. Bowman et al. formally introduced the term CANs in 2010 to describe this new class of materials [62].

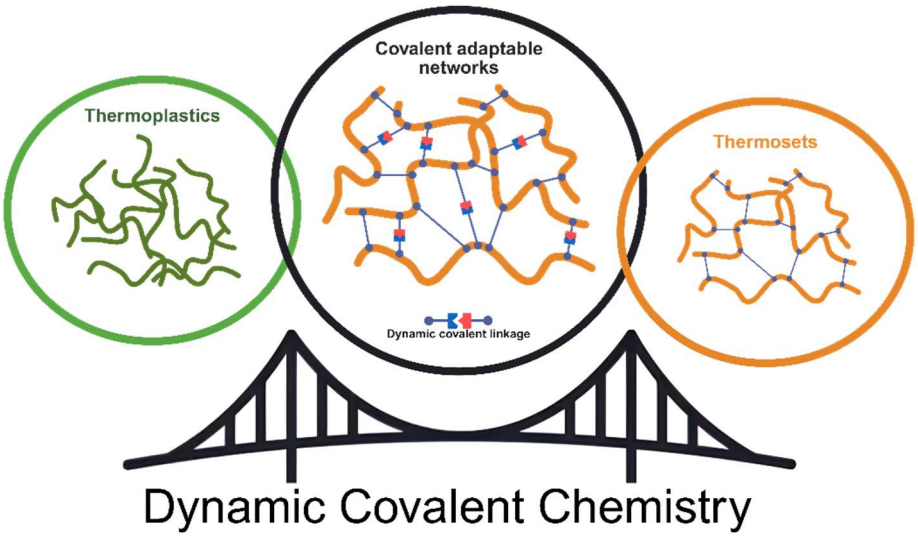

Figure 9. Visual representation of the concept of covalent adaptable networks.

When a CAN is heated well above its glass transition temperature (T_g), its viscosity becomes controlled by the kinetics of thermally activated bond-exchange reactions, causing the material to follow an Arrhenius-type dependence on temperature. Whether the topology-freezing temperature (T_v) lies above or below T_g determines the material's mechanical response, as shown in Figure 10. If T_g is lower than T_v, the network behaves like a classic thermoset until T_g, at which point it undergoes to a rubbery transition. Only when the T_v is exceeded, the bond exchanges become sufficiently rapid to allow the polymer to flow as a viscoelastic

liquid. On the contrary, if T_g exceeds T_v, exchange reactions are already active as soon as the polymer softens above T_g, and the material transitions directly from a glassy solid to a viscoelastic liquid, initially following Williams–Landel–Ferry behaviour before settling into Arrhenius-type kinetics. In either scenario, temperatures above T_v bring the characteristic exchange timescale below the experimental observation window, so that stress relaxation is nearly complete despite the permanent network connectivity. Below T_v, the network appears effectively frozen and responds as an ordinary viscoelastic solid. By convention, T_v is taken to be the temperature at which the zero-shear viscosity reaches 10^{12} Pa·s, a definition originally proposed by Leibler and co-workers [64]. Stress-relaxation measurements remain the most accurate means to determine T_v: the relaxation modulus G(t) decays exponentially according to the formula:

$$\frac{G(t)}{G_0} = e^{\frac{-t}{\tau}}$$

where τ is the time required for G(t) to decrease to 1/e of its initial value G_0. Plotting ln τ versus 1/T yields a straight line if the exchange mechanism obeys Arrhenius kinetics, as expected for associative vitrimeric networks, which will be discussed shortly.

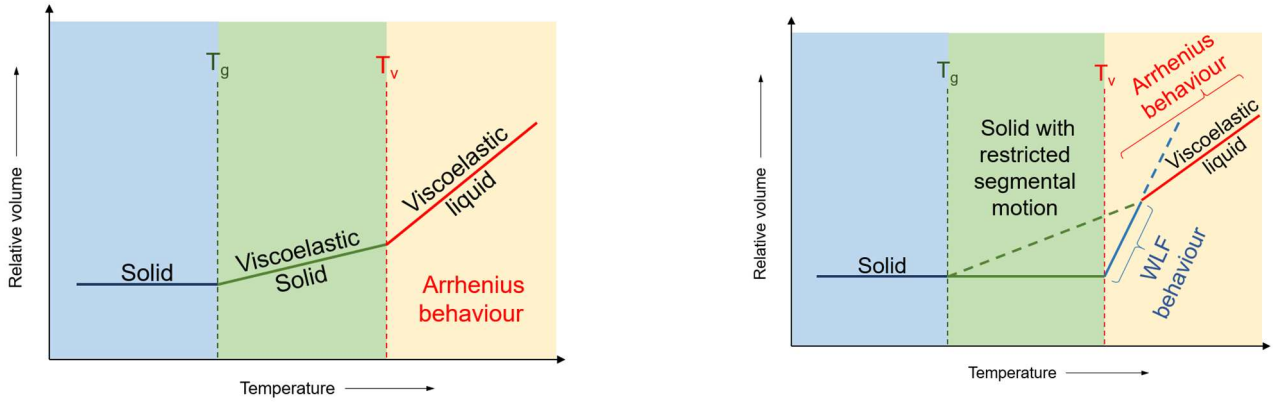

a) b)

Figure 10. Temperature dependence of the dynamic covalent network based on the value of the topology-freezing temperature (T_v). a) T_g below T_v and b) T_g above T_v.

The CANs can be tailored by selecting the reversible chemistry to activate them with the optimal catalyst. The reversible covalent bonds are typically designed to break and reform without losing the overall network connectivity. This can happen via an associative mechanism, where bond exchange occurs by exchanging moieties while maintaining a constant crosslinking, or a dissociative mechanism, where bonds temporarily break completely. In the associative CANs, the crosslinking

density remains fixed during the exchange, so the viscosity decreases with the temperature in an Arrhenius-like behaviour. Leibler et al. coined the term “vitrimer” for associative CANs that possess the Arrhenius behaviour, activated by a transesterification reaction [64]. On the other hand, in dissociative CANs, the bonds fully dissociate at high temperature, but the network reforms upon cooling.

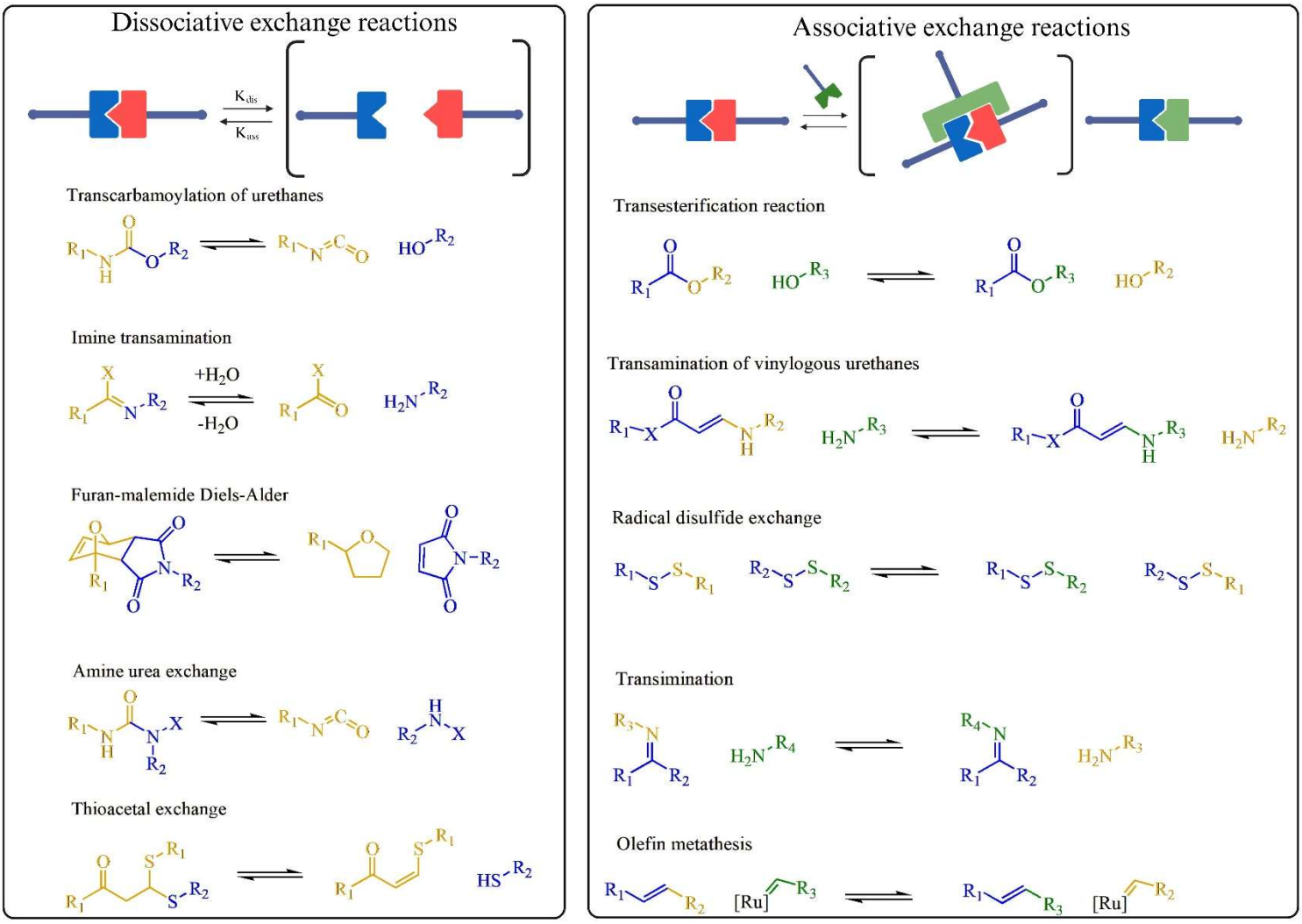

Figure 11. Principal exchange reactions used in the Covalent adaptable network design.

A wide variety of reversible covalent reactions have been employed in CANs.

Disulfide exchange represents another associative mechanism, in which a thiol group attacks a disulfide bond, cleaving and reforming it to bring a new disulfide linkage. This reaction occurs under mild conditions and often does not require external catalysis, making it attractive for UV-curable vitrimer systems [65–70]. Other examples of associative exchange reactions include imine and acetal chemistries, which operate through reversible condensation processes typically

triggered by thermal or acidic stimuli [71–73]. Additional mechanisms such as transcarbamoylation, transimination, and olefin metathesis have also been studied in tailored vitrimeric systems to enhance specific functionalities or thermal profiles [74–81]. Among all the mechanisms, transesterification (ester-hydroxyl group exchange) represents the classic associative mechanism. An ester and a hydroxyl group within the network exchange the moieties, usually catalysed by acids or bases. This is one of the most extensively studied exchange processes in epoxy networks. For instance, adding a catalyst triggers a transesterification reaction starting from 70-100°C, allowing stress relaxation in our work [63,82]. In contrast, dissociative CANs rely on thermally reversible reactions that lead to a temporary decoupling of the network. A typical example is the Diels–Alder reaction, which allows bond cleavage at elevated temperatures and reformation upon cooling, making it suitable for self-healing applications [83,84].

A promising application of covalent adaptable networks is in UV-curable thermoset coatings capable of reprocessability. Conventional UV-cured epoxy coatings form rigid, solvent-resistant films that cannot be reshaped or repaired once crosslinked. By incorporating dynamic covalent bonds into the resin, as explained in the previous systems, it is possible to obtain coatings that cure under UV to form a mechanically robust thermoset. At the same time, these coatings can be subsequently reheated to enable bond exchange, healing, or recycling. Furthermore, most commercial thermosets rely on petroleum-derived monomers, which do not meet sustainability goals; replacing these with bio-based monomers addresses both circularity and environmental impact. [85,86]

There is extensive recent literature on the use of bio-based monomers for CANs synthesis [87–89]. Among these, castor oil has attracted particular attention because its triglyceride backbone possesses ester and hydroxyl groups, both essential for the transesterification reaction, while its non-conjugated C=C bonds are too unreactive to undergo radical polymerisation without prior modification. Consequently, castor oil has been functionalized with epoxy, amine, and methacrylate groups in many studies to tailor network chemistry and mechanics [90–94]. Epoxidised castor oil (ECO) is typically prepared in high yield by reacting castor oil with a formic acid/H_2O_2 system, a process noted for its simplicity and cost-effectiveness [95].

In our work, we utilised epoxidised castor oil (ECO), a biobased epoxy monomer, to design a reprocessable UV curing formulation, thanks to the presence of a transesterification catalyst. The result was a solvent-free biobased vitrimeric network. The resin cured rapidly under UV at low temperature, and the cured coating could undergo thermo-activated bond exchange thanks to dibutyl phosphate. In stress-relaxation tests, these ECO-based coatings exhibited the onset

of transesterification around 170 °C, demonstrating reprocessability behaviour starting from that temperature. Once the reprocessability and transesterification reaction activation were defined, we added a conductive functionality to the system by embedding multiwall carbon nanotubes (MWCNTs) using the same bio-based material that had been previously developed and studied.

2.2 Experimental section

2.2.1 Materials and chemicals

Epoxidised castor oil (ECO), employed as the primary bio-based monomer for network formation, was supplied by Specific Polymers (France). Dibutyl phosphate (DP), utilised as a transesterification catalyst to enable dynamic covalent bond exchange within the vitrimeric network, and triarylsulfonium hexafluorophosphate salt (THS), acting as a cationic photoinitiator for UV-induced polymerisation, were both purchased from Sigma-Aldrich (Milan, Italy). The conductive nanofiller, multi-walled carbon nanotubes (MWCNTs, grade NC3100), characterised by an average diameter of 9.5 nm and a length of approximately 1.5 μm, was kindly provided by Nanocyl S.A. (Belgium) and incorporated to impart electrical functionality to the reprocessable matrix.

2.2.2 Procedures
Resin formulation and UV curing

In the initial stage of the project, the bio-based resin system was developed by combining epoxidised castor oil (ECO) with different amounts of cationic photoinitiator, triarylsulfonium hexafluorophosphate salt (THS) and varying concentrations of the transesterification catalyst, dibutyl phosphate (DP). The components were mixed in a GT ultrasonic bath (Guangdong, China) until complete homogenization, ensuring dissolution of all constituents. To prevent premature photopolymerization, the formulations were stored in the dark prior to being poured into silicone moulds and subsequently cured under UV light using a DYMAX ECE Flood lamp (Dymax Europe GmbH, Wiesbaden, Germany), with an intensity of 130 mW/cm² for 60 seconds.

Building on this formulation, composite networks were developed by incorporating multi-walled carbon nanotubes (MWCNTs, NC3100). To enhance dispersion, ECO was preheated to 50°C, and the MWCNTs were pre-dispersed in acetone before being added to the resin formulation, which also contained 2 phr of photoinitiator and 15 phr of transesterification catalyst. The mixture, comprising

ECO, THS, DP, and MWCNTs, was homogenised using an IKA T ULTRA-TURRAX mixer (Staufen im Breisgau, Germany) for 90 minutes under an ice bath to prevent thermal degradation. Subsequently, an additional dispersion step was conducted in a GT ultrasonic bath at 50°C for 2 hours to allow for the complete evaporation of acetone and to eliminate CNT agglomerates. Four formulations were prepared, including a pristine control and samples containing 0.1, 0.25, and 0.5 phr of CNTs. Each formulation was then poured into silicone moulds and UV-cured under identical conditions to the initial resin system.

Transmittance Fourier transform infrared spectroscopy (FTIR)

FTIR spectroscopy is a technique used to obtain the infrared absorption or emission spectrum of solid, liquid, or gaseous samples. It provides information on the bulk chemical properties of a material by irradiating the sample with infrared (IR) light and detecting the specific wavelengths absorbed by molecular bonds. The resulting IR spectrum acts as a molecular "fingerprint" of the material. A mathematical process known as the Fourier Transform is applied to convert the measured interferogram into a spectrum that displays absorption as a function of wavelength or wavenumber [96,97].

When used in transmittance mode, the sample is typically spread onto a transparent substrate, such as a silicon (Si) wafer, using a film applicator to achieve a uniform thickness (e.g., 32 μm). In this project, real-time transmission FTIR analysis was performed using a Nicolet iS50 spectrometer (Thermo Fisher Scientific, Monza, Italy). The Si-supported resin film was irradiated with UV light at 365 nm, and the evolution of epoxy conversion was monitored over time.

The epoxy group signal was tracked in the region between 755 and 800 cm^{-1}, using the C–H stretching peak at 2950 cm^{-1} as a reference, as it is considered unaffected by UV exposure. The epoxy conversion was calculated using Equation 1, based on the relative decrease in the absorbance of the epoxy band compared to the reference peak.

$$Conversion\ (\%) = \frac{(\frac{A_{group}}{A_{ref}})_{t=0} - (\frac{A_{group}}{A_{ref}})_{t}}{(\frac{A_{group}}{A_{ref}})_{t=0}} \times 100 \quad (1)$$

Where A group is the area of the selected group under investigation, and A ref is the reference area of the peak situated at 2950 cm^{-1}.

Photo dynamic scanning calorimetry (DSC)

The conventional DSC measures heat flow as a function of temperature to identify thermal transitions, such as the glass transition (T_g) or melting point (T_m). [98]

In this case, the DSC was operated isothermally at 25 °C to detect the heat released by the UV-induced polymerisation. This setup allows the quantitative evaluation of the photocuring kinetics and the total heat of reaction.

The photocuring behaviour of the resin formulations was investigated using photo-Differential Scanning Calorimetry (photo-DSC). The measurements were performed with a Mettler Toledo DSC-1 (Milano, Italy), equipped with a Gas Controller GC100 to ensure a constant nitrogen flow of 40 mL/min and a Hamamatsu LIGHTINGCURE LC8 mercury lamp (Hamamatsu Photonics), coupled with an optical fibre to precisely direct the radiation onto the sample. The UV light had a wavelength centred at 365 nm, with an irradiance set between 50 and 100 mW/cm², depending on the specific experiment.

For each measurement, 5 to 15 mg of the uncured formulation was placed in an open aluminium pan, while an empty open pan served as the reference. All tests were carried out at room temperature (25 °C) under a nitrogen atmosphere to prevent oxygen inhibition of the polymerisation process.

The photo-DSC method was designed to monitor the exothermic heat flow associated with the UV-induced crosslinking reaction of the resin. The protocol consisted of two consecutive irradiations, each lasting 120 s and preceded by a dark stabilisation period of 60 to 120 s to ensure thermal equilibrium before light exposure. The second irradiation was used to ensure complete curing and to identify and subtract any baseline signal not related to the polymerisation reaction. The net heat flow, corresponding to the exothermic reaction of interest, was obtained by subtracting the second scan from the first.

All data were processed and analysed using Mettler Toledo STARe software v9.2.

Dynamic mechanical thermal analysis (DMTA)

Dynamic Mechanical Thermal Analysis (DMTA) is a technique employed to investigate the viscoelastic behaviour of materials by applying a dynamic oscillatory force over a range of temperatures. The mechanical response of the material is characterised by two principal parameters: the storage modulus (E′), which quantifies the elastic (energy-storing) component, and the loss modulus (E″), which reflects the viscous (energy-dissipating) component. The loss factor,

expressed as the ratio of E″ to E′ and known as tan δ, provides information about the damping behaviour of the material. The temperature at which tan δ reaches its maximum is typically associated with the glass transition temperature (T_g) of the polymeric system [99,100].

In this study, DMTA tests were performed using a Triton Technology instrument starting from –20 °C (achieved using liquid nitrogen) up to 100 °C. A constant heating rate of 5 °C/min was applied. The primary objective of the analysis was to determine the glass transition temperature, corresponding to the peak of the tan δ curve. Samples for the test were prepared by pouring the photocurable resin into silicone moulds of defined geometry (0.5 × 7.5 × 17.5 mm or 0.5 × 3.5 × 12 mm) and curing each layer for 90 seconds under a DYMAX ECE Flood lamp (Dymax Europe GmbH) at an intensity of 130 mW/cm².

The crosslink density per unit volume (ν_c) was determined using **Equation 2.**

$$\nu_c = \frac{E'}{3RT}$$

Equation 2. crosslinking density formula.

Where E′ is the storage modulus measured in the rubbery plateau region (T_g+50 °C), T is the absolute temperature in Kelvin, and R is the universal gas constant.

Tensile measurements

Tensile testing is a fundamental method used to evaluate the mechanical behaviour of materials under uniaxial stress. The resulting stress-strain curves provide key information about the material tested, such as the elastic (Young's) modulus**,** tensile strength, and elongation at break**.** Specifically, the elastic modulus quantifies the stiffness of a material and is determined from the initial linear region of the curve, where the deformation is reversible and proportional to the applied stress. [101,102]

In this study, the mechanical properties of the UV-cured samples were verified using a universal tensile testing machine (MTS QTest™/10 Elite, MTS Systems Corporation, Eden Prairie, MN, USA) equipped with dedicated software (TestWorks® 4, MTS Systems Corporation). The tensile tests were performed at a constant crosshead speed of 5 mm/min, and the specimens had dimensions of approximately 2 × 5 × 50 mm**.**

The stress–strain curves obtained from the tests were analysed to extract the elastic modulus, calculated within the linear elastic region of the curve, typically up

to 15% deformation. To ensure statistical relevance and reproducibility, five replicates were tested for each formulation, and the results were reported as the average values of the measured mechanical properties.

Thermogravimetric analysis (TGA)

Thermogravimetric analysis (TGA) is a thermal analysis technique used to evaluate the thermal stability of a material by continuously recording the change in mass as a function of temperature over time, under controlled atmosphere. The technique allows the identification of thermal degradation steps, quantification of volatile content, and estimation of inorganic residue.

It is particularly useful for understanding polymer decomposition behaviour and the effect of fillers or additives on thermal stability. The first derivative of the mass loss curve (DTG) can also provide insight into the decomposition kinetics and help identify the temperatures at which the maximum degradation rates occur [103,104].

In this work, TGA was performed using a Mettler Toledo TGA/DSC1 (Milano, Italy) instrument equipped with aluminium oxide crucibles (70 µL) and operated under a nitrogen atmosphere. Approximately 10 mg of sample was placed in the crucible and heated from 25 °C to 800 or 850 °C at a constant heating rate of 10 °C/min. The nitrogen flow rate was maintained at 40 mL/min to ensure an inert environment and prevent oxidative degradation during the analysis. Thermal stability was evaluated based on the onset degradation temperature and the residual weight at the end of the test.

The results provided comparative information on the thermal resistance of the different UV-cured samples, particularly in relation to the chemical structure of the network and the presence of inorganic fillers such as carbon nanotubes.

Electric conductivity

Broadband dielectric spectroscopy (BDS) is a technique used to investigate the dielectric properties of materials across a wide frequency range. During the analysis, an alternating electric field is applied to a material, and its dielectric response is measured as a function of frequency.

In this work, broadband dielectric spectroscopy (BDS) was employed to investigate the electrical conductivity and dielectric response of the materials. Measurements were performed using a Novocontrol Alpha high-resolution dielectric analyser (Frankfurt, Germany), with an alternating voltage of 1.0 V

applied. Frequency scans were conducted in the range of 0.1 Hz to 10^6 Hz at room temperature.

Samples were prepared by hot-pressing thin polymer films between two gold-plated electrodes with a diameter of 20 mm, arranged in a parallel-plate configuration. The initial thickness of the sample was determined as the difference in the separation of the electrodes before and after insertion of the polymer film. For improved accuracy, this value was corrected by measuring the actual thickness of the film after it was removed from the electrodes at the end of the dielectric measurements.

Stress relaxation measurements

Stress relaxation experiments are used to study the time-dependent viscoelastic behaviour of polymers, especially those that exhibit adaptable covalent bonds. In a typical stress relaxation test, the material is subjected to a constant strain while the stress decreases over time at a constant temperature. This experiment allows the characterisation of the network mobility activated by the reversible bonds in the polymeric material. In materials that possess the ability to activate the covalent adaptable network, exhibit a gradual decrease in stress, measured as the relaxation modulus G(t) when a constant temperature, force and deformation is applied, indicating structural internal rearrangement [64,82,105–108].

In this work, stress relaxation experiments were performed to investigate the dynamic reversible network behaviour of the UV-cured samples. The tests were conducted using a Physica MCR 501 rheometer (Anton Paar, Graz, Austria) with sample dimensions of approximately 0.5 mm in thickness and 1 mm in diameter.

Each sample was preloaded with a normal force of 10 N and maintained at the test temperature for 15 minutes to ensure thermal equilibration. Subsequently, a constant strain of 3% was applied, and the stress response was recorded over time to evaluate the relaxation behaviour.

Experiments were conducted at various isothermal conditions to characterise the temperature dependence of the relaxation process.

The time-dependent relaxation modulus, G(t), was normalised by its initial value, G_0. The characteristic relaxation time (τ), a key parameter for covalent adaptable networks, was defined as the time required for the normalised relaxation modulus to reach 1/e of its original value, following an exponential decay behaviour described by the equation:

$$G(t) = G_{t0}\, e^{(-\frac{t}{\tau})}$$

This method allows quantification of the stress relaxation rate, which reflects the dynamic covalent bond exchange reactions responsible for the vitrimeric behaviour of the network.

3. Results and discussion

In this work, we investigated the use of epoxidised castor oil (ECO) as a biobased polymeric matrix for the development of UV-cured vitrimeric thermosets with electrically conductive properties. The chemical structure of ECO, shown in Figure 12, is characterised by long and flexible triglyceride chains that contain epoxy, ester, and hydroxyl functional groups. The epoxy groups can undergo cationic UV-curing via ring-opening polymerisation, resulting in the formation of a crosslinked thermoset network. After curing, the ester and hydroxyl groups become part of the network structure and can participate in transesterification reactions in the presence of a suitable catalyst. This enables the formation of a covalent adaptable network (CAN), which allows for thermally activated bond exchange and network rearrangement, thereby imparting reprocessing properties to the material.

Once the dynamic polymer matrix was produced and characterised for the pristine formulation, multi-walled carbon nanotubes (MWCNTs) were dispersed in the photocurable formulations at two concentrations (0.1 and 0.5 phr) to introduce electrical conductivity into the crosslinked materials. The incorporation of MWCNTs aims to create a composite material capable of combining vitrimeric behaviour with conductive functionality, potentially expanding the range of applications of these bio-based thermosets.

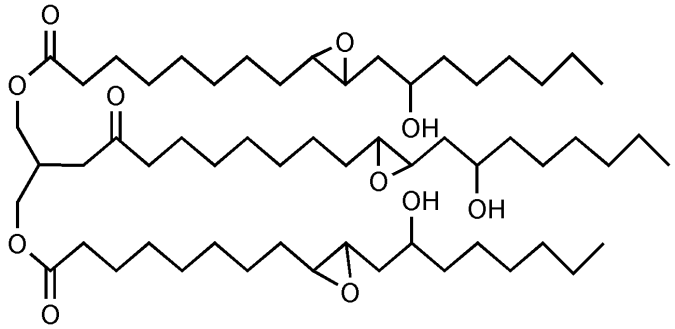

Figure 12. Chemical structure of epoxidised castor oil (ECO).

3.1. Photocuring process

The UV-curing process of the epoxy bio-based formulations was deeply investigated through two complementary analytical techniques: transmission FTIR and photo-DSC. Initially, the influence of the photo-initiator content on the curing behaviour of the pristine epoxidised castor oil (ECO) formulation was evaluated. A typical transmission-FTIR is reported in Figure 13a and 13b, where the epoxy peak

decrease around 775 cm^{-1} upon irradiation is evident, while the relative epoxy peak conversions are shown in Figure 13c. Formulations containing 1 and 2 phr of photo-initiator showed comparable performance, reaching an epoxy peak conversion of 98% after 60 seconds of irradiation. In contrast, the formulation with 4 phr of photo-initiator exhibited a lower final conversion, not exceeding 80%. This behaviour was attributed to an inner filter effect due to the excessive photoacid concentration, which increases the number of reactive points within the resin, leading to a faster gel point onset and, consequently, to a lower final conversion.

These findings were confirmed by photo-DSC analysis, shown in Figure 13d and Table 1. The exothermic peak associated with the photocuring reaction was significantly lower for the formulation containing 4 phr of photo-initiator, while the sample with 2 phr showed a more intense exothermic response, indicating higher conversion of epoxide groups. Based on these results, 2 phr was selected as the optimal concentration of photo-initiator for the resin formulation.

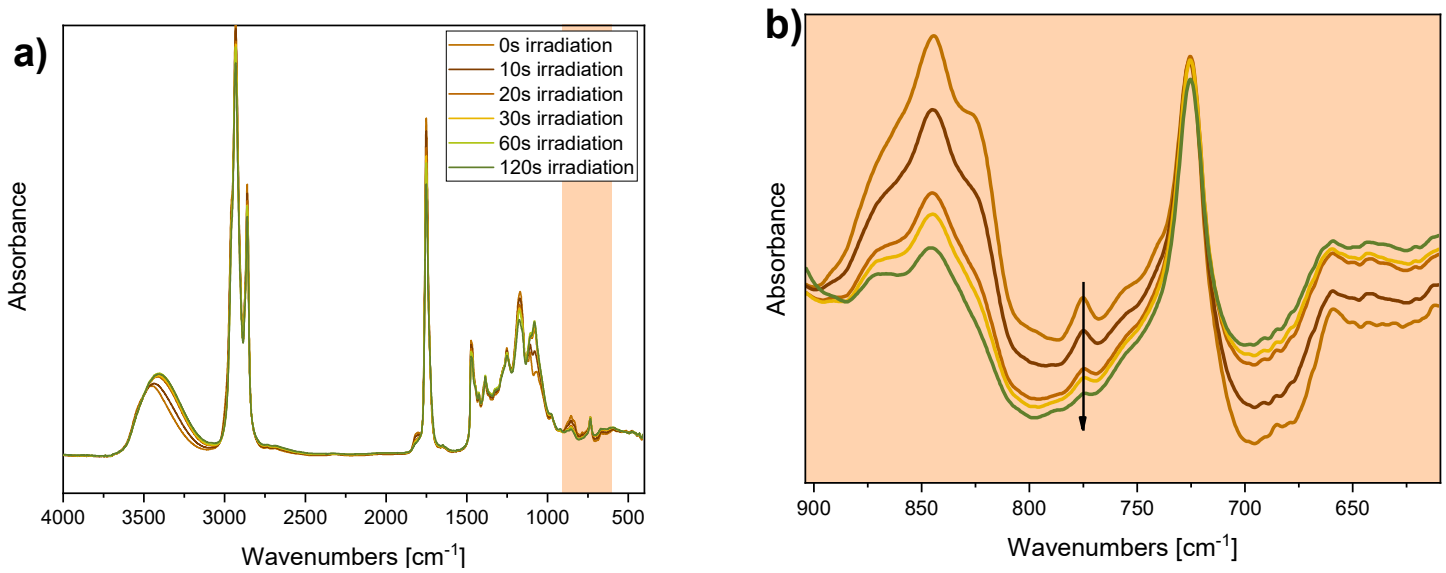

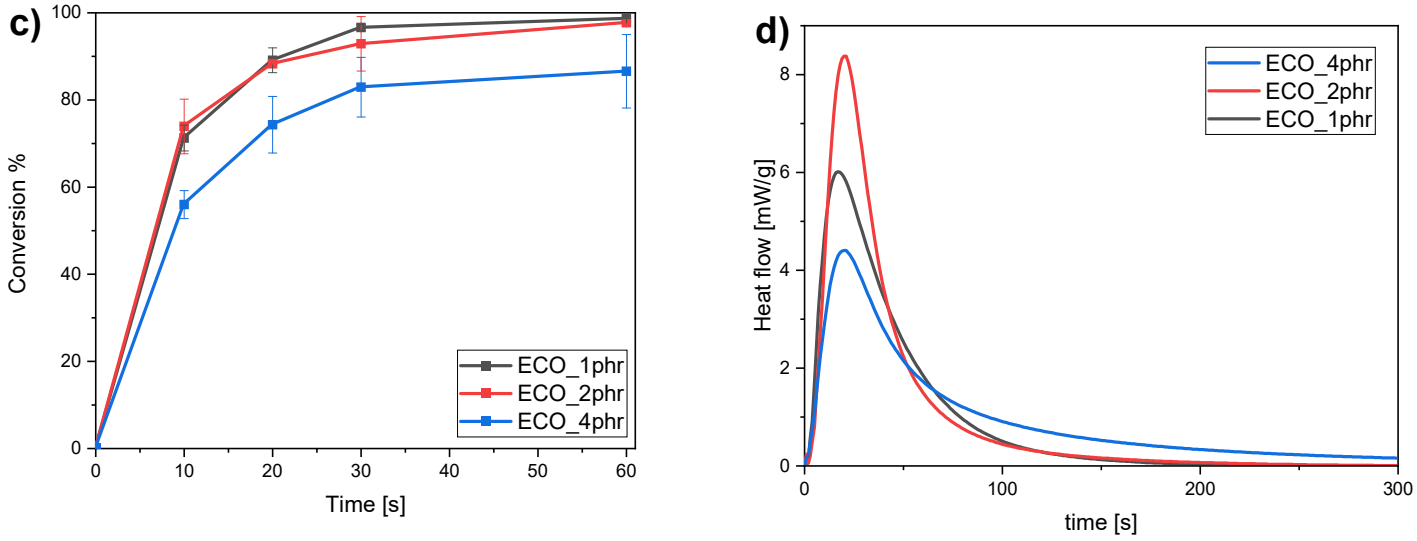

Figure 13. Photocuring process monitored by transmission-FTIR and photo-DSC. a) Representative FTIR spectra over irradiation time. b) Magnification of the epoxy region of the spectra. c) Corresponding epoxy peak conversion (%) as a function of irradiation time. d) Heat released during the photocrosslinking reaction, measured by photo-DSC.

Once the optimal curing conditions were established for the ECO matrix, the influence of carbon nanotubes (CNTs) was studied, with CNTs content ranging from 0.1 to 0.5 phr. The photocrosslinking behaviour was monitored as well as by transmission-FTIR (Figure 14a), following the decrease of the epoxy signal at 775 cm^{-1} over irradiation time. The addition of CNTs resulted in a gradual decrease in both the rate of polymerisation and the final epoxy conversion. While the formulation with 0.1 phr CNTs showed a similar conversion to the pristine resin, the one with 0.5 phr achieved only ~88% conversion. This reduction is attributed to UV absorption by the CNTs, which act as competitive absorbers due to their broadband UV absorbance related to the plasmon resonance of π-electrons.

These results were confirmed by photo-DSC analysis. As shown in Figure 14b and relative Table 1, a consistent decrease in the exothermic enthalpy was observed with increasing CNT content. The exothermic peak area dropped from 296 J/g (pristine ECO) to 199 J/g (0.5 phr CNTs), indicating reduced conversion. Moreover, a slight delay in the exothermic peak (t_peak) was also detected, further confirming the light-screening effect of CNTs and the subsequent deceleration in polymerisation kinetics. Nonetheless, even the most filled formulation achieved satisfactory curing, maintaining a conversion above 80%.

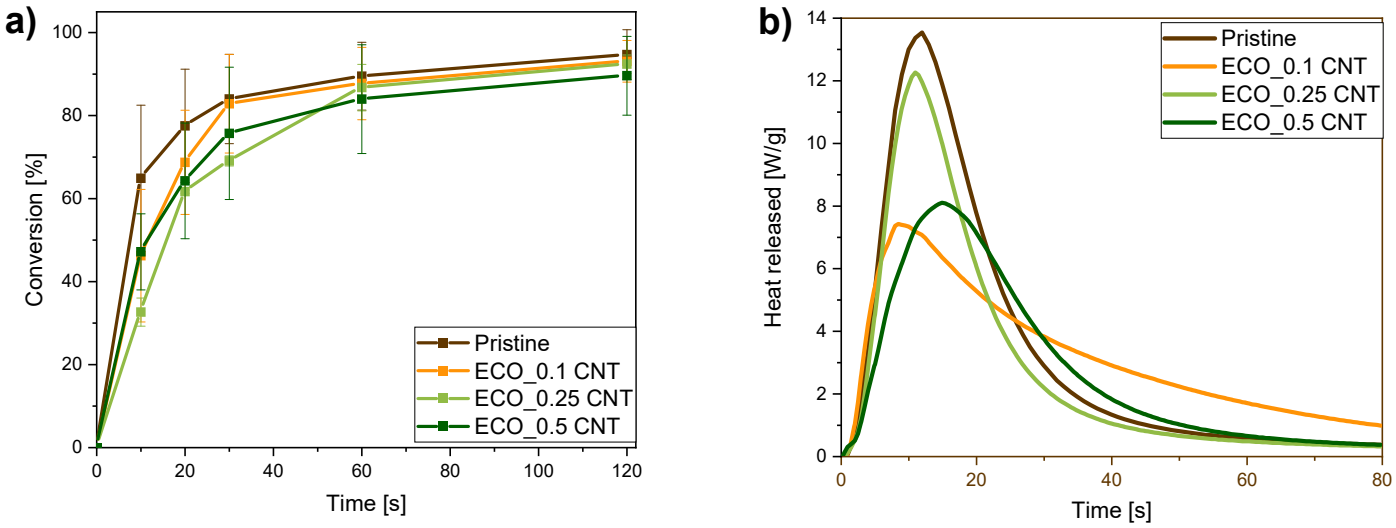

Figure 14. Photocuring process monitored by transmission-FTIR and photo-DSC for the MWCNTs. a) Is the epoxy peak conversion (%) as a function of irradiation time. b) Is the heat released during the photocrosslinking reaction measured by photo-DSC.

Table 1. PhotoDSC values obtained for both the pristine ECO formulations and the formulations containing MWCNT (The filled formulations contain 2 phr of photoinitiator).

Sample	Integral (J/g)
ECO_1phr	256.3±15.0
ECO_2phr	296.4±16.7
ECO_4phr	227.1±28.2
ECO_0.1CNT	228.4 ± 4.7
ECO_0.25CNT	226.5 ± 18.9
ECO_0.5CNT	199.9 ± 17.2

Subsequently, the effect of the transesterification catalyst, dibutyl phosphate (DP), was investigated at two concentrations (10 and 15 phr). Both FTIR and photo-DSC analyses demonstrated a negligible influence of DP on the photocuring process. The epoxy conversion and exothermic enthalpy were very similar among the tested formulations, suggesting that the addition of the catalyst does not interfere with the initial crosslinking reaction but is expected to activate the exchange reactions at elevated temperatures post-curing.

3.2. Viscoelastic, mechanical and thermal properties of cured ECO-materials

Dynamic mechanical thermal analysis (DMTA)

The viscoelastic properties of the UV-cured samples were initially investigated by DMTA analysis. In Figure 15, the tan δ and storage modulus (E') curves are reported for the pristine ECO formulation and for the formulations containing the transesterification catalyst dibutyl phosphate (DP) at 10 and 15 phr. The corresponding glass transition temperatures (T_g), recorded as the maximum of the tan δ peak, as well as the elastic modulus and the number of crosslinks per volume, are collected in Table 2. The UV-cured sample containing 10 phr DP showed a slight enhancement of thermo-mechanical performance compared to both the pristine matrix and the sample containing 15 phr DP. This suggests that an excess of transesterification catalyst may slightly reduce the crosslinking density, possibly due to premature activation of transesterification reactions during photocuring, resulting in a lower T_g.

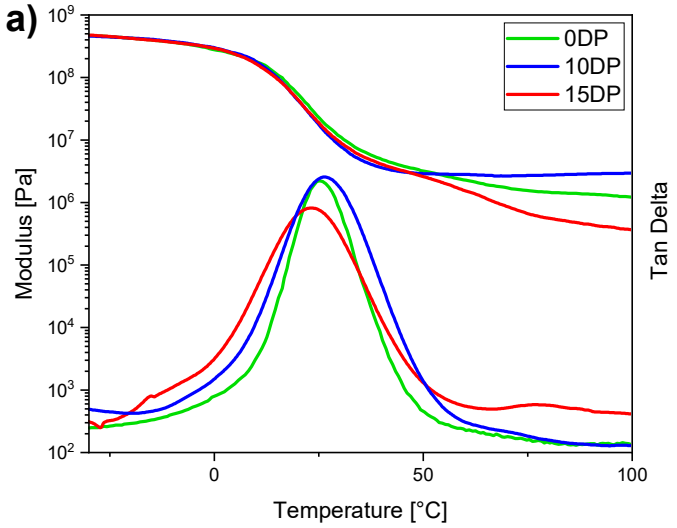

Sample	T_g [°C][1]	Modulus [MPa][2] measured at T_g+50°C
0DP	21±4	0.7 ±0.5
10DP	26±4	2.7±4.1
15DP	23±5	0.5±0.1

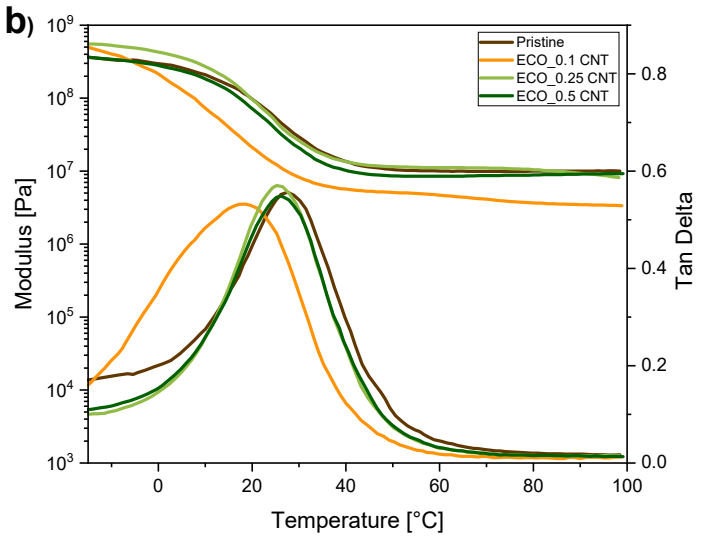

Sample	T_g [°C][1]	Modulus [MPa][2] measured at T_g+50°C
Pristine	29 ± 1	7.8 ± 2.3
ECO_0.1CNT	18 ± 2	3.0 ± 1.7
ECO_0.25CNT	24 ± 1	8.4 ± 2.1
ECO_0.5CNT	26 ± 1	8.4 ± 0.3

Figure 15 and relative Table 2. (a) DMTA data for the pristine formulation obtained with different amounts of transesterification catalyst and relative values; (b) DMTA data for the composite formulations containing increasing CNT content and relative values.

Subsequently, the effect of carbon nanotubes (CNTs) on the thermo-mechanical behaviour of the ECO matrix was investigated. Figure 15b reports the tan δ and E' curves for all the CNT-containing formulations, while the corresponding T_g values are summarised in Table 2. A slight reduction in T_g was observed for the composite with 0.1 phr CNTs (18 °C) compared to the pristine formulation (29 °C), likely due to a lower epoxy conversion in the presence of CNTs, as previously discussed. However, by increasing the CNT content to 0.25 and 0.5 phr, the T_g values increased to 24 °C and 26 °C, respectively. This trend indicates a dual effect: while low CNT content may reduce crosslinking density and lead to flexibilization, higher CNT loadings impart a reinforcing effect that counteracts this phenomenon. Indeed, CNTs can hinder polymer chain mobility, thereby enhancing thermo-mechanical properties, as confirmed by the increase in both T_g and storage modulus in the rubbery region with increasing CNT content.

Thermogravimetric analysis (TGA)

The thermal stability of UV-cured ECO formulations was evaluated by thermogravimetric analysis (TGA), with representative degradation curves reported in Figure 16. All samples exhibited good thermal resistance, with the 5% weight loss temperature ($T_{5\%}$) and the onset of degradation around 200 °C. The onset of degradation corresponds to an important threshold, as it defines the maximum

temperature applicable during reprocessing and activation of bond exchange reactions.

The pristine ECO sample (without catalyst) showed two main degradation steps. In contrast, samples containing the transesterification catalyst (DP) exhibited three distinct degradation steps, suggesting a more complex degradation mechanism possibly influenced by the catalyst.

To assess the effect of MWCNT addition, TGA was also performed on the composite samples. As an example, the curve of the UV-cured film with 0.1 phr MWCNTs is shown in Figure 16. Two main degradation steps were observed: the first, at lower temperatures, is attributed to the degradation of residual photoinitiator and unreacted monomers; the second, occurring around 400 °C, corresponds to the decomposition of the crosslinked ECO network, as expected by observing the other trials. Carbon nanotubes remained thermally stable throughout the analysis, consistent with their well-known resistance to high temperatures [109,110].

Similar thermal behaviour was observed across all tested MWCNT-containing formulations, confirming that both catalyst and CNT incorporation do not compromise the thermal resistance of the cured network.

Thermogravimetric analysis is crucial for determining the safe operational window of the materials and supporting subsequent investigations into the activation of covalent bond exchange reactions.

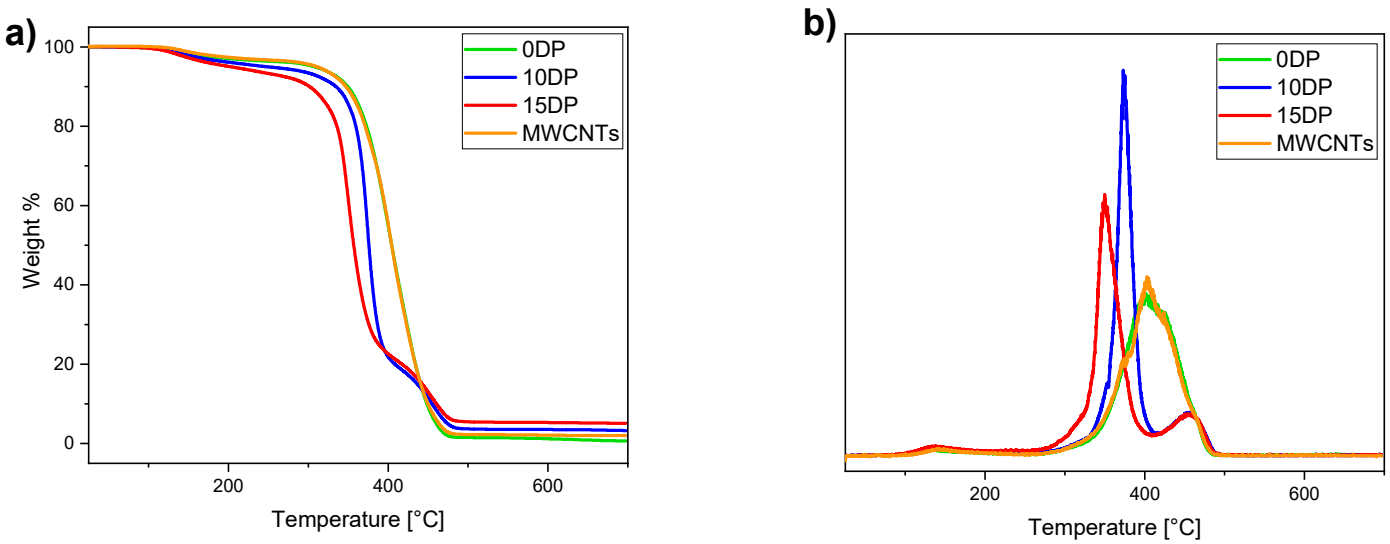

Figure 16. a) TGA curves of the UV-cured ECO formulations containing different amounts of transesterification catalyst (DP) and 0.1 phr of MWCNTs. b) First derivative of the corresponding TGA curves that highlight the main degradation steps.

Electrical conductivity

The electrical conductivity of the MWCNT-containing cured films was measured by broadband dielectric spectroscopy to determine the percolation threshold. Figure 17 shows the conductivity as a function of filler loading. All composite samples exhibited higher conductivity than the pristine ECO film, but a pronounced jump of approximately seven orders of magnitude occurred at 0.5 phr CNT. While the pristine UV-cured ECO displayed a conductivity of $\sim 1 \times 10^{-13}$ S/cm, the formulation with 0.5 phr CNT reached $\sim 1 \times 10^{-6}$ S/cm, indicating the formation of a continuous conductive network. From these results, the percolation threshold lies between 0.25 and 0.5 phr of CNT, which is consistent with literature reports of biobased epoxy–CNT composites where percolation is achieved at around 0.4 phr [111].

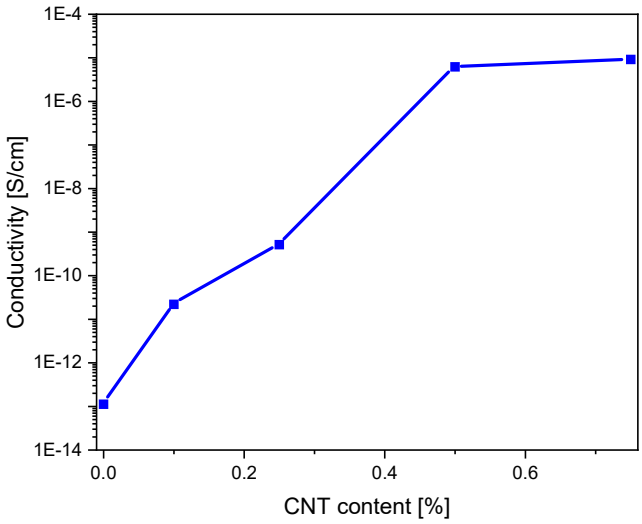

Figure 17. Conductivity of UV-cured ECO films containing various CNT concentrations, as determined by dielectric spectroscopy.

Stress relaxation experiments

The dynamic nature of covalent adaptable networks is enabled by thermally activated covalent bond exchange reactions, which facilitate stress relaxation and network rearrangement at elevated temperatures. In our system, epoxidised castor oil (ECO) provides a polymer backbone that consists of both ester and hydroxyl functionalities. During UV-curing, the epoxy groups form a crosslinked thermoset, while the remaining esters and hydroxyls remain available as sites for transesterification reactions when, at high temperature, they are catalysed by dibutyl phosphate (DP).

Before evaluating vitrimeric behaviour, amplitude-sweep tests were performed at 170 °C and 200 °C to determine the linear viscoelastic region (LVR) of the polymeric matrix. Both the pristine ECO (no catalyst) and the formulation with 15 phr DP maintained linearity up to 3 % strain (Figure 18); for this reason, a 3 % constant strain was chosen for all subsequent stress-relaxation experiments.

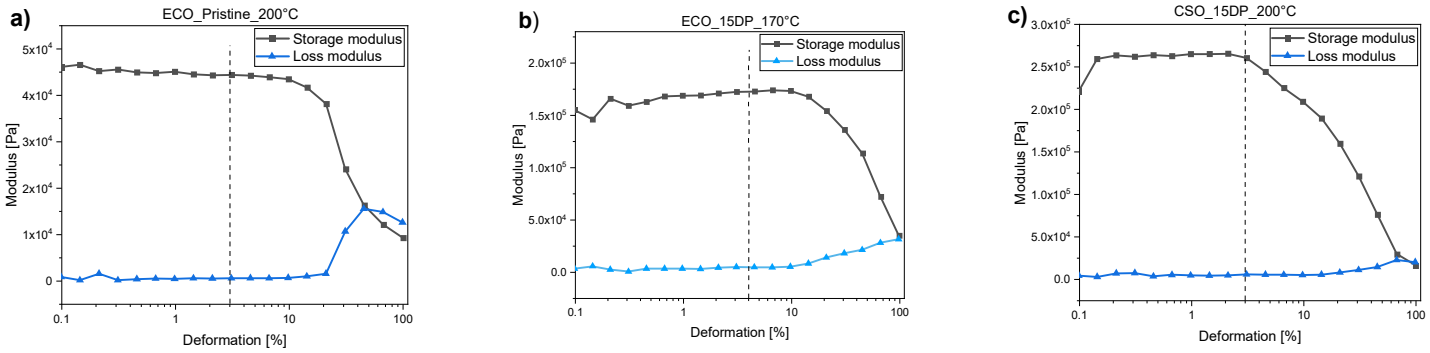

Figure 18. Amplitude sweep tests of pristine ECO UV-cured samples with no catalyst at 200 °C (a), ECO UV-cured samples containing 15 phr DP at 170 °C (b), and at 200 °C (c).

Stress-relaxation tests were performed using samples 0.5 mm thick, having 1 mm diameter, that were first preloaded with 10 N for 15 min at the test temperature, then held at 3 % strain while the decay of the relaxation modulus G(t) was recorded over time. The characteristic relaxation time τ was measured as the time at which G(t) falls to 1/e of its initial value G_0.

In Figure 19, relaxation at the constant temperature of 200 °C for ECO with no catalyst, 10 phr DP and 15 phr DP is reported. The pristine sample shows only modest stress decrease, reflecting its purely viscoelastic response and the high flexibility (low T_g), while both DP-containing samples relax much more rapidly. We can then state that higher DP loading reduces τ, indicating faster transesterification reaction and network rearrangement.

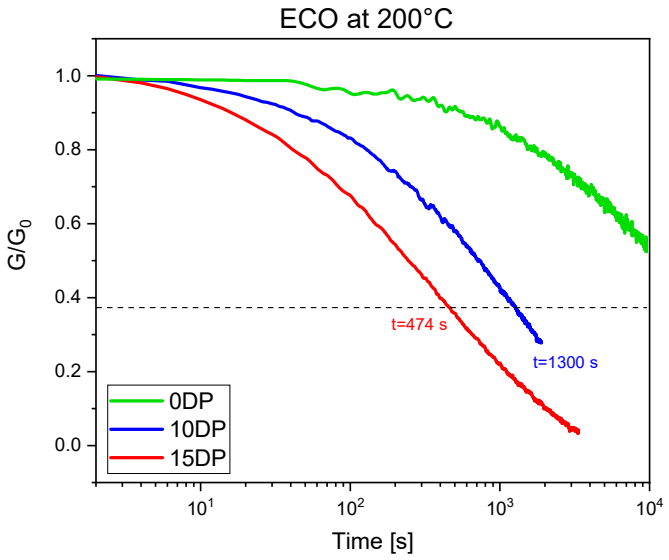

Figure 19. Stress relaxation measurement performed for ECO with no catalyst (DP) and with 10 and 15 phr of DP at a constant temperature of 200°C.

In Figure 20, stress-relaxation curves at 170, 180, 190 and 200 °C for the 10 phr and 15 phr DP samples, respectively, are plotted alongside their Arrhenius plots. The 15 phr sample follows a single linear Arrhenius regime, while the 10 phr sample shows two distinct slopes, reflecting, as Hubbard et al. first described, a low-temperature regime controlled by chain relaxation and a higher-temperature regime dominated by bond exchange kinetics. The fitting in the Arrhenius plots can demonstrate that the ECO material, in the presence of the transesterification catalyst, can activate the dynamic covalent network, thereby exhibiting reprocessability properties.

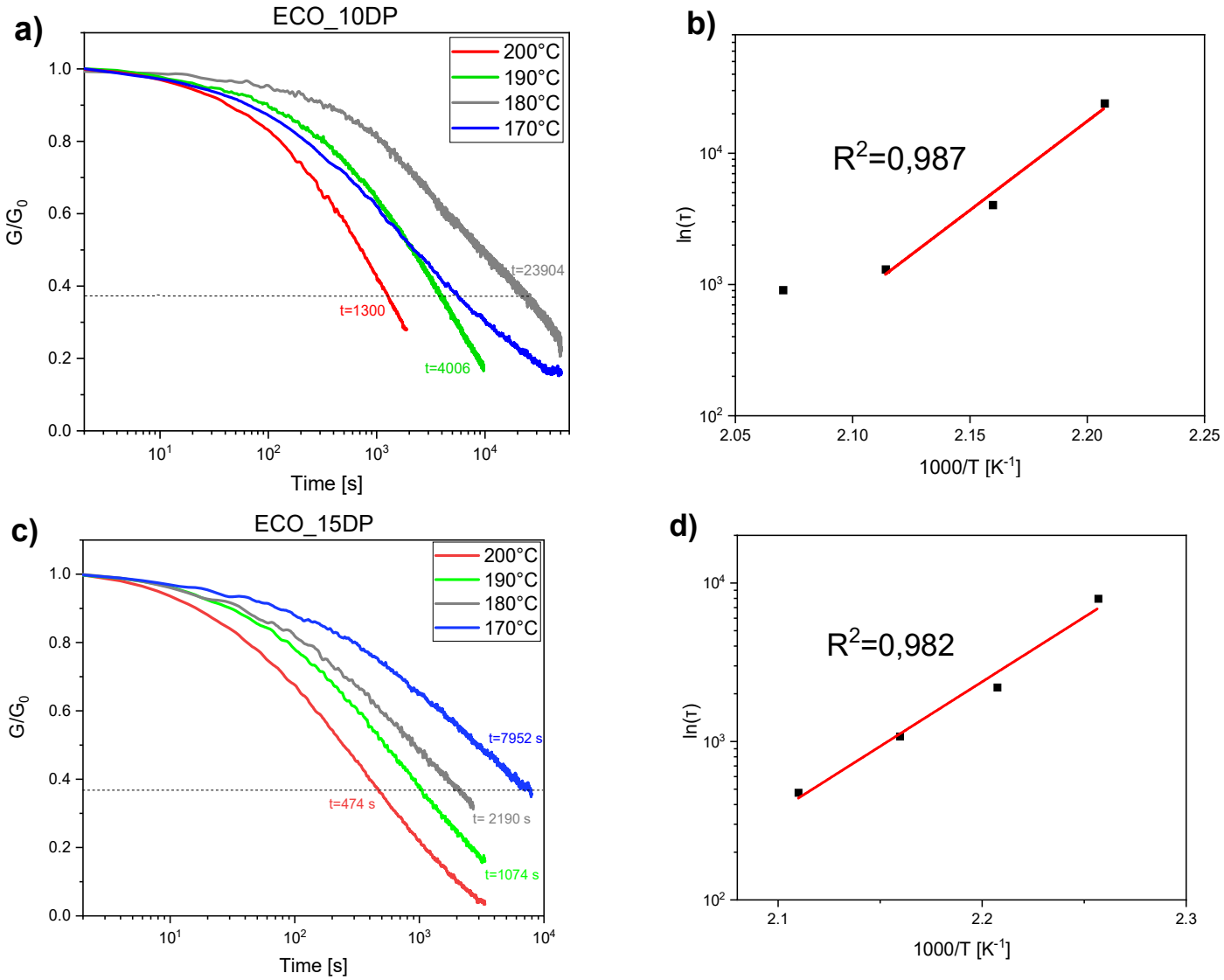

Figure 20. Stress relaxation measurement performed at different temperatures, and their relative Arrhenius plots. a) Relaxation measurement of the ECO sample with 10 DP. b) Arrhenius plot of ECO with 10 phr DP. c) Relaxation measurement of ECO sample with 15 phr DP. d) Arrhenius plot of ECO with 15 phr DP.

To assess the effect of conductive fillers on vitrimeric behaviour, we performed stress-relaxation tests on UV-cured ECO composites containing 0.5 phr multi-walled carbon nanotubes (CNTs), both with and without 10 phr DP. Figure 21a shows stress relaxation at 70 °C: the CNT-only sample displays slow viscoelastic decay (similar to the pristine matrix), while the CNT+DP sample relaxes much more quickly. Figure 21b extends these measurements up to 100 °C, confirming that τ decreases with increasing temperature. Finally, Figure 21c presents the Arrhenius plot for the CNT+DP composite, which exhibits a linear relationship between ln τ

and 1000/T. From the slope, we obtain an activation energy of 49.9 kJ/mol, consistent with typical values reported for vitrimeric transesterification. The activation energy was obtained with the formula:

$$\ln(\tau) = \ln(\tau_0) + E_a \frac{1}{RT}$$

Where E_a correspond to the activation energy, R is the universal gas constant, T is the temperature in °K, τ is the time needed to the formulation to reach 1/e, also called relaxation time, of its initial G(t) modulus, and τ_0 represents the hypothetical relaxation time the network would exhibit if the activation barrier were zero (i.e., at infinitely high temperature).

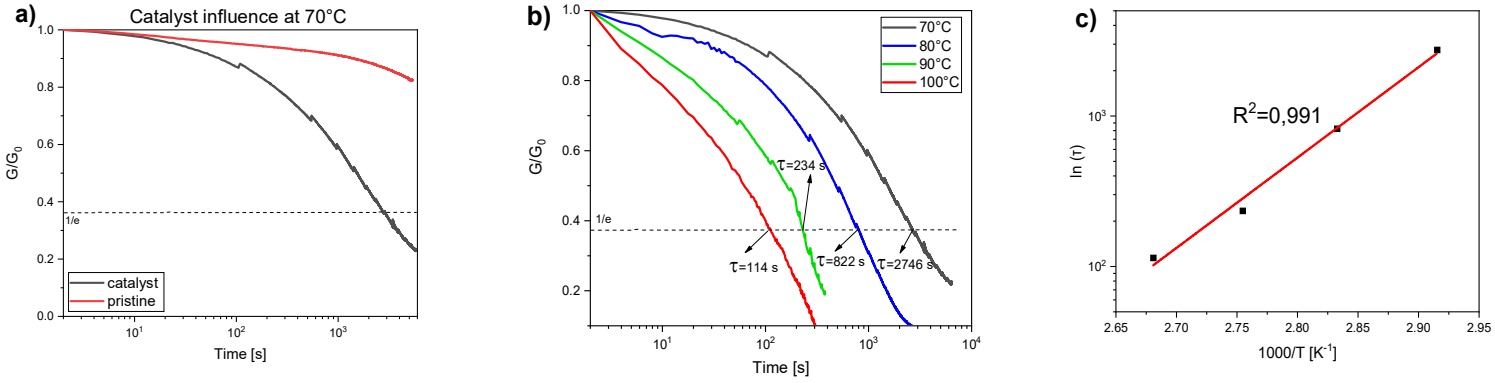

Figure 21. a) Represent the stress relaxation at a constant temperature of ECO reinforced with 0.5 phr MWCNTs with and without the catalyst. b) represents the stress relaxation at different temperatures of the ECO filled with different amounts of MWCNTs, and c) is the Arrhenius plot derived from the stress relaxation experiments.

These results demonstrate that DP catalyses rapid stress relaxation via transesterification, the kinetic regime can shift depending on catalyst concentration, and the addition of MWCNTs does not prevent the activation of the bond exchange but may slightly modify relaxation kinetics by decreasing its activation temperature, since there is a lower crosslinked structure derived by the interconnecting inert points due to the reinforcement.

3.3. Comparison with biobased reprocessable CANs and commercial thermosets

The ECO-based covalent adaptable networks developed in this work display a combination of glass transition temperature, stiffness and relaxation behaviour that places them within the performance window of recently reported bio-based vitrimer systems. Bio-derived epoxidised vegetable oils typically yield vitrimers with T_g values between 30 and 80 °C and rubbery moduli of a few MPa, depending on crosslink density and catalyst content. In our research, the ECO–DP networks

match the lower-intermediate glass transition temperature range reported for epoxidised soybean oil and castor oil vitrimers, while preserving a fully bio-based nature and using a simple transesterification chemistry for network rearrangement. In fact, biobased imine and transesterification-based vitrimers often rely on multi-step syntheses or partially fossil-derived monomers, while the present system instead exploits a single monomer (ECO) and a small-molecule catalyst to introduce dynamic character, which is advantageous from both a synthetic and life-cycle perspective [112–114].

When compared with fossil-based commercial thermosetting epoxies used in coatings and structural applications, ECO–DP networks exhibit lower T_g and modulus, but compensate with reprocessability, repairability, and a high renewable content. Conventional UV-curable epoxy networks typically reach T_g values in the 60–120 °C range and storage moduli between 5 and 20 GPa in the glassy state; however, they are intrinsically non-reprocessable and fully derived from fossil sources. In contrast, ECO–DP vitrimers offer sufficient stiffness for flexible coatings, sealants and low load-bearing structural parts, while enabling reshaping and welding under transesterification conditions, thus directly supporting circular economy applications. The incorporation of MWCNTs further narrows the mechanical gap with commercial epoxy formulations by increasing modulus and imparting electrical conductivity. [115–117]

The activation temperature for transesterification observed in this work (~170 °C) lies within the processing window identified in previous vitrimeric epoxy literature, and the thermal stability onset ($T_{5\%}$ = ~200 °C) is consistent with bio-based thermosets currently available. This alignment indicates that the ECO-DP system can be recycled through reprocessing cycles without degradation, a critical advantage for circular economy applications in coatings and adhesives. Recent literature on epoxidised vegetable oil-based vitrimers has demonstrated that these systems can achieve comparable or superior performance to conventional epoxies in specific application niches, particularly when tuned for mechanical and thermal balance by varying stoichiometric ratios and catalyst loading. [118,119]

4. Conclusion

In these studies, we demonstrated that unmodified, biobased epoxidised castor oil (ECO) can be rapidly and completely cured under UV irradiation, even when reinforced with multi-walled carbon nanotubes (MWCNTs) to enhance the material functionality. Upon heating, the cured networks exhibit transesterification driven

bond exchange, enabling reprocessing despite their thermoset nature. Incorporating MWCNTs not only imparts electrical conductivity but also appears to lower the activation temperature for dynamic covalent exchange, likely due to increased chain mobility deriving from a modest reduction in crosslink density. By varying catalyst concentration, crosslink density, and filler loading, we have analysed the structure-property relationships that govern relaxation kinetics and performance. These findings provide a solid foundation for the design of sustainable, reprocessable, and functional thermoset coatings.

The work described in this chapter has been published and is available at the following references:

[120] Sangermano M.; Bergoglio M.; Schögl S.; Biobased Vitrimeric Epoxy Networks. *Macromolecular Materials and Engineering,* **2024**, 9, 309, DOI: https://doi.org/10.1002/mame.202300371

[63] Bergoglio M.; Reisinger D.; Schögl S.; Griesser T.; Sangermano M.; Sustainable Bio-Based UV-Cured Epoxy Vitrimer from Castor Oil. *Polymers* 2023, 15(4), 1024; DOI: https://doi.org/10.3390/polym15041024

[121] Bergoglio M.; Palazzo G.; Reisinger D.; Porcarello M.; Kortaberria G.; Schögl S.; Sangermano M.; Cationic UV-curing of bio-based epoxidised castor oil vitrimers with electrically conductive properties. *Reactive and Functional Polymers* **2024** 200 105936, DOI: https://doi.org/10.1016/j.reactfunctpolym.2024.105936

Chapter 3: Biobased scaffolds for tissue engineering

Bone injuries and disease-related defects represent a rising challenge to global health, also due to the incidence of non-healing fractures, which rises sharply with age [122]. Although natural bone possesses an intrinsic capacity for self-repair, critical defects often require surgical intervention. Conventional approaches, such as autografts, allografts, and metal implants, can alleviate these defects but bring complications ranging from donor-site morbidity to long-term foreign-body reactions [123]. Tissue engineering aims to address these limitations by providing synthetic or semi-synthetic scaffolds that not only replace lost tissue volume but also actively guide new bone formation through controlled delivery of biochemical cues and tailored mechanical support.

An ideal scaffold for bone regeneration must simultaneously satisfy multiple requirements. It must be mechanically robust enough to withstand physiological loads, particularly in weight-bearing sites, but also porous and interconnected to permit cell infiltration, nutrient transport, and vascular ingrowth [124,125]. The chemistry of the scaffold should promote cell attachment, proliferation, and osteogenic differentiation.

In the case of bone tissue replacement, the material should also release bioactive ions that trigger the processes leading to the formation of hydroxyapatite, thereby mimicking the native mineral phase. This can be accomplished with the aim of bioactive glasses. First introduced by Larry Hench, bioactive glasses (BGs) constitute a class of ceramic biomaterials that offer osteoconductive, osteoinductive, and therapeutic properties (e.g., angiogenic and antibacterial properties) by releasing ions typical of the glass network. For this reason, they are crucial for bone repair [126,127]. Moreover, as mentioned, besides promoting bone regrowth, BGs can also exhibit antibacterial properties, which are attributed to a local increase of pH in the body fluids. The antibacterial effect can also be increased by the incorporation of various metal ions [128–130]. Among them, Ag and Cu have been extensively studied for biomedical applications since they offer a dual role in promoting antimicrobial activity and facilitating tissue repair by giving anti-inflammatory effects, while Te is emerging as a promising ion thanks to its beneficial properties, but it has not been extensively studied [126,131–138].

Although BGs have multiple benefits, pure BG scaffolds generally fall short in mechanical strength, precluding their use in load-bearing applications [139]. Embedding BG particles within polymer matrices has emerged as an optimal strategy to address this issue, yielding composites that combine improved toughness and elasticity with the bioactivity of the glass [140]. A variety of fabrication techniques, ranging from traditional moulding and solvent-casting to electrospinning and modern additive manufacturing (AM), have been employed to produce these polymer–ceramic hybrids [141–144]. Moreover, the choice of polymeric matrix permits tuning of the scaffold stiffness, toughness, and degradation rate, enabling the design of products tailored to the mechanical and biological demands of different tissue-engineering [145].

At the same time, scaffolds should degrade in synchrony with tissue formation, thereby avoiding chronic inflammation caused by accumulating degradation products. Finally, the sustainability of the product is fundamental, since the research has shifted towards biobased products to replace petroleum-derived polymers with renewable, biodegradable alternatives.

This chapter explores three complementary scaffold platforms, hydrogels, polyHIPE foams, and 3D-printed bulk scaffold obtained by means of mSLA 3D printing, each built upon bio-based monomers and similar BGs fillers. The chapter begins with "soft," highly hydrated methacrylated chitosan hydrogels reinforced with tellurium-doped bioactive glasses, demonstrating dual antimicrobial and osteoinductive functions in a compliant matrix. Next, it moves to the hard tissue engineering scaffolds. First, the chemistry is shifted into porous polyHIPE foams via thiol–ene photopolymerization of acrylated-soybean oil (AESO) and a multifunctional thiol, showing how high internal phase emulsions yield mechanically tunable, interconnected pores that support osteoblast-like cell growth and mineral deposition. Finally, it defines the design of rigid, patient-specific scaffolds manufactured by layer-by-layer vat photopolymerization of AESO-based resins loaded with silanised or ion-doped bioactive glasses. In this last platform, we also introduced dynamic covalent (vitrimeric) networks, activated by transesterification catalysts, to give the photocured materials reprocessability, bridging the gap between conventional disposable implants and sustainable, repairable biomaterials.

By monitoring this progression, from soft gels that mimic the extracellular matrix to load-bearing, reprocessable implants, this chapter illustrates how, starting from bio-based monomers and adding inorganic fillers, the demands for multi-properties and bioderived materials for bone tissue engineering can be met.

Paper I *Tellurium-Doped Silanised Bioactive Glass–Chitosan Hydrogels: A Dual Action for Antimicrobial and Osteoconductive Platforms*

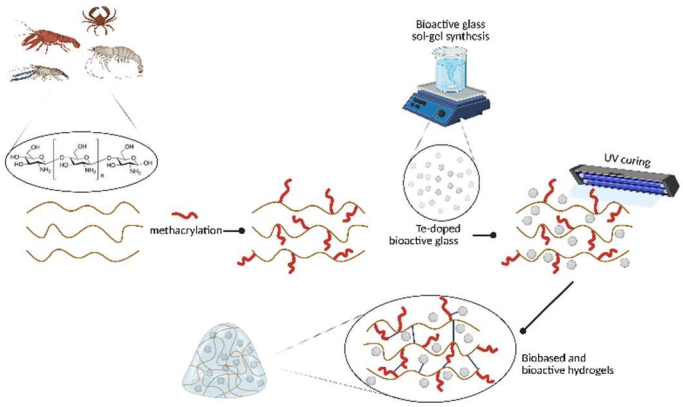

Paper II
3D-Printed Biobased Thiol-Ene Photocurable Scaffolds Reinforced With Bioactive Glasses Achieved By High Internal Phase Emulsion Polymerisation

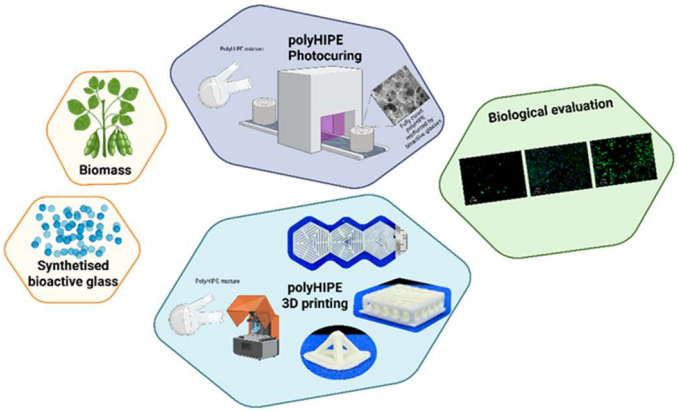

Paper III U*V-Cured Bio-Based Acrylated Soybean Oil Scaffold Reinforced with Bioactive Glasses*

Paper IV *Silanised and Cu-doped bioactive glass as filler for biobased photocurable 3D printed scaffolds*

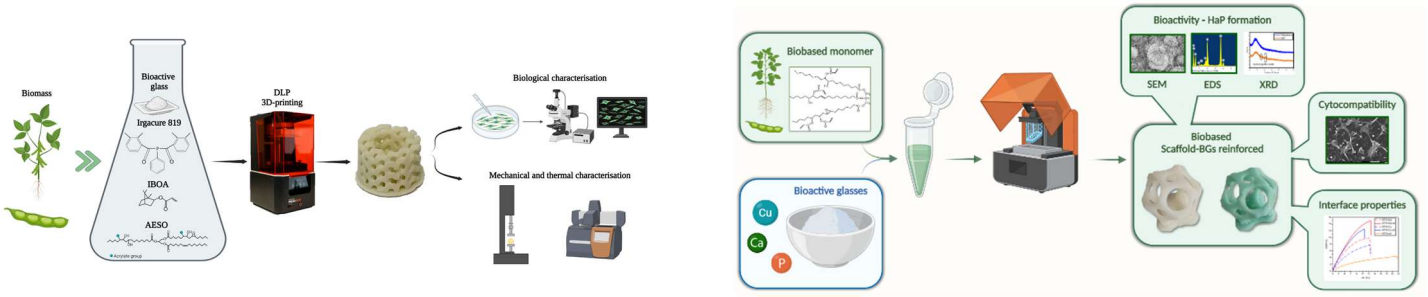

Paper V *3D-Printed Acrylated Soybean Oil Scaffolds with Vitrimeric Properties Reinforced by Tellurium-Doped Bioactive Glass*

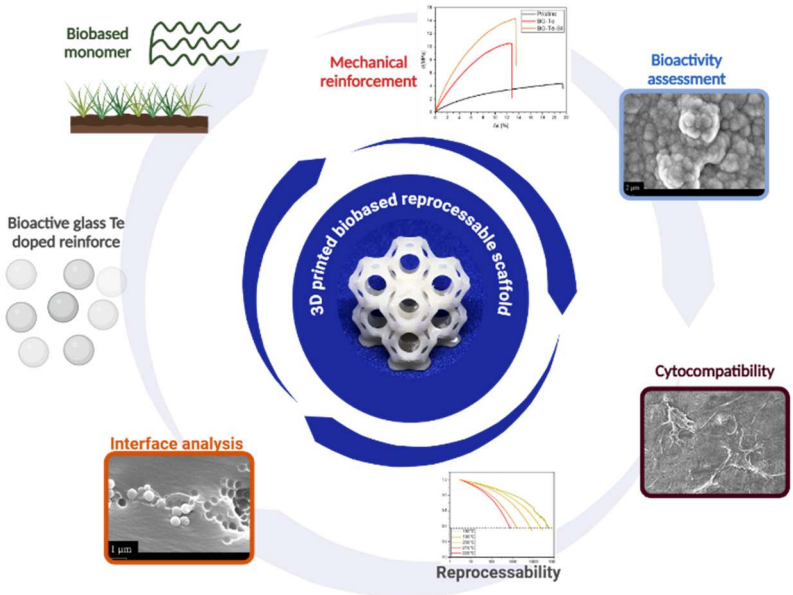

3.1 Introduction

Bone defects arising from trauma, disease, or congenital malformations present a critical clinical challenge: while small defects in healthy bone exhibit an intrinsic capacity for repair, defects exceeding a critical size and in elderly patients, often >2.5 cm, cannot regenerate without intervention, leading to delayed union or non-union [146,147]. This can result, for instance, in 13% of tibial fractures, which therefore necessitate surgical grafting or implant procedures [148]. Tissue engineering scaffolds aim to restore the structural and biological structure of native bone by providing a three-dimensional (3D) framework that supports cell adhesion, proliferation, and differentiation, while simultaneously providing vascular ingrowth and nutrient transport [124,146,149–154]. An ideal scaffold must replicate the extracellular matrix (ECM) at multiple length scales, possess mechanical properties suitable for the target site (from soft, gel-like properties to load-bearing rigidity), actively guide osteogenesis through biochemical signals starting from the support in HAp growth, and be easily manufactured to meet the demands of patient-specific geometries.

To address these complex requirements, this chapter explores a broad range of biobased scaffolds, ranging from soft hydrogels to high-porosity foams (polyHIPEs) to rigid, 3D-printed acrylated-soybean-oil (AESO) composites, each synthesized via rapid, energy-efficient photopolymerization and reinforced with bioactive glasses (BGs) used for osteoinduction and doped with different ions to impart additional properties to the final material.

3.1.1 Hydrogels for soft tissue: Methacrylated Chitosan and Te-Doped Bioactive Glass

Hydrogels are hydrated, crosslinked polymer networks capable of retaining >90% water in weight while maintaining their shape under mechanical load. Their soft tissue-like mechanics and high-water content create an ECM-analogous microenvironment ideal for cell culture, drug delivery, and wound dressings [148,155–161]. Among natural polymers, chitosan, derived from alkaline deacetylation of chitin sourced from shellfish or fungi, offers abundant availability, biodegradability, and facile chemical reactivity [162–164]. By grafting methacrylate groups onto its chemical structure, chitosan becomes suitable for UV-induced radical crosslinking, enabling rapid formation of stable hydrogels under mild, aqueous conditions [165–167]

To impart osteoconductivity and antimicrobial activity to hydrogels, sol–gel-synthesized bioactive glasses doped with tellurium (BG-Te) and further functionalized via silanization (BG-Te-Sil) were incorporated at 30 and 50 phr. BG-Te releases Si, Ca, and PO_4 ions that induce the precipitation of hydroxyapatite under physiological conditions, while Te doping confers antibacterial and anti-inflammatory effects [131–135].

3.1.2 Highly Porous PolyHIPEs: Thiol–Ene AESO Foams Reinforced with BG

Translating hydrogel chemistry to a solid foam architecture, high internal phase emulsions (HIPEs) of acrylated-epoxidized soybean oil (AESO) and trimethylolpropane tris(3-mercaptopropionate) (TMPTMP) were UV-cured to yield polyHIPEs with nominal 80% porosity. In these thiol–ene networks, water droplets serve as the templating phase, and upon photopolymerization, interconnected spheroidal voids remain [168–171]. Also in this case, BG loading 15 and 30 phr was used to give osteoinductive properties to the final scaffold.

3.1.3 Hard tissue AESO Composites: Vat Photopolymerization and covalent adaptable networks

For load-bearing applications and patient-specific geometries, acrylated soybean oil (AESO) was formulated with reactive diluents (isobornyl acrylate or acrylated eugenol) into photocurable resins compatible with DLP/mSLA 3D printing at 25–100 μm resolution. Sol–gel bioactive glasses (undoped, Cu-doped, Te-doped and silanised) were dispersed at a maximum of 30 phr, with TMSPMA silanisation to enhance interfacial adhesion.

Moreover, with the aim of a transesterification catalyst, the final scaffold was proven to possess reprocessability behaviour, bridging the gap between the previous chapter where vitrimeric formulations were studied. This allows the production of a 3D printed material which can be used as a hard tissue replacement, biobased and reprocessable, meeting the growing demand of the circular economy.

3.2 Experimental section

3.2.1 Material and chemicals

Acrylated soybean oil (AESO) was supplied either from Allnex (Frankfurt, Germany) or Sigma Aldrich (Milan, Italy). Isobornyl acrylate (IBOA), tetraethyl orthosilicate (TEOS), triethyl phosphate (TEP), calcium nitrate tetrahydrate ($Ca(NO_3)_2 \cdot 4H_2O$), ammonium hydroxide (NH_4OH), 3-(trimethoxysilyl)propyl methacrylate (TMSPMA) were obtained from Sigma-Aldrich (Milan, Italy). The photoinitiator phenylbis (2,4,6-trimethylbenzoyl) phosphine oxide (old commercial name Irgacure 819) was purchased from BASF (Ludwigshafen, Germany). Acrylated eugenol (AEUG) and the eugenol-based phosphate ester transesterification catalyst (EUGP) were synthesised according to literature procedures [172–174]. Bioactive glass (BG) was prepared via a sol–gel route using tetraethyl orthosilicate (TEOS), triethyl phosphate (TEP), sodium tellurite (Na_2TeO_3), 3-(Trimethoxysilyl) propyl methacrylate (98%, TMSPMA), ethanol (EtOH, 99%), all purchased from Sigma Aldrich, as were hydrogen peroxide (H_2O_2), Tween 80, penicillin/streptomycin, hematoxylin and eosin, and all other cell-culture reagents (DMEM + glutaMAX, Gibco; Thermo Fisher). Copper-doped and tellurium-doped bioactive glass (BG-Cu and BG-Te) were synthesised using copper (II) nitrate trihydrate ($Cu(NO_3)_2 \cdot 3H_2O$) and sodium tellurite (Na_2TeO_3), purchased from Sigma Aldrich. Lauria Bertani (LB) broth and agar were supplied by Thermo Fisher Scientific (Milan, Italy). Trimethylolpropane tris(3-mercaptopropionate) (TMPTMP) and the surfactant Hypermer B246 were used as received from their respective suppliers.

3.2.2 Bioactive glass synthesis

Bioactive glasses were used in these projects to create the composite along with the polymeric AESO-based, hydrogel-based, and PolyHIPE-based matrix. Their use was fundamental to give the final composite the ability to promote bone tissue growth in the derived scaffolds. The synthesis of bioactive glasses was completed following a modified Stöber method [175]. As shown in Table 3, three different bioactive glasses were prepared. In all cases, the process began by stirring together two solutions: one containing ammonium hydroxide (NH_4OH), bidistilled water, and ethanol, and the other consisting of ethanol and tetraethyl orthosilicate (TEOS). This initial mixing promoted the formation of silica particles. Next, the phosphorus precursor, triethyl phosphate (TEP), and the calcium precursor, calcium nitrate tetrahydrate ($Ca(NO_3)_2 \cdot 4H_2O$), were added to the mixture. While maintaining continuous stirring, copper (II) nitrate trihydrate ($Cu(NO_3)_2 \cdot 3H_2O$) was introduced

for the Cu-doped glasses (BG-Cu), while sodium tellurite (Na_2TeO_3) was added for the Te-doped glasses (BG-Te). The resulting sols were then dried at 60 °C for 48 h to remove solvents, followed by calcination at 700 °C for 2 h with a controlled heating ramp of 5 °C/min to eliminate any residual organic compounds, obtaining the final inert compound.

Table 3. Elemental composition of sol-gel synthesised bioactive glasses.

Sample name	**Composition %wt**				
	SiO_2	P_2O_5	CaO	CuO	TeO_2
BG	77	9	14	-	-
BG-Cu	77	9	9	5	-
BG-Te	77	9	9	-	5

The single dispersed particles of BG had a rounded shape with an average dimension of 489 ± 54 nm, as clearly visible from Figure 22, obtained by FESEM microscope. The same shape and similar dimensions were obtained for Cu and Te-doped glass.

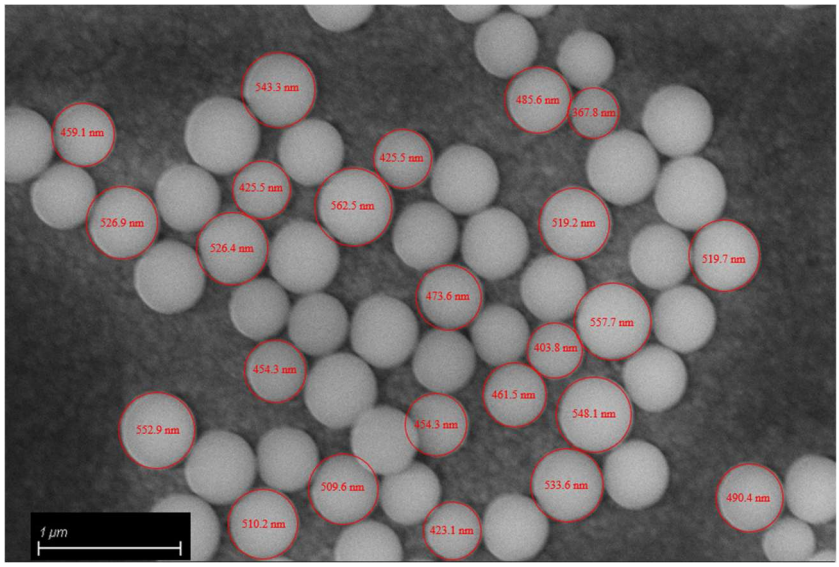

Figure 22. Bioactive glass shape and diameter.

3.2.3 Bioactive glass silanisation

BG were also silanised to increase the compatibility between the reinforcing BG phase and the polymeric matrix. This was done by chemically attaching silanol groups to the particle. To do so, 3-(trimethoxysilyl)propyl methacrylate (TMSPMA) was used. First, 0.5 g of BG powder was dispersed in 2 mL of acetone and subjected to ultrasonic agitation, then centrifuged at 7000 rpm for 5 min to

remove the solvent. This washing cycle was repeated three times with deionised water to ensure complete acetone removal and to activate surface –OH groups. A 20 vol% % solution of TMSPMA in ethanol was then prepared, and three alternative silanization protocols were evaluated: i) stirring for 2 h at room temperature without adjusting pH; ii) stirring for 2 h with the addition of acetic acid to adjust the pH to 5; iii) and prolonged stirring for 24 h at ambient pH. After each treatment, the powder was collected by centrifugation (7000 rpm, 2 min) to remove unreacted silane and then dried at 37 °C for 24 h.

3.2.4 FTIR spectroscopy

The photocuring behaviour of both acrylate resin formulations and hydrogel or polyHIPE precursors was characterised by Fourier-transform infrared spectroscopy (FTIR) using a Nicolet iS50 spectrometer (Thermo Scientific, Milan, Italy). For the acrylate resins, which possess sufficient viscosity after mixing, the liquid was spread into a uniform 32 µm film on a silicon wafer by means of a stir bar; this transmission setup permitted continuous monitoring of reactive group consumption while irradiation in situ. In contrast, hydrogel and polyHIPE precursors could not be deposited as free-standing films, so these samples were analysed in attenuated total reflectance (ATR) mode using the built-in diamond crystal accessory, before and after photopolymerisation. In all cases, the spectral region from 4000 to 600 cm^{-1} was recorded at a resolution of 4 cm^{-1}, using 32 scans per spectrum to maximise signal-to-noise ratio.

Real-time curing kinetics were obtained by equipping the FTIR with a Hamamatsu Lightingcure LC8 UV lamp (365 nm, 50 mW/cm^2). Spectra were collected at regular intervals during continuous UV irradiation. The principal group followed during polymerisation was the decrease in the C=C stretching vibration of the acrylate double bond, monitored around 1600 cm^{-1}. The peak of the aliphatic C–H stretching band at 2950 cm^1, which is known to remain unaffected under UV exposure, served as the reference peak. The ratio of acrylate to C–H peak areas at each time point was calculated and normalised to its initial value at t = 0. Conversion (%) was then determined using:

$$Conversion\ (\%) = \frac{(\frac{A_{group}}{A_{ref}})_{t=0} - (\frac{A_{group}}{A_{ref}})_{t}}{(\frac{A_{group}}{A_{ref}})_{t=0}} \times 100$$

where A_{group} and A_{ref} represent the integrated areas of the acrylate and reference peaks, respectively. All spectra were processed and baseline corrected using OMNIC software (Thermo Fisher Scientific), enabling quantification of the

monomer conversion as a function of UV exposure time. In the case of MCHIT and thiol ene conversion to produce, respectively, hydrogel and polyHIPE materials, the ATR FTIR was performed before and after the photocuring process.

3.2.5 Photo Dynamic Scanning Calorimetry (photo-DSC)

The photocuring behaviour of the formulations was investigated using photo-differential scanning calorimetry (photoDSC). Measurements were performed on a Mettler Toledo DSC-1 system (Milan, Italy), equipped with a Gas Controller GC100 and a Hamamatsu LIGHTINGCURE LC8 mercury UV lamp (Hamamatsu Photonics, Milan, Italy). The UV source was coupled with an optical fibre to focus the radiation directly onto the sample pan. The UV light employed had a wavelength of 365 nm, with the intensity adjusted to either 10 mW/cm² or 50 mW/cm², depending on the experimental setup, by setting the lamp at different percentages of its maximum output.

Samples with a mass between 5 and 15 mg were placed in open aluminium crucibles, while an empty crucible was used as a reference. All experiments were performed at room temperature (25 °C) under a constant nitrogen flow of 40 mL/min to prevent oxygen inhibition and ensure inert conditions. Each photo DSC experiment was composed of an initial isothermal stabilisation step of 2 minutes, a first UV irradiation step of 60 seconds, followed by a second stabilisation step of 2 minutes, and a second identical irradiation step. The second irradiation step was used to establish the baseline. Since the second exposure was performed after complete curing, it enabled the subtraction of non-reactive thermal signals. By subtracting the heat flow curve obtained during the second irradiation from the first, the resulting exothermic profile was attributed exclusively to the crosslinking reaction. All thermograms were processed and analysed using Mettler Toledo STARe software, version 9.2.

3.2.6 Rheology and photorheology

The viscosity and UV-curing behaviour of the formulations were studied using an Anton Paar MCR 302 parallel plate rheometer (Graz, Austria), equipped with a Hamamatsu LIGHTINGCURE LC8 mercury UV lamp (Hamamatsu Photonics, Milan, Italy), coupled with an optical fibre for focused irradiation at 365 nm. All measurements were conducted at a controlled temperature of 25 °C. Photo-rheological measurements were performed to investigate the curing kinetics under UV irradiation. The setup employed a 25 mm diameter upper metal plate, while the lower plate was made of quartz or glass, allowing transmission of UV light through

the sample. The gap between the plates was set to either 300 or 100 μm, depending on the formulation and setup requirements. Samples were subjected to oscillatory shear at a constant frequency of 1 Hz and 1% strain. The UV light was turned on 60 seconds after the start of the measurement to allow system stabilisation. The lamp intensity was set to either 15 mW/cm², 30 mW/cm², or 50 mW/cm², depending on the specific formulation and curing study. During the photo-rheology experiments, both the storage modulus (G′) and the loss modulus (G″) were monitored over time to evaluate the photocuring process. The storage modulus (G′) represents the elastic (solid-like) component of the material, while the loss modulus (G″) corresponds to the viscous (liquid-like) component. Their evolution over time provided information about the crosslinking behaviour during irradiation.

To determine the viscosity and flow behaviour of the uncured formulations, essential for assessing their processability, especially in 3D printing applications, standard rheological tests were performed using the same rheometer. Measurements were conducted using a parallel plate geometry with two 25 mm diameter metal plates, and the gap was set to 1 mm or 3 mm, depending on the formulation. The shear rate was set from 0.01 to 1000 s^{-1}, allowing the determination of the viscosity profile under variable flow conditions.

Using the same instrument, stress relaxation experiments were conducted to verify the dynamic covalent network behaviour of the UV-cured samples. Disc-shaped specimens (10 mm diameter, 0.5 mm thickness) were placed between parallel plates and equilibrated at each test temperature for 15 minutes. A constant shear strain of 3 % was then applied, and the decay of the stress was recorded over time. Tests were performed at temperatures ranging from 180 °C to 220 °C. From the recorded stress–time data, the relaxation modulus G(t) was calculated and normalised by its initial value G_0, defined at the start of strain application. The characteristic relaxation time τ, the critical indicator of dynamic network mobility, was determined as the time required for G(t) to decrease up to 1/e of the initial G_0.

3.2.7 Dynamic mechanical thermal analysis (DMTA)

Dynamic Mechanical Thermal Analysis (DMTA) was performed using a Triton Technology instrument (Netzsch-Gerätebau GmbH, Selb, Germany) to investigate the thermo-mechanical behaviour of the UV-cured materials. The analysis was performed in uniaxial tensile mode, applying a 1 Hz oscillation frequency and an initial displacement of 0.02 mm. The temperature range was set from 0 °C to 100 °C, with a heating rate of 5 °C/min or 3°C/min when more precision in the data acquisition was needed. The starting temperature was reached by cooling the chamber with liquid nitrogen. The test was terminated once the sample reached the

rubbery plateau region, allowing for the identification of the glass transition temperature (T_g), which was determined from the peak of the tan δ curve.

Samples used for the analysis had dimensions of approximately 1.5 × 3.5 × 12 mm or 1 × 8 × 18 mm, depending on the preparation method. The specimens were either fabricated via 3D printing or moulded by pouring the photocurable formulations into silicone moulds and UV-cured with a DYMAX ECE flood lamp (Dymax Europe GmbH, Wiesbaden, Germany) at an intensity of 130 mW/cm².

To estimate the crosslink density (ν_c) of the network, the storage modulus in the rubbery plateau region (T_g + 50 °C) was used according to the formula:

$$\nu_c = \frac{E'}{3RT}$$

Where E′ represents the storage modulus at T_g + 50 °C, R is the universal gas constant (8.314 J·mol^{-1}·K^{-1}), and T is the absolute temperature in Kelvin at which E′ is measured.

3.2.8 Mechanical tests

The mechanical performance of the developed materials was evaluated through tensile and compression tests. These measurements are necessary for determining the potential of the materials for biomedical and tissue engineering applications, where mechanical integrity, elasticity, and deformation behaviour have to be defined.

Tensile properties of the UV-cured and 3D-printed materials were assessed using a universal electromechanical testing machine MTS QTest™/10 Elite (MTS Systems Corporation, Eden Prairie, MN, USA), operated through the TestWorks® 4 software. The instrument was equipped with a 500 N load cell, and the crosshead speed was set to 5 mm/min. Dog-bone-shaped specimens were used, conforming to the ISO 527-5B standard.

Young's modulus (E) was determined from the slope of the linear portion of the initial part of the stress–strain curve. In addition, the tensile strength and strain at break were recorded at the failure point. Each measurement represents the average of five individual specimens**,** ensuring the statistical reliability of the results.

Compressive tests on swollen hydrogel samples were carried out to simulate physiological conditions. The tests were performed on the same MTS QTest™/10 Elite testing machine, equipped with a 10 N load cell, suitable for the low stiffness typically associated with hydrated networks. The samples were pre-incubated in phosphate-buffered saline (PBS) for 24 hours at room temperature to allow complete swelling and mimic in vivo-like conditions.

The hydrogel specimens had a cylindrical shape, with an average diameter of 10 mm and a height of 10 mm. A constant crosshead speed of 5 mm/min was used. The compressive modulus (E_c) was calculated from the linear region of the stress–strain curve. The data represent the mean values of five replicates per material formulation.

The mechanical properties of the polyHIPE scaffolds were assessed via uniaxial compression using an ElectroForce® 3220 Base System (TA Instruments, New Castle, DE, USA). The samples had an average size of 10 × 10 × 4 mm^3 and were tested at a compression speed of 1 mm/min.

For AESO-based formulations, compression tests were conducted on cylindrical scaffolds using a universal testing machine, Instron 5982 (Instron, USA), equipped with a 2 kN load cell. All tests were performed at room temperature, with a constant crosshead speed of 2 mm/min. The specimens were cylindrical**,** with a diameter of 6 mm and a thickness of 2 mm.

3.2.9 Morphological and compositional characterisation

The morphological and compositional characterisation of the developed materials was performed to evaluate their microstructural features, the distribution of the reinforcing phase, and their surface reactivity upon immersion in simulated body fluid (SBF). These analyses are needed to determine not only the quality of the polymer-filler interface but also the bioactivity of the materials, a key parameter for their potential application in bone tissue engineering.

The microstructure and elemental composition of the scaffolds were investigated using field emission scanning electron microscopy (FESEM) equipped with energy dispersive X-ray spectroscopy (EDS, SUPRA™ 40, Zeiss, Oberkochen, Germany). The analysis focused on the visualisation of the morphology of the fracture surfaces, evaluating filler dispersion within the polymer matrix, and detecting the presence of specific elements associated with the bioactive glass or newly formed mineral phases, such as hydroxyapatite (HAp).

Samples were prepared by brittle fracture of cured materials. The fractured pieces were mounted onto aluminium stubs using a conductive adhesive and coated with a thin platinum (Pt) layer via sputtering, to ensure surface conductivity and high-resolution imaging.

The SEM analysis enabled a closer examination of the particle dispersion, matrix–filler interactions, and potential phase separation phenomena.

To assess the in vitro bioactivity of the composite scaffolds, samples were immersed in simulated body fluid (SBF) following Kokubo's protocol [176]. The immersion period and conditions were designed to simulate physiological

environments and evaluate the potential for apatite layer formation, which is indicative of osteoconductive behaviour.

After the SBF immersion, the surface of the samples was analysed via FESEM to detect the formation of hydroxyapatite (HAp)-like structures. These were identified based on their typical cauliflower-like morphology, along with EDS mapping, focusing on the presence of calcium (Ca) and phosphorus (P) ratio.

Further analysis to determine the formation of mineral phases upon SBF exposure was obtained using X-ray diffraction (XRD). Analyses were performed using a Malvern PANalytical X'Pert PRO (Malvern Panalytical Ltd., UK) diffractometer operating in reflection mode.

3.2.10 Contact angle

The surface wettability of bioactive glasses was determined by static contact angle measurements. The water contact angle was measured to evaluate the surface wettability of the scaffolds, as it is directly related to cell adhesion, proliferation, and nutrient exchange. A moderate hydrophilicity is generally considered favorable for biological interactions. Each specimen, formed by pressed powder, was placed on a DSA100 Drop Shape Analyser (Krüss, Hamburg, Germany). A single droplet of ultrapure water (approximately 5 μL) was gently deposited on the sample surface using a calibrated syringe. After allowing the drop to stabilise (typically within 5 s), the left and right contact angles were recorded simultaneously by the instrument software. Three droplets were measured on different regions of each sample to take into consideration any surface heterogeneity, and the mean value was reported as the contact angle. All measurements were performed at room temperature.

3.2.11 Biological evaluation
Cell culturing

All cell culture procedures were performed under sterile conditions in a laminar-flow fume hood. Prior to use, all surfaces were disinfected with 70 % (v/v) ethanol prepared with Milli-Q ultrapure water. Cell culture incubators (Thermo Scientific HERAEUS BB15 and HeraCell 150i) were maintained at 37 °C, 5 % CO_2, and 100 % relative humidity. All media and phosphate-buffered saline (PBS) solutions were pre-warmed to 37 °C in a water bath (Ratek Instruments) before each use.

Human osteosarcoma MG-63 cells (ATCC® CRL-1427™, Manassas, VA, USA) were cultured in tissue-culture flasks (Corning® T75, non-pyrogenic polystyrene) using complete growth medium consisting of high-glucose Dulbecco's

Modified Eagle Medium with GlutaMAX™ (Gibco™, Thermo Fisher Scientific), supplemented with 10 % fetal bovine serum (FBS; Scientifix, SFBS-FR) and 1 % penicillin-streptomycin solution (10000 U/mL penicillin and 10 mg/mL streptomycin; BioReagent grade). Cells were maintained between passages 12 and 15 and subcultured every three days or upon reaching ~80 % confluence. For passaging, the medium was removed by vacuum aspiration (Bernant Company Model 400-3912, Thermo Fisher Scientific), and cells were rinsed with DPBS (Gibco™, 14190-144), and then detached with TrypLE™ Express (Gibco™) for five minutes at 37 °C. Detached cells were collected, counted, and reseeded at the desired density. Confluency and morphology were routinely monitored under an inverted phase-contrast microscope (Nikon Eclipse TS100).

Alternatively, human bone marrow derived mesenchymal stem cells (hbMSCs; PromoCell, C-12974, Heidelberg, Germany) were cultured in low-glucose DMEM (Sigma-Aldrich, Milan, Italy) supplemented with 10 % FBS (Sigma-Aldrich) and 1 % penicillin-streptomycin. Cells were cultured at 37 °C, 5 % CO_2 until reaching 80–90 % confluence. For detachment, 0.25 % trypsin-EDTA in PBS was applied for three minutes at 37 °C, followed by neutralisation with complete medium. Cells were counted and used between passages 3 and 6 for all assays.

Where possible, before the biological evaluation, the scaffolds were sterilised under UV light for 30 minutes on each side.

Cytocompatibility evaluation

The cytocompatibility of the scaffolds was evaluated using metabolic activity assays, fluorescence imaging, and morphological analysis to assess cell viability, adhesion, and morphology over time. Human osteosarcoma MG-63 cells and human bone marrow-derived mesenchymal stem cells (hbMSCs) were seeded directly onto the surface of each scaffold under sterile conditions, using different seeding densities for each material system. 2×10^4 cells per sample were seeded on AESO-BG and silanized reinforced scaffolds, 5×10^4 cells per sample in polyHIPE scaffolds, 2×10^6 cells per sample for hydrogel-based systems.

Following a 4-hour adhesion period at 37 °C in a humidified 5 % CO_2 atmosphere, complete DMEM medium (500–700 µL) was gently added to submerge the samples. Cells were then cultured for 24 and 48 hours or up to 7 days (polyHIPE scaffolds), with medium refreshed every 2–3 days.

Cell metabolic activity was assessed using the resazurin-based alamarBlue™ assay (Life Technologies). A ready-to-use solution (0.015 % w/v in PBS) was added directly to each sample. After 4 h incubation in the dark at 37 °C, fluorescence was measured using a Spark™ spectrophotometer (Tecan,

Switzerland) at excitation/emission wavelengths of 570/590 nm. For PolyHIPE scaffolds, a 440 mM resazurin sodium stock solution (100×) was diluted 1:100 in complete medium to prepare the working solution. After 3 h incubation, 200 µL of medium was transferred to a clear 96-well plate (SpectraPlate™, PerkinElmer), and absorbance was measured at 570 nm (reference: 600 nm) using a VICTOR® Nivo™ microplate reader (PerkinElmer, USA). Values were normalised by subtracting the signal from non-seeded reference scaffolds and reported as mean ± standard deviation (n = 3).

To visualise cell viability and distribution, a Live/Dead staining assay (Viability/Cytotoxicity Kit for mammalian cells, Invitrogen™) was applied at relevant time points. After staining with calcein-AM and ethidium homodimer-1, samples were imaged using an EVOS™ FLoid™ digital fluorescence microscope (Life Technologies).

Finally, cell morphology and adhesion on the scaffold surfaces were evaluated by scanning electron microscopy (SEM). Specimens were fixed with 2.5 % glutaraldehyde in PBS, dehydrated through an ascending ethanol gradient (70 %, 90 % for 1 h each; 100 % for 1–2 h), and dried using hexamethyldisilazane (HMDS). Dried samples were mounted on aluminium stubs using conductive carbon tape and sputter-coated with a thin gold layer (JEOL Smart Coater, Japan). SEM images were acquired at multiple magnifications using a JEOL JSM-IT500 microscope (Japan) under secondary electron detection.

Antibacterial activity

To evaluate the antibacterial properties of the developed materials, *Staphylococcus aureus* (ATCC 43300) was used as a multidrug-resistant Gram-positive bacterium that is commonly used as a model organism in infection-related studies due to its clinical relevance in bone infections. The bacteria were cultured on Luria-Bertani (LB) agar and incubated at 37 °C until distinct and countable colonies formed. After 24 hours, a fresh bacterial suspension was prepared to reach a final concentration of approximately 1×10^5 CFU/mL.

The antibacterial performance of the different scaffold formulations was determined according to the ISO 22196 standard. Each sterile sample was placed in a 24-well plate, and 100 µL of the bacterial suspension was directly pipetted onto the surface. After 24 hours of incubation at 37 °C, non-adherent bacteria were removed by washing with PBS. To assess bacterial viability, the metabolic activity of the bacteria that remained adhered to the samples was measured using the Alamar Blue assay (0.0015% in PBS), which relies on resazurin as an indicator dye.

Viable bacteria were also quantified using the classical colony-forming unit (CFU) counting method. Bacteria were detached from the material surfaces by a combination of sonication and vortexing, then plated on LB agar for overnight incubation. Colonies were counted the next day to estimate the number of viable bacteria per sample surface.

In addition to metabolic and viability assays, scanning electron microscopy (SEM) was employed to observe bacterial adhesion and aggregation on the materials. High-magnification images (×5000) were acquired and subsequently analysed using both SMILE VIEW™ Map software and ImageJ. The images enabled a more detailed analysis of the bacterial distribution, as well as the calculation of the surface area covered by the bacteria. Background noise was minimised through threshold adjustments, and 3D mapping allowed the quantification of the thickness and height of bacterial clusters on the samples.

All experimental data were collected in triplicate, and statistical analysis was done using SPSS software (v.20.0). The normal distribution of the datasets was confirmed using the Shapiro–Wilk test, and homogeneity of variance was assessed with Levene's test. One-way ANOVA was used for comparisons among different groups, followed by Tukey's post hoc test to identify specific differences. Results were considered statistically significant for p-values less than 0.05 (*).

3.3 Soft tissue: Bioactive hydrogels as a versatile platform

Hydrogels represent a unique class of materials in tissue engineering, as they provide a hydrated, tissue-mimetic environment ideal for bioactivity. In this work, we used methacrylated chitosan combined with tellurium-doped, silanized bioactive glass (BG-Te-Sil) to create a composite hydrogel. This combination creates a functional network in which the bioactive glass enhances osteoinduction, while Te-ion release confers antibacterial and anti-inflammatory properties. The methacrylated chitosan backbone ensures an optimal surface for cell attachment, and the gel's structural integrity is fully maintained. The following sections describe the hydrogel synthesis and characterisation, as well as its biological performance. The graphical abstract is represented in Figure 23.

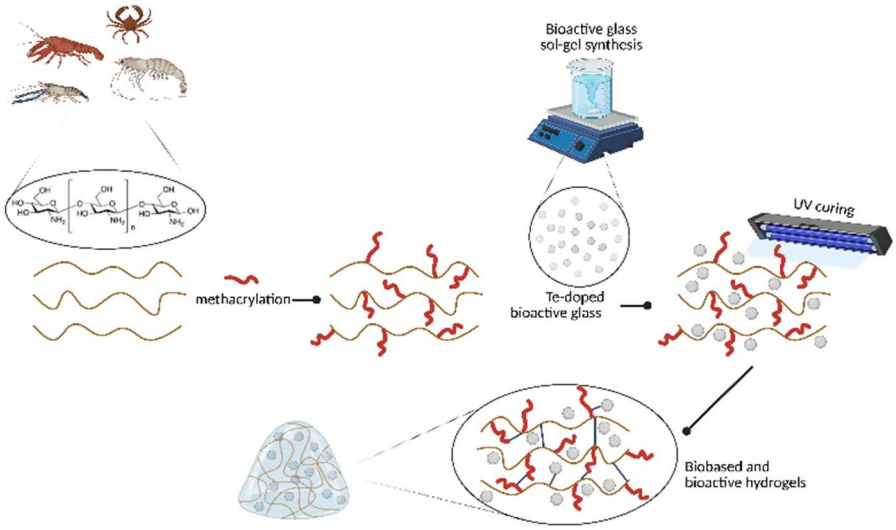

Figure 23. Hydrogel-related graphical abstract.

3.3.1 Methacrylation of chitosan and resin formulation for hydrogel synthesis

Methacrylated chitosan (MCHIT) was synthesised following our previous protocols [166,167]. Chitosan (1.5 wt%) was dissolved in 2 vol% aqueous acetic acid under constant stirring at 50 °C until a homogeneous solution was obtained. Methacrylic anhydride (MA) was then added dropwise at a molar ratio of 1:20 relative to the glucosamine units, and the reaction was allowed to proceed for 4 h at 50 °C. The reaction mixture was dialysed with bidistilled water for 4 days using a 14 kDa cellulose membrane, then freeze-dried to yield a white, cotton-like MCHIT powder.

Once the chitosan was methacrylated, hence ready for a photocuring reaction thanks to the acrylated groups attached, hydrogels were produced. The reaction scheme is reported in Figure 24.

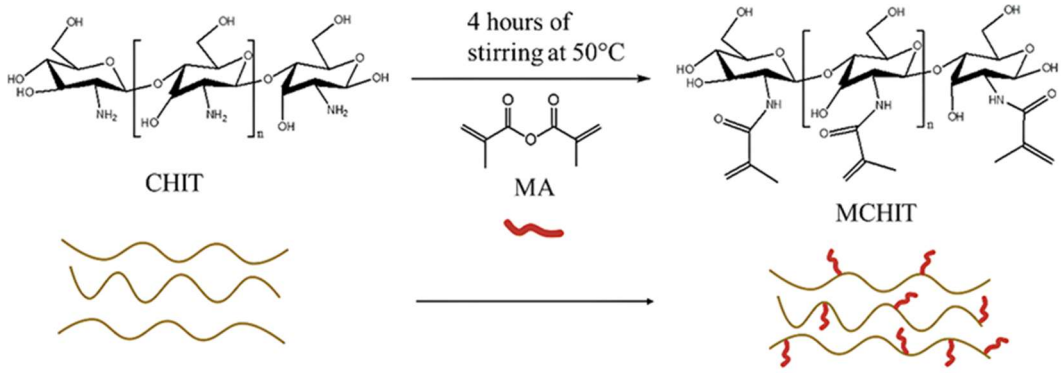

Figure 24. Visual and chemical representation of the methacrylation scheme.

First, it was dissolved 1.5 wt% MCHIT in 2 vol% acetic acid at 50 °C for 2 h. Bioactive glass tellurium-doped and silanised (BG-Te-Sil) were then incorporated at the desired loadings (see Table 4), and the suspension was stirred for an additional hour. Photoinitiator (2-hydroxy-4-(2-hydroxyethoxy)-2-methylpropiophenone, 2 phr) was added, and the mixture was mixed in a Thinky ARE-310 planetary mixer for 20 min. The resulting hydrogel precursor was cast into silicone moulds (10 mm × 10 mm) and cured under a Dymax lamp (365 nm, 145 mW/cm²) for 3 min. The cured hydrogels were freeze-dried to produce porous, white scaffolds (Figure 25).

Table 4. Sample name based on bioactive glass quantity.

Sample name	Amount of BG Te doped and silanised [phr]
MCHIT	0
MCHIT3	30
MCHIT5	50

Figure 25. Hydrogels obtained after the freeze-dry process. From left to right: MCHIT, MCHIT3 and MCHIT5

3.3.2 Gel content and swelling experiments

To assess the gel content of the hydrogels, dried samples were immersed in 5 mL of bi-distilled water and left to soak for 24 hours. This step was meant to extract any unreacted monomers that were not crosslinked during the photocuring process. After the immersion period, the samples were gently touched with absorbent paper and then placed in an oven at 50 °C for an additional 24 hours to ensure that all residual water had evaporated. Once completely dry, the samples were weighed again. The gel content was then calculated as the percentage ratio between the final dry weight (after extraction and drying) and the initial dry weight, using the formula:

$$Gel\ content\ (\%) = \left(\frac{W_f}{W_i}\right) \times 100$$

Swelling behaviour was evaluated by immersing the dry hydrogel samples in 5 mL of bi-distilled water and monitoring their weight gain over time, up to 24 hours. At each time point, the samples were carefully removed, and any excess surface water was gently removed before weighing, ensuring that only the absorbed water was weighed. This allowed to determine how much water the hydrogels were able to uptake, indicating their water retention.

3.3.3 Photocuring process and properties analysis

Methacrylated chitosan was used as the biobased monomer to start the photopolymerisation reaction, relying on the methacrylated groups opening in the radical UV curing, activated by the opening of the photoinitiator.

To fully investigate the methacrylation and the photocuring behaviour of the hydrogel formulations, a full characterisation before and after UV exposure using

FTIR and photorheology was performed. All resin compositions were examined to assess whether the presence of bioactive glass particles interfered with the photocuring process. UV irradiation was performed using a Dymax lamp (145 mW/cm²) for 6 minutes, a time sufficient to ensure the formulation reached a consistent state that allowed it to be removed from the silicone mould.

Figure 26 shows the FTIR spectra of all tested formulations. The presence of acrylate groups around 945 cm^{-1} in the pristine methacrylated chitosan (MCHIT) confirms the success of the methacrylation reaction when compared to unmodified CHIT, which shows no signal in that region. This acrylate peak is clearly visible in the uncured MCHIT sample, indicating the highest content of unreacted double bonds. Upon UV exposure at 365 nm, a clear reduction in the 945 cm^{-1} peak is observed across all cured formulations, confirming that photopolymerisation has taken place.

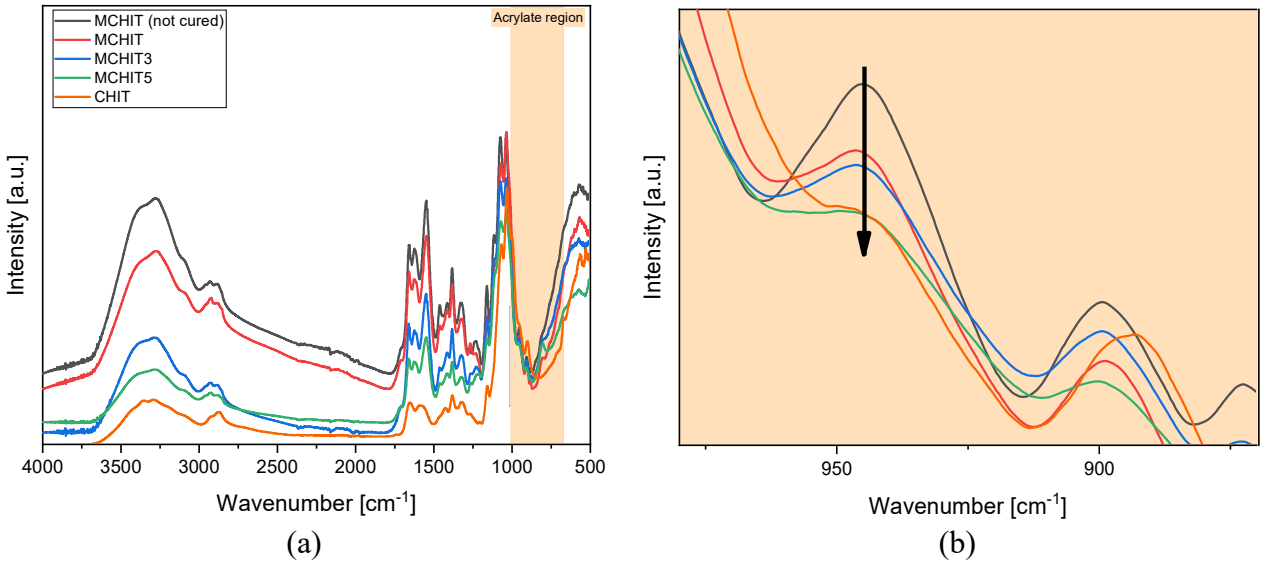

Figure 26. Overall FTIR spectra of all the tested formulations; (**b**) is the magnification of (**a**) in the range from 1100 to 830 cm^{-1}. The black arrow represents the acrylate peak decrease after curing.

To support the FTIR analysis and further confirm the photocuring process, photorheology tests were done on all formulations. In these experiments, the liquid resins were exposed to UV light while their rheological behaviour was continuously monitored. The results are shown in Figure 27.

UV irradiation began 60 seconds after the start of each test. All formulations exhibited a consistent behaviour: after a short delay of approximately 10 seconds, the curing reaction proceeded quickly and was completed within about 180 seconds under 365 nm UV light at 145 mW/cm².

As expected, the initial storage modulus (G') in the dark phase, which reflects the material properties before curing, was lower for MCHIT. In contrast, the formulations containing bioactive glass exhibited higher initial G' values, attributable to the ceramic particles increasing the overall viscosity of the resin. To investigate this further, a viscosity test was performed across a range of shear rates. As shown in Figure 27, both MCHIT and MCHIT3 displayed comparable shear-thinning behaviour, while MCHIT5 demonstrated a marked increase in viscosity, confirming the thickening effect of higher glass content.

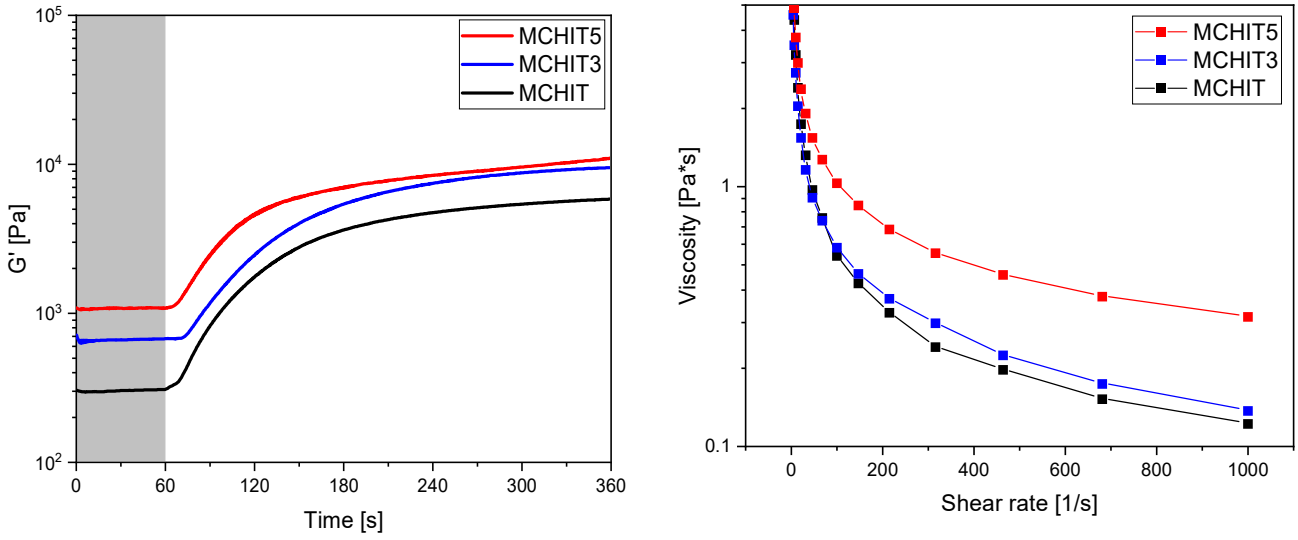

Figure 27. Photorheology and rheology experiments performed on the hydrogel BGs-containing formulations.

After confirming the successful photocuring of the hydrogel, they were then manufactured. The precursor resin was poured into cylindrical silicone moulds (1 cm in height and diameter) for shaping. Once cured, the samples were carefully removed and immediately transferred to a lyophiliser to dry them while preserving their structure. Air drying in a fume hood was avoided, since, as shown in Figure 28, this method leads to structural collapse and deformation of the original shape.

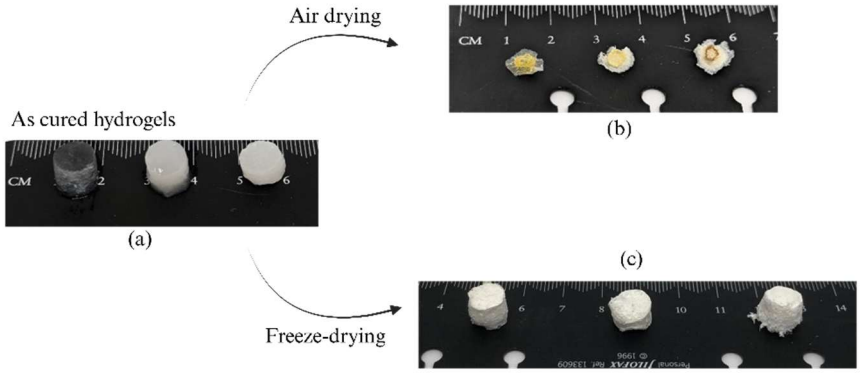

Figure 28. Different stages after the hydrogels production, from left to right are positioned MCHIT, MCHIT3, MCHIT5. (a) represents the cured hydrogels, while (b) and (c) represent the respective dry forms of them.

To verify whether the hydrogels were fully cured, a gel content test was carried out. After immersing the samples in distilled water for 24 hours, they were dried and weighed to determine the percentage of uncured monomer. The results confirmed that all formulations achieved nearly complete curing, since all values obtained resulted above 99.8 ± 0.1 % of gel content. These high gel content values confirm that no unreacted acrylate groups remain in the cured hydrogels, which is crucial for ensuring that no cytotoxic species leach during in vitro testing.

Following confirmation of curing, the hydrogel microstructure was examined using FESEM. Samples were frozen in liquid nitrogen, fractured to expose the internal cross-section, and sputter-coated with a thin platinum layer to enhance conductivity. Representative images of all hydrogel formulations are shown in Figure 29.

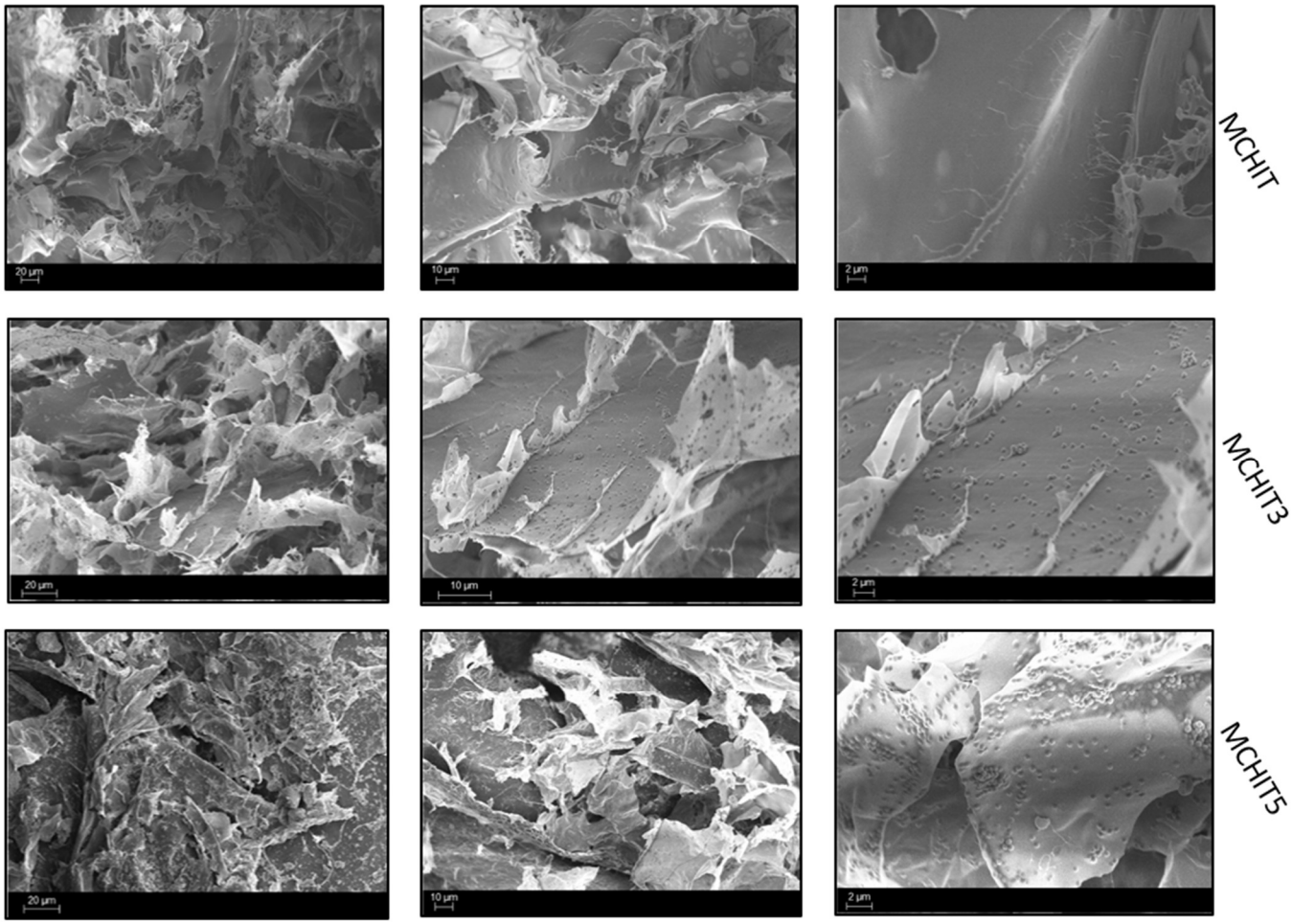

Figure 29. FESEM image of hydrogel filled with BG at different concentrations. Each row represents three different magnifications of the same sample.

From the images, it is clear that the bioactive glass particles are well dispersed throughout the matrix, with no observable voids, indicating good interfacial adhesion to the polymer phase. This strong integration is likely due to the silanisation of the glass particles, which improves compatibility with the organic matrix by promoting covalent interaction via their aliphatic chains. In the MCHIT5 samples, the higher filler content leads to a greater number of visible particles at the surface, but they remain homogeneously distributed. Only a minimal degree of aggregation is observed.

To confirm the successful incorporation of tellurium into the bioactive glass, EDS analysis was performed on a representative sample, selecting a BG particle cluster (Figure 30). The elemental spectrum clearly shows the presence of Te, confirming its inclusion within the filler composition.

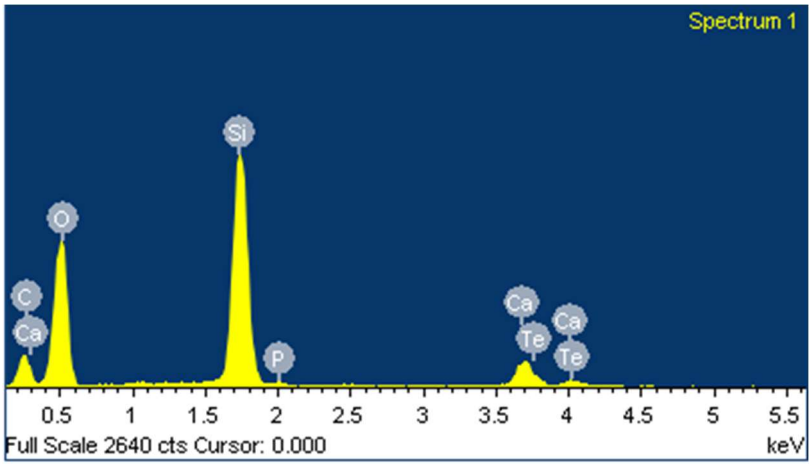

Figure 30. EDS measurement of the BG-Te particles where the main peaks of the glass elements are reported.

Once the bioactive glass particles were proven to be well integrated into the metacrylated chitosan network, the mechanical performance of the hydrogels was tested in their hydrated state. Samples were first swollen in PBS, then subjected to uniaxial compression to measure their resistance to deformation. Figure 31 and Table 5 summarise the compressive modulus results.

Table 5. Compression modulus values obtained from compression tests.

Sample Name	Compressive Modulus [kPa]
MCHIT	87 ± 25
MCHIT3	246 ± 51
MCHIT5	80 ± 34

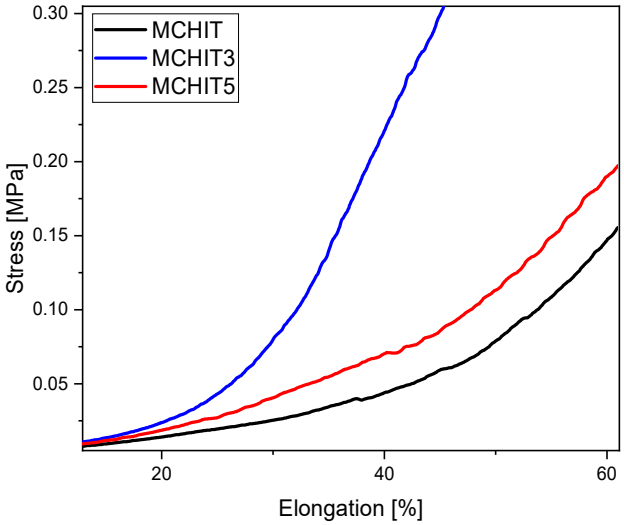

Figure 31. Graphical representation of mechanical compression tests performed across all the hydrogel BG-filled formulations. Each curve represents a mean value derived from 5 different measurements.

The incorporation of 30 phr of BG-Te-sil more than doubled the hydrogel compressive modulus, reflecting the ceramic phase ability to bear load. However, further increasing the filler content to 50 phr unexpectedly reduced stiffness. The drop was attributed to local particle aggregation, which disrupts the uniform network and decreases the reinforcing effect, an observation consistent with similar reports in the literature [177,178]. Even so, the 50 phr formulation still outperforms the MCHIT reference, demonstrating that an optimal filler loading exists between mechanical reinforcement and structural integrity.

3.3.4 Biological evaluation

To assess the suitability of the BG-Te-Sil-reinforced hydrogels for regenerative applications, we evaluated their interaction with both bone-derived cells and pathogenic bacteria. Methacrylated chitosan hydrogels mimic the hydrated extracellular matrix of soft tissues; however, by incorporating tellurium-doped, silanized bioactive glass, they also gain osteoconductive, anti-inflammatory, and antimicrobial functionality. Such composite hydrogels can be directly moulded or injected into bone defects, where the sustained release of Ca^{2+}, PO_4^{3-}, and Te^{2+} ions promote hydroxyapatite formation and inhibits microbial colonisation.

In this section, it was first characterised cell viability, adhesion, and proliferation on MCHIT3 and MCHIT5 scaffolds using primary human bone

marrow-derived mesenchymal stem cells (hBMSCs). It was then tested how the material can resist colonisation by multi-drug-resistant *Staphylococcus aureus*.

Cytocompatibility evaluation

To evaluate cytocompatibility, human bone marrow-derived mesenchymal stem cells (hBMSCs), chosen due to their relevant role in bone regeneration, were encapsulated within 1 cm × 1 cm hydrogel cylinders of MCHIT, MCHIT3, and MCHIT5. To prevent cell detachment from the network, the cells were suspended in a 3 mg/mL collagen solution prior to seeding (Figure 32a). At 24, 48, and 72 hours post-seeding, metabolic activity was measured by alamarBlue assay, using MCHIT as the reference control. No statistically significant differences were observed among the three formulations at any time point (Figure 32b), indicating that neither 30 phr nor 50 phr of BG-Te-Sil affects hBMSC metabolism. After 72 hours, cell viability and spatial distribution were assessed by combining live/dead staining with NucBlue nuclear labelling, three-dimensional fluorescence imaging, and Hematoxylin/Eosin staining (Figure 32c). The live/dead assay showed predominantly green-fluorescent cells, confirming high viability, while confocal reconstruction revealed uniform cell dispersion throughout the hydrogel. Hematoxylin /Eosin staining revealed round, dark-red nuclei embedded within a light-red fibrillar matrix, validating the fluorescence findings.

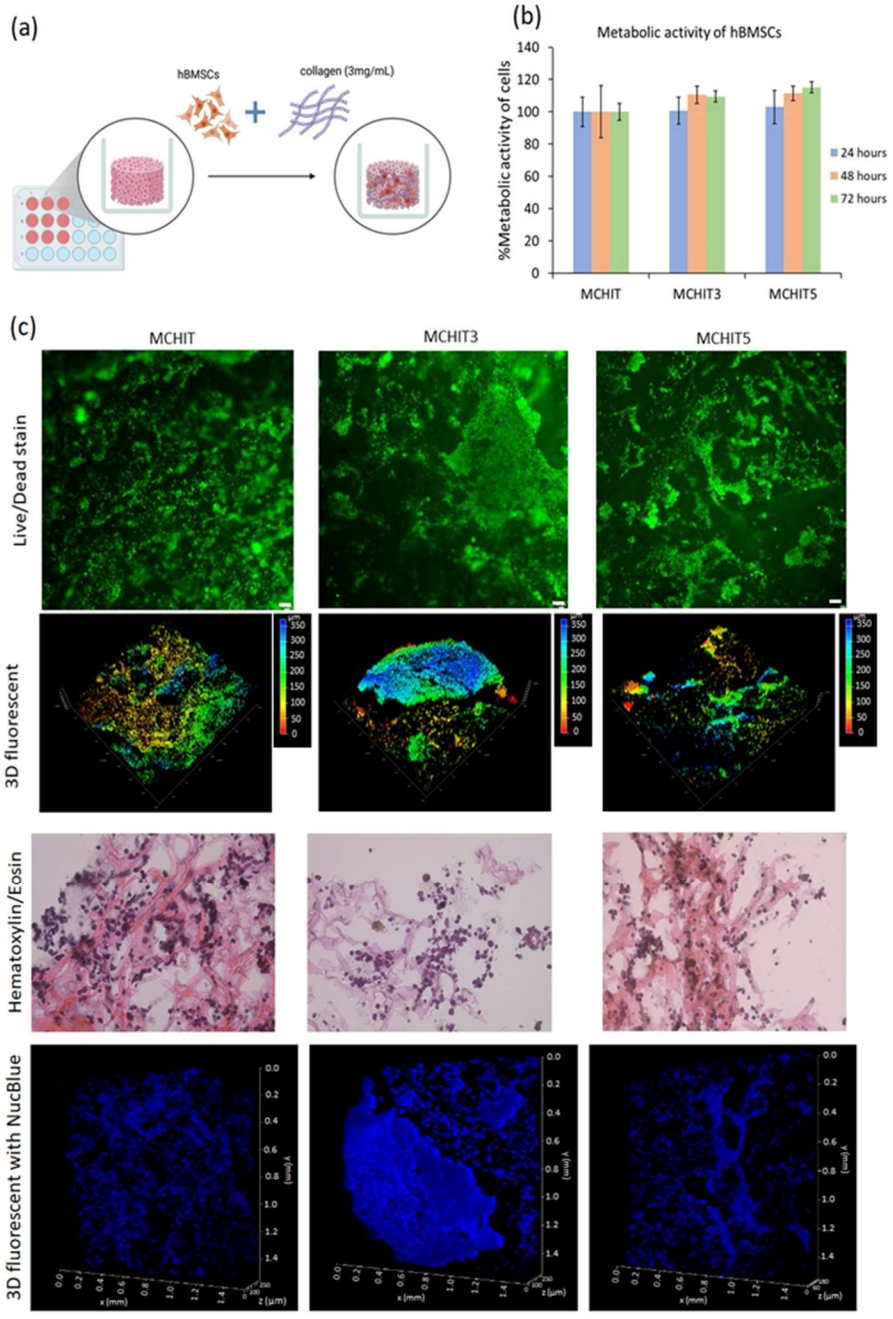

Figure 32. Cytocompatibility evaluation of hydrogel scaffolds after 24-72 h incubation. (a) Represent a schematic diagram illustrating the cells seeding in the hydrogel, (b) Metabolic activity of cells at each time point. Data are normalised to MCHIT (control). (c) Top panel: live/dead fluorescent staining, scale bar=50 um, middle panel: 3D fluorescent images, bottom panel histological staining.

Antibacterial Activity Assessment

The pathogenicity of multidrug-resistant *S. aureus* in tissue implant infections and its challenge in implant-associated infections, especially its ability to form resilient biofilms, is well documented. To test the effect of Tellurium on the antibacterial efficacy of the hydrogel scaffolds, 1 mL of *S. aureus* suspension was directly applied onto MCHIT, MCHIT3 and MCHIT5 samples, allowing the bacteria to adsorb and penetrate the network (Figure 33a). After 24 hours of incubation, the hydrogels were then transferred to new wells, and antibacterial activity was quantified by adding the AlamarBlue reagent directly to each well. The viable bacterial cells were then detached and counted, with the results shown in Figures 33b and 33c. MCHIT5 exhibited a statistically significant reduction in bacterial metabolism compared to the MCHIT control ($p < 0.05$), even though the CFU counts for MCHIT3, MCHIT5, and MCHIT did not differ significantly.

SEM analysis (Figure 33d) revealed extensive biofilm coverage on MCHIT, whereas biofilm on MCHIT3 and MCHIT5 was confined to internal pores, most notably in MCHIT3. Tellurium antibacterial action has been attributed to its uptake by bacterial cells and subsequent inhibition of enzymes essential for growth and biofilm development. It is possible that silanization in BG-Te-Sil reduces Te availability to the bacteria. However, MCHIT5, which contained the highest BG-Te-Sil loading, showed the greatest decrease in metabolic activity, likely due to its higher particle density.

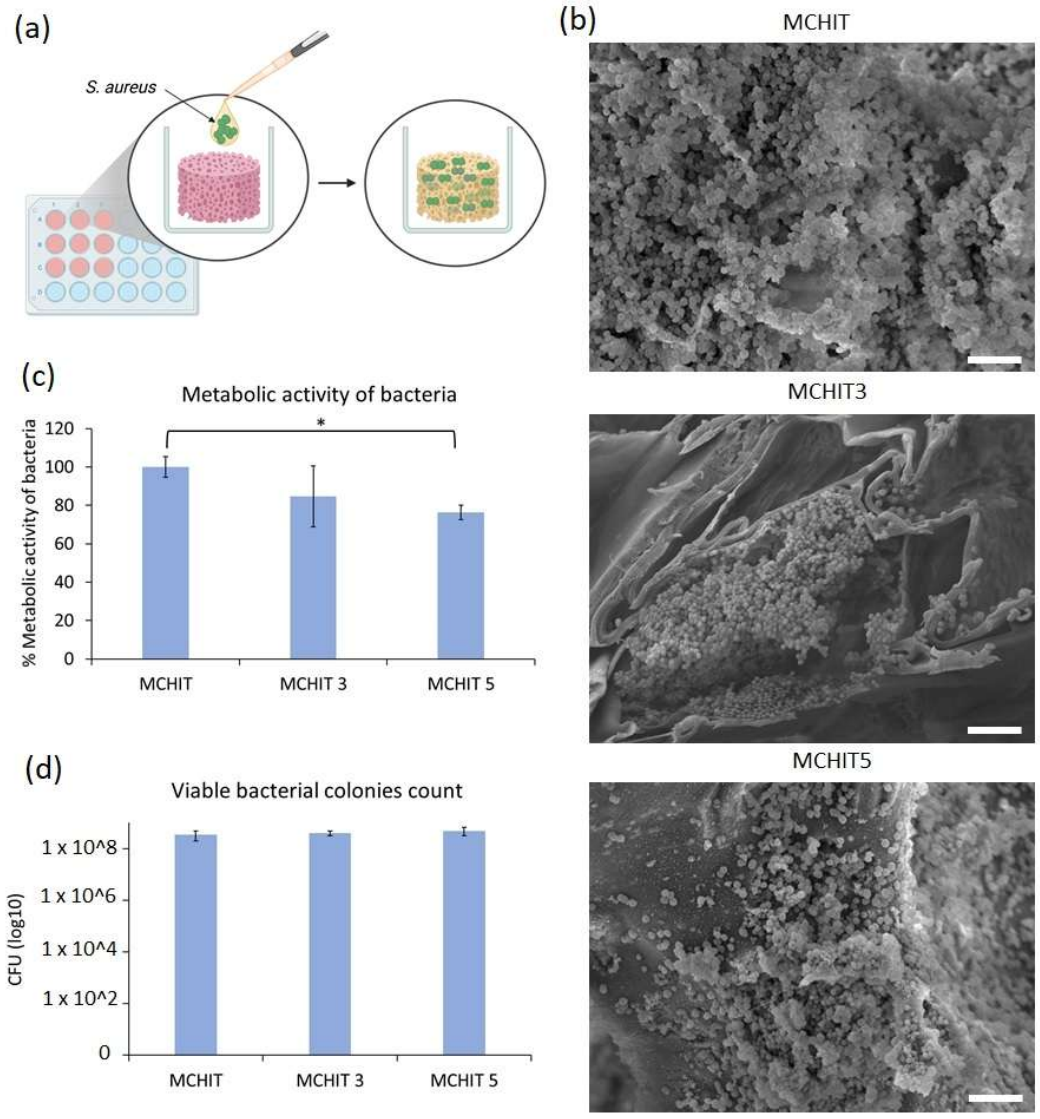

Figure 33. Antibacterial activity of hydrogel samples against MDR S.aureus after 24h of incubation: (a) schematic diagram of infection samples with bacteria, (b) SEM images, scale bar=5um (c) bacterial metabolic activity normalised to MCHIT, *represent $p<0.05$. (d) viable bacterial colony count adhered to and within the samples.

Anti-Inflammatory Characterisation

Bone is a tissue that is continuously remodelled, and the equilibrium between the mineralising activity of osteoblasts and the resorptive function of osteoclasts is fundamental to be maintained. This balance can be disrupted by various factors, including hormones, cytokines, and reactive oxygen species (ROS) [179]. Tellurium and its oxide, TeO_2, have been recognised for their anti-inflammatory

properties, with numerous studies documenting their ability to mitigate inflammatory responses [132,135,180]. In this hydrogel system, incorporating 30 phr and 50 phr of silanized Te-doped bioactive glass (BG-Te-Sil) not only reinforces the methacrylated chitosan matrix and confers antibacterial properties, but also can introduce anti-inflammatory functionality.

To determine this anti-inflammatory effect, hBMSCs were encapsulated within MCHIT3 and MCHIT5 hydrogels and exposed to 300 μM H_2O_2 for seven days to simulate oxidative stress. At the end of this period, expression changes in key pro- and anti-inflammatory genes have been quantified (IL-1β, TNF-α, IFN-γ, PGES-2, and IL-10) by qRT-PCR, using the qRT-PCR method. A fold-change greater than 1 indicates upregulation, while values below 1 denote downregulation. As shown in Figure 34, both MCHIT3 and MCHIT5 scaffolds significantly downregulated TNF-α and IFN-γ, with MCHIT5 also reducing IL-1β and PGES-2 expression most effectively (Figures 34a–d). These results align with the known mechanism of Te(IV) species, which scavenge ROS such as H_2O_2 and hydroxyl radicals by cycling through lower oxidation states, thus preventing activation of pro-inflammatory transcription factors.

p

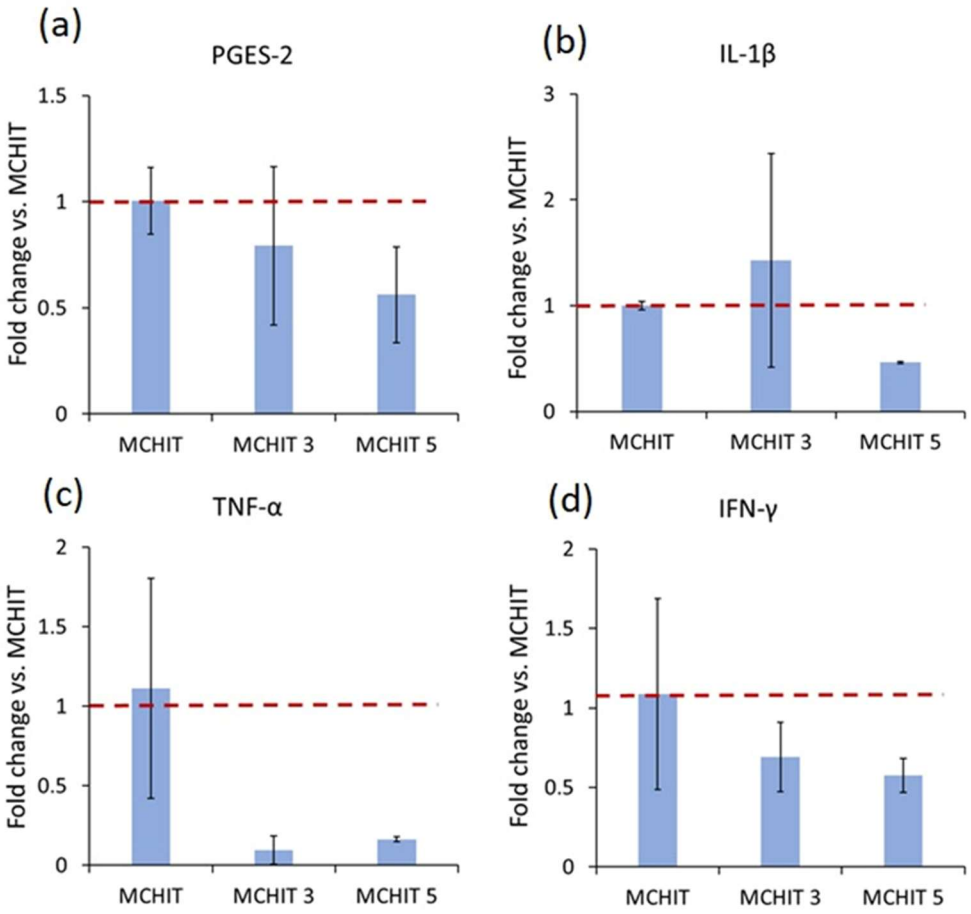

Figure 34. Fold changes in the expression of genes encoding pro-inflammatory responses. The red line represents a fold-change value of 1, where any value above 1 is considered upregulated, and any value below 1 is considered downregulated: (a) Prostaglandin-E Synthase 2 (PGES-2); (b) Interleukin-1 beta (IL-1β); (c) Tumour necrosis factor-alpha (TNF-α); (d) Interferon-gamma (IFN-γ). Gene expression of Glyceraldehyde 3-phosphate dehydrogenase (GAPDH) was used as the housekeeping gene.

Conclusion

According to the results, this study demonstrates that BG-Te-Sil reinforced hydrogels combine mechanical strength, cytocompatibility, and inflammation control, making them promising candidates for bone-implant applications.
In summary, the methacrylated chitosan-based hydrogel scaffolds reinforced with silanised Te-doped bioactive glass demonstrated improved mechanical properties, efficient crosslinking and cytocompatibility, along with promising anti-inflammatory responses. In particular, the addition of both 30 and 50 phr BG-Te-Sil in the formulation contributed to a reduction in bacterial metabolic activity and downregulation of key pro-inflammatory genes, supporting the multifunctionality of these hydrogels for tissue implant applications. Despite these results, further optimisation is required to improve their antimicrobial efficacy, for instance by trying to increase the Te content within the formulation, especially against multidrug-resistant bacteria, without compromising the mechanical performance. Having established the potential of BG-reinforced hydrogels, the next section focuses on the development of highly porous polyHIPE scaffolds incorporating a similar composition of bioactive glasses.

3.4 Soft–hard tissue engineering transition: polyHIPE materials as porous platform for composite scaffold manufacturing

With the hydrogel system established as a versatile, bioactive platform and after having defined the positive effect of BG in a hydrogel platform, we then turned to a porous polymeric matrix that offers enhanced robustness and interconnected porosity, a key feature that is fundamental to support vascularisation and bone growth. As previously described, these systems aim to combine the architectural advantages of high internal phase emulsions with tunable mechanical properties and bioactivity, offering an alternative route for bone tissue engineering applications where higher porosity and interconnected structures are needed. Polymerised high internal phase emulsions (polyHIPEs) combine the advantages of emulsion templating with fast photocuring, yielding light-weight, highly porous foams where pore architecture can be finely tuned by controlling emulsion formulation and curing conditions. By embedding bioactive glass into a biobased polyHIPE matrix, we aim to marry the osteoconductive and antimicrobial benefits demonstrated in our hydrogels with the mechanical strength and mass transport properties of a foam. The next section details the design, synthesis, and characterisation of these composite polyHIPE scaffolds, evaluating their morphology, mechanical performance, and support of osteoblast-like cell activity.

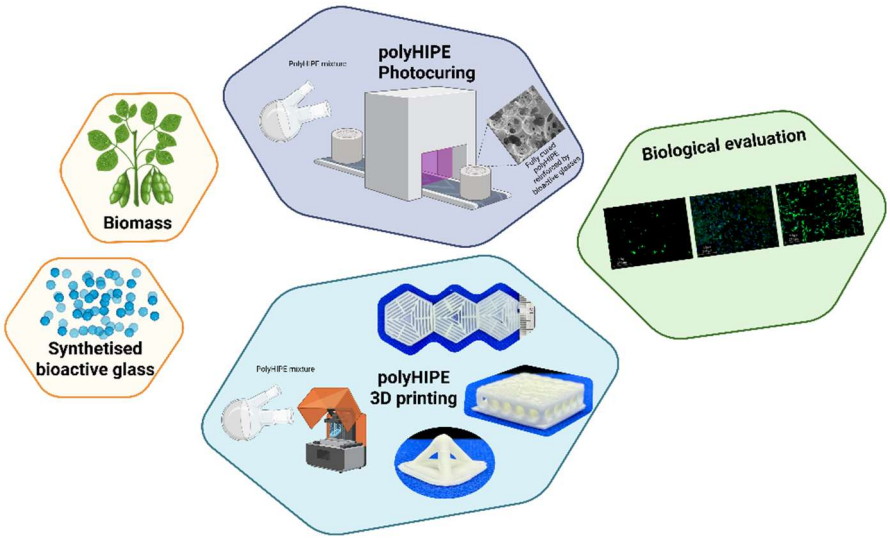

Figure 35. Graphical abstract about polyHIPE project.

3.4.1 Resin formulation and high internal phase emulsion polymerisation

The composite polyHIPE scaffolds were synthesised by adapting established high internal phase emulsion protocols with several modifications for bioactive glass incorporation [181–184]. First, 5 wt% Hypermer B246 surfactant (relative to the oil phase) was dissolved in 1,2-dichloroethane (DCE; 50 vol% of the oil phase) using a vortex mixer. To this solution, acrylated epoxidised soybean oil (AESO) and trimethylolpropane tris(3-mercaptopropionate) (TMPTMP) were added in a 1:1 molar ratio of acrylate to thiol functional groups, forming the hydrophobic phase. Photoinitiator (Phenylbis(2,4,6-trimethylbenzoyl) phosphine oxide, 2 phr) and the desired loading of bioactive glass used in the basic composition without any doping were then introduced. The mixture was transferred into a 250 mL, two-necked, round-bottom flask equipped with a PTFE overhead paddle and stirred at 300 rpm in an ice bath.

Milli-Q water was added dropwise (80 vol% relative to the organic phase) at 45 mL/h using a syringe pump to generate the HIPE. After completing the water addition, the emulsion was homogenised for a further 5 minutes. For moulded samples, the HIPE was poured into PTFE cylinders (25mm diameter, 50 mm height) between glass plates. Polymerisation was achieved by subjecting the moulds to a belt conveyor UV curing system (Heraeus LC6B with UV Light Hammer 6) at 500 mW/cm² for 20 s per side. For printed samples, the fresh emulsion was used directly in a DLP 3D printer.

Regarding post-curing, all scaffolds underwent acetone soaking for 24 hours to prevent the rapid evaporation of DCE and remove any uncured monomer, followed by Soxhlet extraction in dichloromethane for 24 hours to open and interconnect the pore network. To avoid shrinkage due to rapid solvent removal, samples were then immersed in ethanol for 24 hours before final drying in a vacuum oven for an additional 24 hours. The cured foams were sectioned into circular slices (0.2–2 mm thickness) using a vibratome for subsequent analysis. The post-curing process is shown in Figure 36.

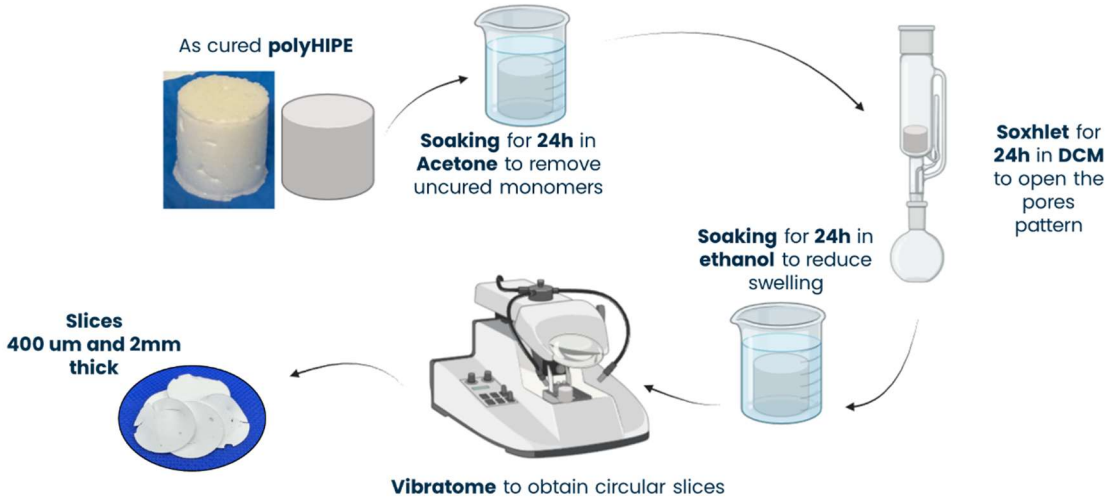

Figure 36. Post curing process of polyHIPE materials.

Three formulations were prepared by varying the bioactive glass content, obtaining "Pristine" formulation, without any BG content, PHI15 with 15phr (per hundred resin) of BG, and PHI30 with 30phr of BG.

3.4.2 Photocuring behaviour

To assess the photocuring behaviour of polyHIPE formulations, real-time photocuring experiments under 365 nm UV light (10 mW/cm²) were performed by means of a rheometer equipped with a UV lamp. As reported in Figure 37a, all formulations reacted almost immediately upon irradiation, with polymerisation completing in 5 to 10 seconds, a time typical for the rapid and efficient thiol-ene crosslinking mechanism.

The viscosity of each emulsion prior to photopolymerisation was evaluated under the same instrumentation. Figure 37b and Table 6 summarise the resulting data. The pristine polyHIPE exhibited the highest viscosity, reflecting its superior emulsion stability in the absence of particulate fillers. Introducing 15 phr of bioactive glass slightly reduced viscosity, likely due to decreased emulsion stability and consequently droplet size distributions. However, increasing the glass content to 30 phr reversed the trend, increasing the viscosity once more as the higher ceramic load improved the overall resistance to flow.

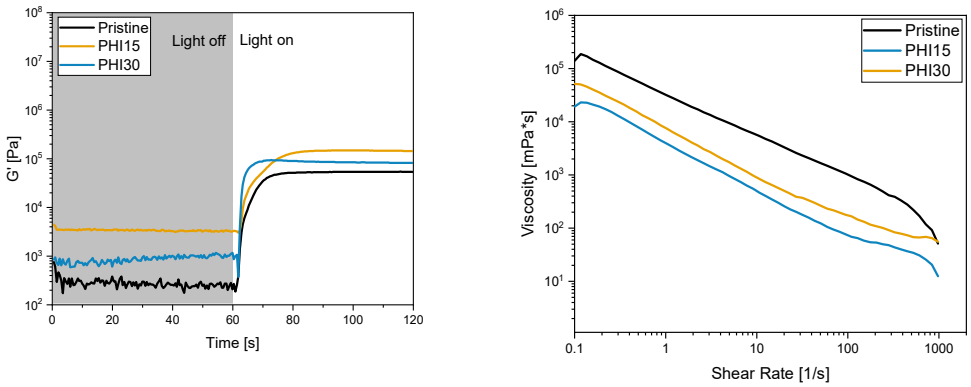

(a) (b)

Figure 37. a) Photorheological measurement recorded under UV exposure (365 nm) applied after 60 seconds from the start of the measurement. b) Viscosity profiles of the tested formulations measured over a shear rate range from 0.1 to 1000 s^{-1}.

Table 6. Viscosity values determined from rheology measurements across all formulations.

Sample name	Viscosity [Pa*s] at $30s^{-1}$
Pristine	2.2 ± 0.2
PHI15	0.2 ± 0.0
PHI30	1.2 ± 0.4

Despite these variations, all formulations possessed viscosities within the optimal window for 3D printing, confirming that both pristine and BG containing polyHIPE emulsions can be processed by mSLA 3D printing.

3.4.3 PolyHIPE scaffolds morphology

After having manufactured the polyHIPE discs, the internal structure was analysed by means of scanning electron microscopy. Representative FESEM images (Figure 38) revealed the characteristic open-cell structure imparted by the high internal phase emulsion approach. In particular, Figure 38b demonstrates that the glass particles are evenly dispersed throughout the polymer matrix, confirming that the addition of the inert phase did not compromise the overall scaffold porous structure.

Within these polyHIPE networks, the primary pores, which are the cavities templated by the internal water phase, reflect emulsion stability and processing conditions, while secondary pores derive from partial coalescence and polymer film

rupture, providing interconnectivity between primary voids. To compare pore architectures quantitatively, the diameters of 100 randomly selected primary pores in each scaffold were measured by using ImageJ software and a statistical correction factor of $2/\sqrt{3}$ was applied to account for sectioning errors. The pristine polyHIPE exhibited an average primary pore diameter of 8.0 ± 2.7 µm, while the addition of glass particles increased the dimension to 10.2 ± 4.4 µm. This enlargement is attributed to the increase in emulsion viscosity, which derives from the BG addition, which locally disrupts droplet uniformity and promotes slight coalescence. On the other hand, secondary pore sizes remained essentially unchanged (2.2 ± 0.9 µm in all formulations), indicating that their formation is governed by film-rupture mechanisms, which are not sensitive to the presence of the inorganic phase.

Elemental mapping by EDS (Figure 38) further confirmed the homogeneous distribution of glass within the scaffold. Oxygen, silicon, and calcium signals coincide with the bright inclusions seen in SEM, verifying their identity as bioactive glass. Phosphorus mapping was not performed to avoid interference with the iridium coating signal. Together, these morphological and compositional analyses demonstrate that the polyHIPEs produced are highly porous, and the BG particles can be well incorporated into the structure without compromising the characteristic porous structure.

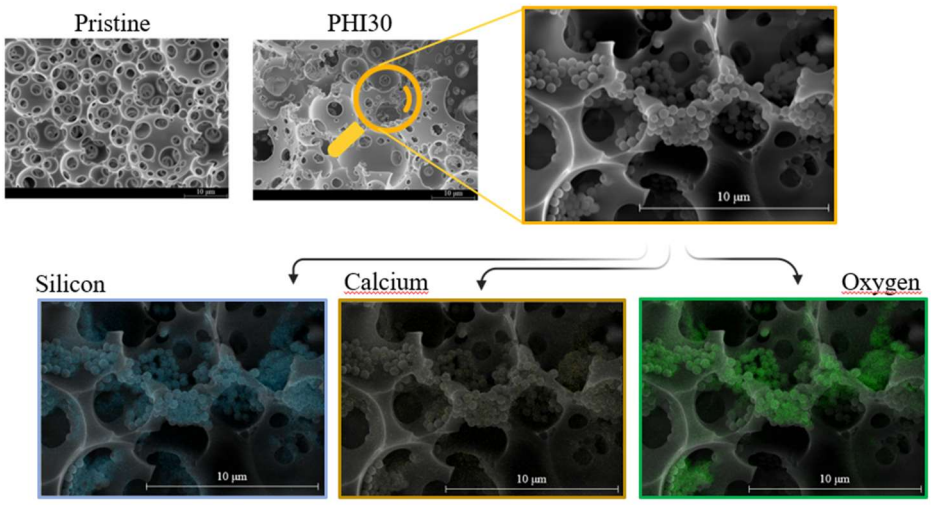

Figure 38. a) Field Emission Scanning Electron Microscopy (FESEM) and EDS image of the pristine polyHIPE scaffold and PHI30 sample, illustrating typical morphological features of bioactive glass-containing polyHIPE scaffold along with elemental distribution of the principal components of BG.

3.4.4 Surface wettability and gel content

To evaluate the surface and network properties of our polyHIPE scaffolds, we measured water contact angles and performed gel content analyses. Static contact angle measurements (Figure 39a) confirmed that the pristine polyHIPE is hydrophobic, with a contact angle of 123 ± 3°, consistent with its crosslinked thiol–ene chemistry along with the porous structure. Introducing bioactive glass particles progressively increased surface wettability, reducing the contact angle to 116 ± 1° for PHI15 and 102 ± 5° for PHI30. Although the larger primary pores in the filled scaffolds might be expected to trap air and increase hydrophobicity, the opposite trend was observed. This decrease in hydrophobicity derives from the glass particles surface hydroxyl groups, which become the dominant interface with water and promote wettability, a parameter that is desired during biological applications.

Gel content was also examined (Figure 39b) to determine the residual monomer content by immersing the scaffolds in dichloromethane (DCM) for 72 hours to. Each formulation exhibited almost complete gel fractions, confirming that thiol–ene photopolymerisation and post-curing processes removed almost all monomers, avoiding the concern of leaching of unreacted species in biological trials.

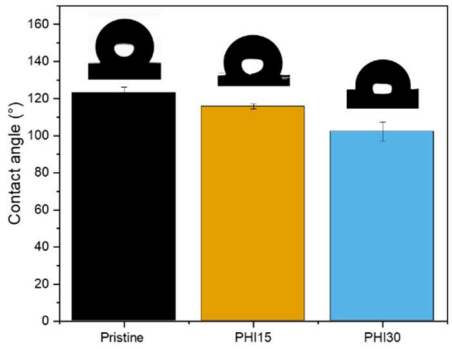

Figure 39. a) Contact angle measurement performed on pristine and BG-reinforced polyHIPE scaffolds: 123±3° for pristine, 116±1° for PHI15, 102±5° for PHI30. b) Gel content test performed on pristine and BG-reinforced polyHIPE scaffolds.

3.4.5 Thermal stability

Thermal stability and ceramic loading of the polyHIPE scaffolds were evaluated by thermogravimetric analysis (TGA) under a nitrogen atmosphere. Samples were heated from 25 °C to 900 °C at a controlled rate, enabling both the assessment of degradation behaviour and the quantification of residual inorganic

content. As shown in Figure 40, the pristine polyHIPE retained approximately 4 wt % of its mass at 900 °C, reflecting char formation from the thiol–ene network.

Incorporation of bioactive glass led to an increase in the residual mass, rising to 11 wt % for PHI15 and 20 wt % for PHI30. This trend directly corresponds to the BG loadings and confirms that the glass phase remains thermally stable during the test.

The T_5% value for all samples above 310 °C demonstrates that the thiol–ene crosslinked networks retain their integrity well above sterilisation temperatures, a crucial attribute for biomedical scaffolds.

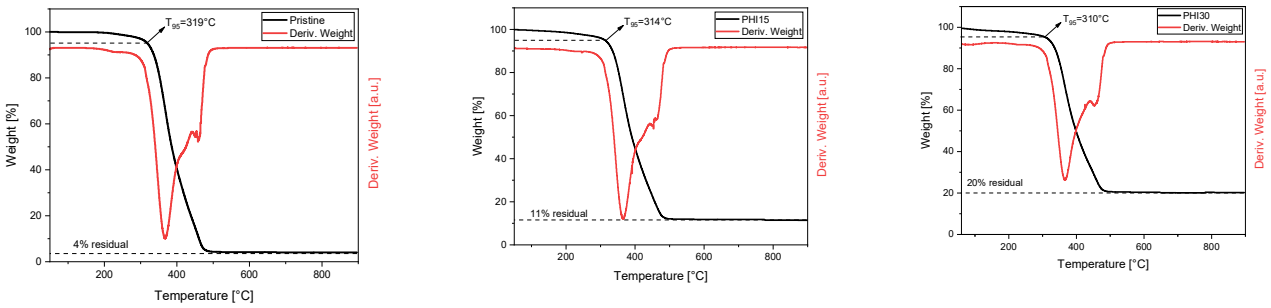

a) b) c)

Figure 40. Thermal gravimetric analysis performed on pristine formulation (a), PHI15 (b), and PHI30 (c). All analyses ranged from 25°C to 900°C in an inert atmosphere.

3.4.6 Thermo-mechanical properties

To assess the thermo-mechanical performance of polyHIPE scaffolds, Dynamic Mechanical Thermal Analysis (DMTA) and uniaxial compression testing were performed. DMTA was used to determine the viscoelastic response and the glass transition temperature (T_g) of each UV-cured formulation. As shown in Figure 41, incorporating increasing amounts of BG progressively raises T_g from ~22 °C in the pristine polyHIPE to ~30 °C in PHI30. This upward shift reflects restricted polymer chain mobility derived from physical constriction caused by the ceramic particles and the thiol–ene network, resulting in a more rigid composite.

From a biomedical perspective, these Tg values, which lie just below physiological temperature (~37°C), suggest that in vivo, the scaffolds will be in a viscoelastic, rubbery state, offering both mechanical compliance and resilience under dynamic loading conditions.

To quantify stiffness directly, uniaxial compression tests was performed, and the relative compressive modulus was determined (Figure 41a and Table 7). The pristine formulation exhibited a modest modulus of 64 ± 5 kPa, suitable for non-load-bearing applications. Reinforcement with 15 phr and 30 phr of BG increased

the modulus to 136 ± 16 kPa and 174 ± 25 kPa, respectively, with a nearly 270 % enhancement in PHI30. The improvement underscores the role of the rigid BG phase as a mechanical reinforcement within the porous network.

Beyond stiffness, all formulations demonstrated excellent elastic recovery: after 100 % compressive strain, the scaffolds returned to their original dimensions upon unloading (Figure 41c).

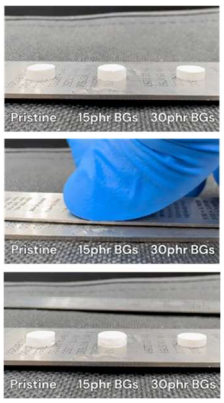

(a) (b) (c)

Figure 41. (a) represent the compression tests obtained across the formulations, while (b) shows the glass transition temperature obtained by DMTA curves. (c) shows the complete elastic recovery of polyHIPE after complete compression.

Table 7. Thermomechanical values obtained from DMTA and compression tests.

	Pristine	**PHI15**	**PHI30**
Elastic modulus [kPa]	64±5	136±16	174±25
Glass transition temperature [°C]	22±1	23±3	30±4

3.4.7 3D printing outcome

Patient-specific scaffold geometries and precise porosities are essential for optimising biocompatibility and matching complex defects. 3D printing via vat photopolymerization can meet these requirements, enabling the rapid fabrication of porous architectures. In this study, the working curves for each polyHIPE formulation were first determined, relating UV exposure time to cure depth, and used these data to determine the printing settings. The final protocol resulted in 15 s exposure for the first layer (to secure a good adhesion to the build platform), 10 s for the second layer (to reinforce the second layer adhesion), and 3 s per subsequent layer. All layers were cured under a 405 nm light at 19 mW/cm², with a z-axis

resolution of 100 µm and an xy-resolution of 25 µm. As shown in Figure 42, this approach produces high-fidelity, porous polyHIPE scaffolds, accurately reproducing complex designs without the need for additional dyes or photoabsorbers.

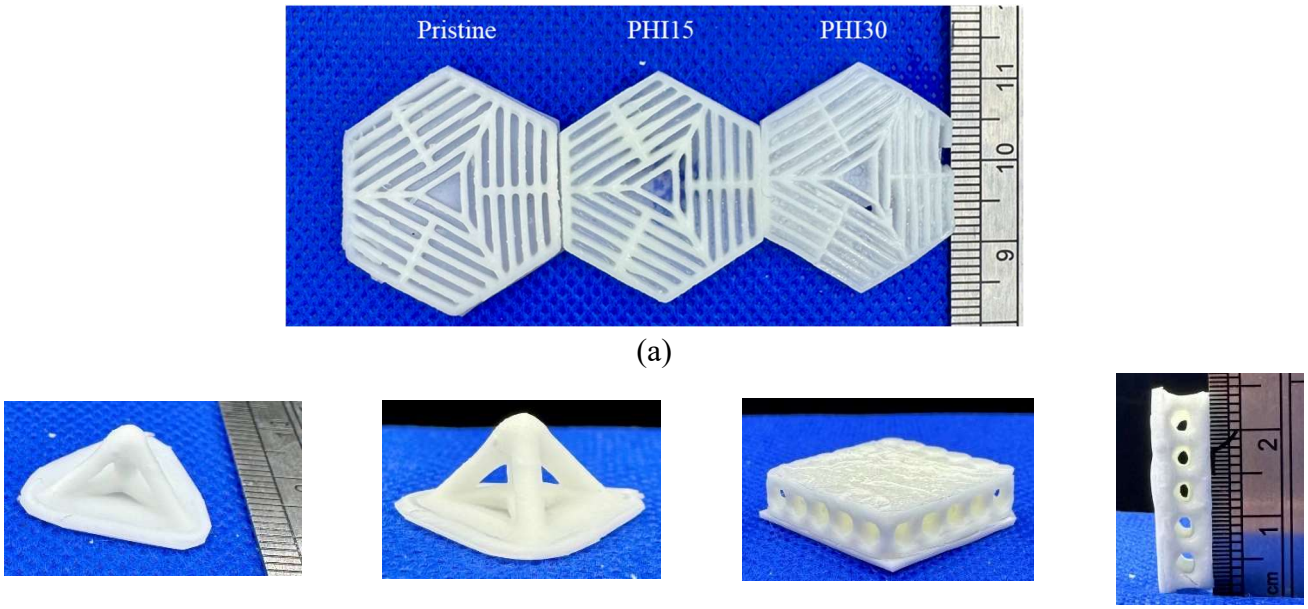

Figure 42. a) Overview of all printed formulations, including pristine and BG-reinforced scaffolds. b–e) 3D printed structures from the pristine formulation, illustrating both hollow geometries and scaffold-like architectures with interconnected porosity.

3.4.8 Biological evaluation

The biological performance of polyHIPE composite scaffolds was evaluated through a series of in vitro assays using MG-63 osteosarcoma cells, a widely accepted model for osteoblastic activity [185]. Discs (6 mm diameter, 0.4 mm thickness) were seeded with 5×10^4 cells in a 100 µL droplet, poured onto the samples and allowed to attach for 60 minutes in the incubator. Following attachment, 2 mL of complete culture medium was added, and samples were maintained under standard conditions (37 °C, 5 % CO_2, high humidity) with medium changes every 2–3 days, or until 80% confluency was reached.

Metabolic Activity (Resazurin Assay)

Cellular metabolic activity was quantified at days 1, 3, and 7 via a resazurin-based assay (Figure 43). All scaffold formulations presented an increase in metabolic conversion over time, indicating cell proliferation over the sample surface. Both BG-reinforced scaffolds (PHI15 and PHI30) exhibited metabolic

activities comparable to the pristine polyHIPE, and all samples exceeded those measured in the control well (NoScaffold), demonstrating that neither the porous architecture nor the bioactive glass content compromised MG-63 viability.

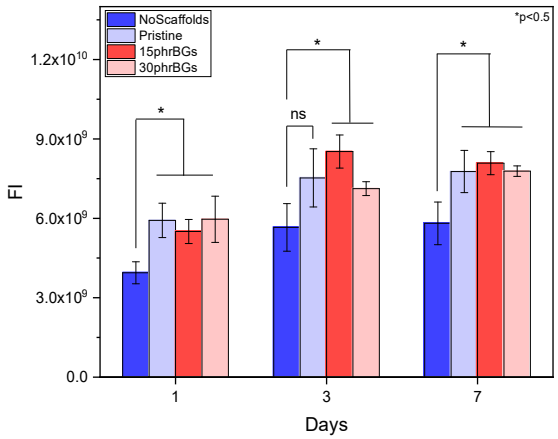

Figure 43. Resazurin assay results obtained for all the polyHIPE formulations and the corresponding reference (NoScaffold).

Cell Morphology and Spreading (Fluorescence Imaging)

Cytoskeletal organisation and nuclei distribution were visualised by dual staining with Phalloidin (for F-actin) and DAPI at days 1, 3, and 7 (Figure 44). By day 1, MG-63 cells showed good adhesion and initial spreading along the scaffold surface, especially on the PHI15 and PHI30 surfaces. Over the following days, the cells began to grow in number and confluency, particularly on PHI15 and PHI30, where elevated cell density and extensive lamellipodia were observed. These findings highlight the favourable properties provided by the interconnected pores and the stimulatory effects of bioactive glass.

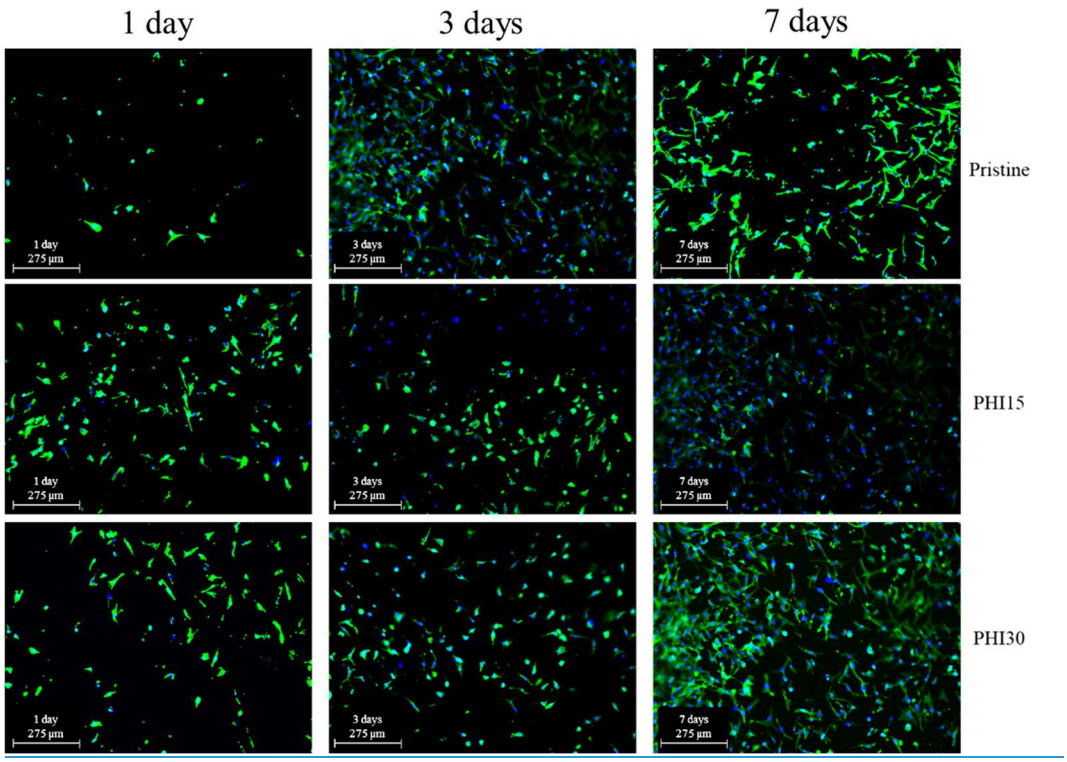

Figure 44. Stained MG63 cells cultured on pristine and polyHIPE reinforced scaffolds after 1, 3, and 7 days of culturing.

Osteogenic Mineralisation (OsteoImage™ Assay)

After 28 days in medium, hydroxyapatite deposition was assessed using a fluorescence-based mineralisation assay (Figure 45). Low HAp presence was detected on the pristine polyHIPE, while PHI15 and PHI30 scaffolds demonstrated progressively stronger hydroxyapatite signals in proportion to bioactive glass content. The dose dependent mineralisation confirms the osteoinductive capacity of the scaffolds, attributed to the sustained release of Ca^{2+} and Si^{4+} ions known to trigger osteogenic pathways and nucleate bone-like mineral formation.

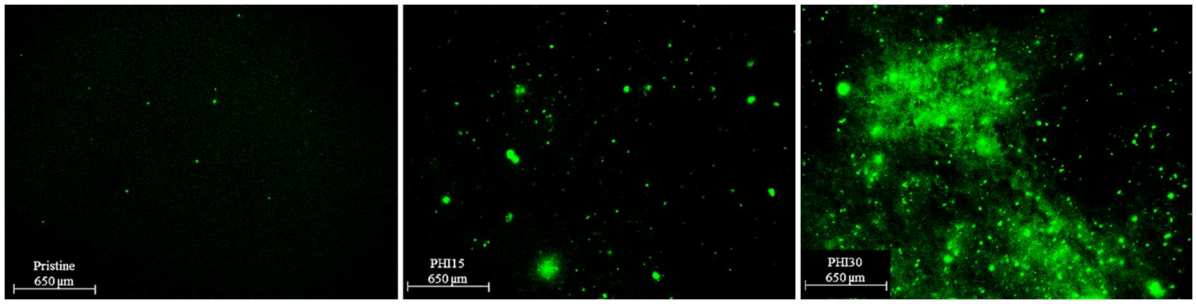

Figure 45. Representative fluorescence microscopy images of polyHIPE scaffolds after 28 days of incubation with MG-63 cells, stained using the OsteoImage™ Mineralisation Assay (left to right: pristine, PHI15 and PHI30 scaffolds).

Together, the biological data indicate that BG-reinforced polyHIPE scaffolds provide an optimal environment for MG-63 attachment, proliferation, and differentiation, giving, after 28 days, a hydroxyapatite forming, essential for bone tissue growth. Their interconnected porosity, biocompatible thiol–ene network, and incorporated bioactive glass make these materials promising candidates for non-load bearing bone regeneration applications.

In conclusion, the biobased thiol–ene polyHIPE scaffolds reinforced with 15 and 30 phr of bioactive glass proved to combine rapid UV cure, high and interconnected open porosity, and enhanced mechanical stiffness in the presence of the glass particle reinforcement, all while retaining the elasticity typical of a sponge like material, which can be exploited during implantation and during solicitations in vivo. MG-63 studies confirmed the excellent cytocompatibility, with BG-loaded scaffolds leading to increased cell proliferation and HAp formation in 28 days. These results establish BG-reinforced polyHIPEs as a sustainable, 3D-printable platform for bone tissue engineering and open the way to move this approach to acrylated soybean oil–based composites with specific ionic functionality.

3.5 Foam to Bulk Transition: Epoxidised Acrylated Soybean Oil for Rigid 3D-Printed Scaffolds

In contrast to the emulsion-templated thiol–ene polyHIPE systems, acrylated epoxidised soybean oil (AESO) can function as the only reactive component in a radical photopolymerisation process. When exposed to UV light, AESO acrylate moieties undergo rapid crosslinking, typically completing in just a few seconds. This fast cure, however, does not allow for high internal-phase emulsions due to the high viscosity and slower reaction rate than thiol-ene systems; instead, it yields a bulk network that is ideally suited for vat photopolymerization techniques. The formulation benefits from simple chemistry and improved control over bulk curing, enabling the fabrication of rigid, mechanically improved scaffolds with adaptable, patient-specific geometries.

Building on the introductory work in which AESO was combined with bioactive glass fillers to produce UV-cured composites [186], and later extended to silanized copper- and tellurium-doped glasses for enhanced interfacial adhesion and ionic functionality [187]. The acrylate-only approach offers an alternative pathway. It bridges the gap between highly porous polyHIPE foams and the need for mechanically robust constructs in applications where porosity must be balanced against structural integrity. Moreover, when the AESO network is filled with bioactive glass, whether undoped, copper-doped, or tellurium-doped, it can potentially retain the biocompatibility, antibacterial potential, and osteoinductive capacity in reprocessable AESO/BG-Te scaffolds [188].

3.5.1 Resin formulation and photocuring

The AESO monomer was used as received and mixed with 2 wt% of the radical photoinitiator phenylbis(2,4,6-trimethylbenzoyl) phosphine oxide, along with varying amounts of both a basic formulation of bioactive glass and the reactive diluent isobornyl acrylate (IBOA). As reported in Table 8, fifteen formulations were prepared. The components were homogenised using an Ultra-Turrax T10 basic mixer until a uniform mixture was obtained. UV curing was then performed either in silicone moulds using a DYMAX ECE flood lamp or via 3D printing with a Prusa SL1S SPEED printer. The cured samples were subsequently post-cured under the DYMAX lamp for 60 seconds.

Table 8. Formulation names based on the AESO:IBOA ratio and BGs quantity.

AESO (%wt)	IBOA (%wt)	BG (phr)	Sample Name
50	50	0	A0
		10	A10
		30	A30
60	40	0	B0
		10	B10
		30	B30
70	30	0	C0
		10	C10
		30	C30
80	20	0	D0
		10	D10
		30	D30
100	0	0	E0
		10	E10
		30	E30

3.5.2 Photocuring process evaluation

Acrylate double-bond conversion was monitored by transmission-FTIR through the decrease of the peak at 1620 cm^{-1} under UV irradiation. Figure 46 compares conversion vs. time for the pristine formulation (C0) and the same resin containing increasing amounts of bioactive glass. As the printable formulation for subsequent studies, the C0 formulation is shown here; complete ATR-FTIR data for all the other formulations are provided in Table 9. All AESO: IBOA mixtures achieved satisfactory final conversions (>65 %), with a slight increase in conversion observed with the increase in IBOA content, likely due to delayed vitrification at lower crosslink density. Incorporation of up to 30 phr BG produced a modest decrease in conversion, attributable to competitive UV absorption by the glass particles, but did not significantly affect the final result.

To validate the FTIR results, the exothermic heat release during UV curing was measured using photo-DSC (Table 9). The pristine formulations showed a small exotherm increase with higher IBOA content, reflecting the ATR-FTIR trends. Adding BG reduced the integrated exothermic peak slightly, consistent with the marginal conversion drop. However, the overall heat release remained satisfactory, indicating that BG loadings up to 30 wt % do not compromise the overall photocuring reaction.

Photo-rheology experiments (Figure 46 c,d) tracked the evolution of the storage modulus G′ under 365 nm irradiation. All formulations reached a G′ plateau within

20 s, with a gel point at 5 s. This uniform behaviour confirms that neither diluent nor filler significantly affects network formation kinetics.

Table 9. FTIR and photoDSC values obtained for all formulations.

Sample Name	Conversion after 120 s Irradiation from FTIR measurements	Heat released from photoDSC measurements [J/g]
A0	82 ± 5	459 ± 11
A10	76 ± 2	418 ± 4
A30	75 ± 5	338 ± 5
B0	80 ± 8	437 ± 10
B10	72 ± 2	351 ± 5
B30	66 ± 3	342 ± 7
C0	86 ± 8	419 ± 7
C10	74 ± 2	350 ± 10
C30	73 ± 14	315 ± 2
D0	77 ± 2	389 ± 11
D10	74 ± 4	316 ± 13
D30	65 ± 14	275 ± 5

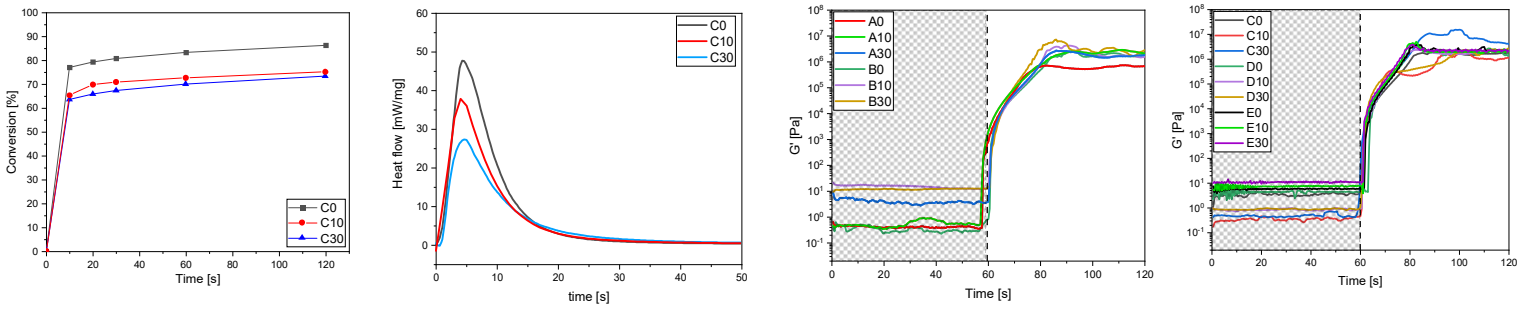

(a) (b) (c) (d)

Figure 46. Photocuring analysis performed on the AESO-BG formulations. a) represent a typical behaviour of transmission FTIR, b) represent a typical photoDSC measurement. c) and d) shows all the analysis performed on the samples during the photorheology, where UV light was switched on after 60 s the starting of the test.

3.5.3 Thermal and mechanical properties of cured AESO-BG samples

DMTA was employed to determine the glass transition temperature of UV-cured AESO based materials (Table 10). In the pristine formulations, T_g increases slightly with higher IBOA content. Ordinarily, adding a monofunctional diluent would lower T_g, but here the rigid bicyclic structure of isobornyl acrylate dominates, stiffening the network and raising T_g

Introducing up to 30 phr of BG into the biobased matrix produces a modest T_g reduction, consistent with the slight cure inhibition observed by FTIR and photo-DSC, caused by the competitive UV absorption by the glass.

Interestingly, 3D-printed samples exhibit the opposite trend: T_g rises as BG loading increases. The main reason behind this effect is that mSLA 3D printing cures each 50 µm layer individually, avoiding the light attenuation that affects thick moulds. These reflect stronger BG polymer interactions than in bulk-cured specimens.

Table 10. Glass transition temperature of mold cured and 3D printed samples.

Sample Name	Glass Transition Temperature T_g [°C]
A0	75 ± 1
A10	74 ± 0
A30	73 ± 0
B0	73 ± 2
B10	72 ± 0
B30	68 ± 3
C0 (3D printed)	67 ± 2 (60 ± 0)
C10 (3D printed)	66 ± 3 (64 ± 4)
C30 (3D printed)	60 ± 0 (72 ± 2)
D0	61 ± 0
D10	62 ± 3
D30	60 ± 2

Compression testing on both mould-cured and printed samples performed on C0, C10, and C30 reveals a general decrease in modulus with increasing BG content (Table 11, Figure 47). In mould-cured samples, this drop follows the lower T_g and conversion at higher filler loadings. However, 3D-printed samples show substantially higher modules than their mould-cured counterparts, proving the mechanical advantage conferred by layer-by-layer curing. Moreover, although modulus still falls from C0 to C10, it partially recovers in C30, suggesting that above 30 phr the reinforcing effect of the well-dispersed glass phase begins to overcome the cure inhibition effect, resulting in a compressive resistance increase.

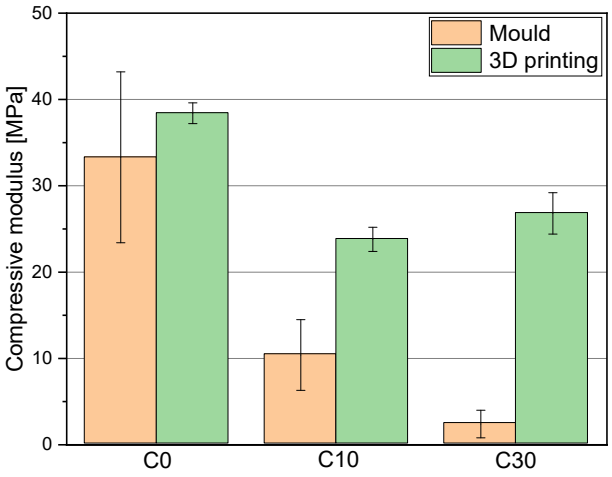

Figure 47. Compression tests performed across all AESO based formulations.

Table 11. Compressive elastic modulus obtained from mechanical tests.

	Compression Modulus [MPa]		
AESO-IBOA sample	Pristine	10 phr BG	30 phr BG
C (mould)	33.3 ± 9.9	10.4 ± 4.1	2.4 ± 1.6
C (3D printed)	38.4 ± 1.2	23.8 ± 1.4	26.8 ± 2.4

3.5.4 Rheology and 3D printing

Rheological measurements were performed to assess the viscosity and flow behaviour of each formulation. Figure 48a presents viscosity versus shear rate for all samples, while Figure 48b compares the viscosity of the AESO-only formulation (E) as a reference. The viscosities measured at 30 s^{-1}, correspond to a shear rate representative of 3D-printing conditions [189–195]. Consistent with literature reference for vat photopolymerization, the C30 formulation (70:30 AESO:IBOA with 30 phr BG) exhibited the most favourable viscosity profile and was therefore selected for subsequent printing trials.

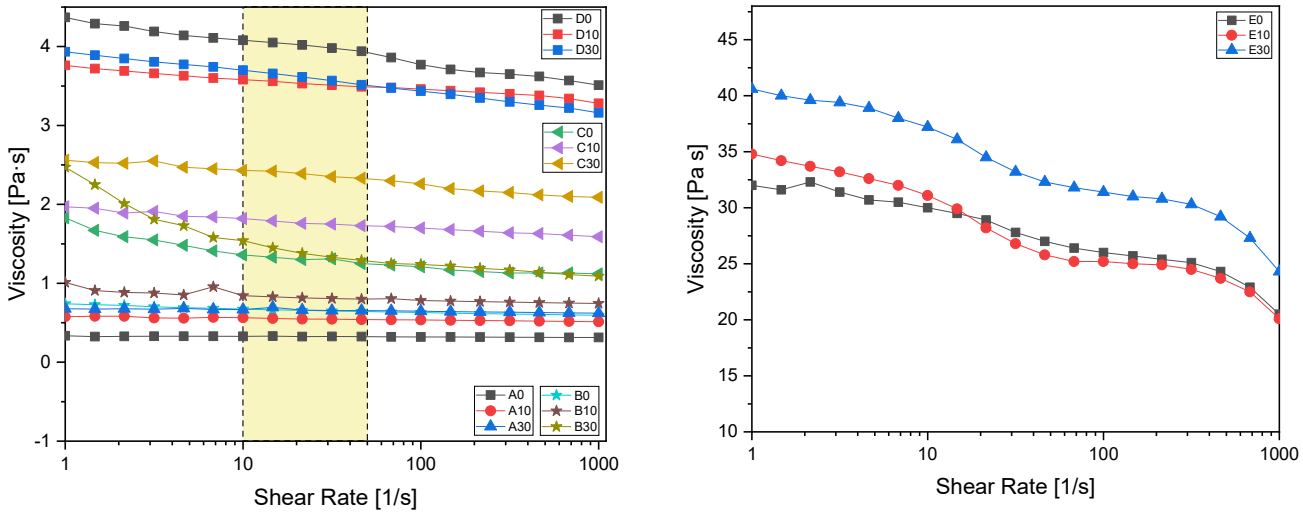

(a) (b)

Figure 48. a) Viscosity parameters measured from 1 to 1000 shear rate [1/s]. Tthe shear rates typical of a 3D printing process are evidenced in yellow; (b) viscosity reference of AESO samples without reactive diluent. All the values were measured with a 2.5 mm diameter plate.

Using a PRUSA SL1S printer (Prague, Czech Republic), the pristine resin (C0) and its BG-reinforced variants (C10 and C30) were successfully manufactured into layer-by-layer structures (50 µm layer thickness) under 405 nm irradiation for 2.5 s per layer. Printed parts were rinsed in isopropanol and sonicated for 5 minutes to remove unreacted resin, then post-cured under a DYMAX lamp for 1 minute to ensure complete crosslinking. Various geometries, including specimens for DMTA and compression, were produced. Figure 49 illustrates a complex, highly porous scaffold printed from C30, with pore sizes of approximately 1 mm.

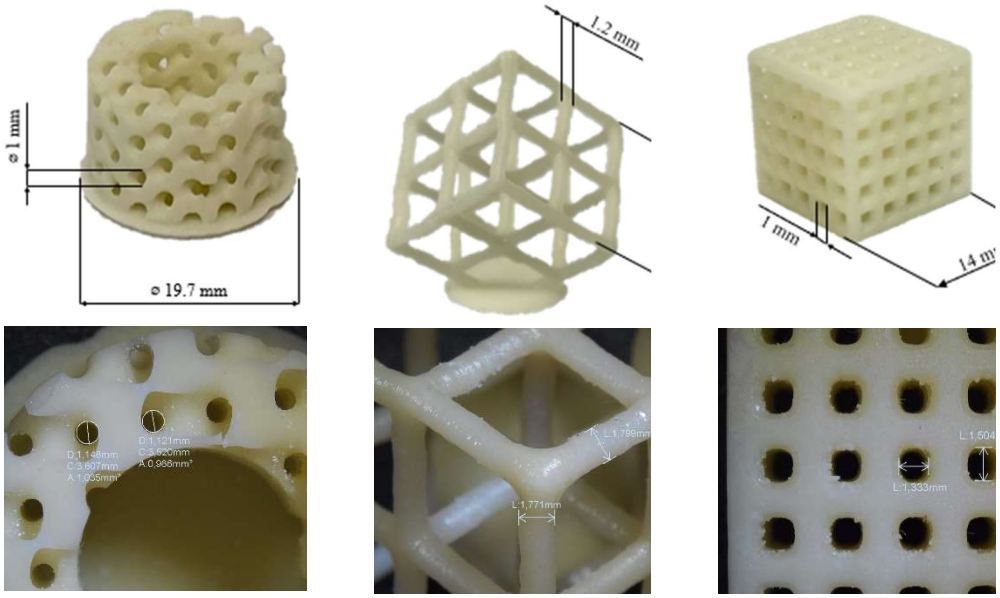

(**a**) (**b**) (**c**)

Figure 49. 3D printed structures obtained by means of Prusa SL1S. All structures represent C30 formulation.

Fracture-surface SEM of printed C10 and C30 samples (Figure 50a) revealed a uniform dispersion of BG particles throughout the polymer matrix, with minimal aggregation. High-magnification imaging (Figure 50 a,b) confirmed the effective filler dispersion during the printing and curing process.

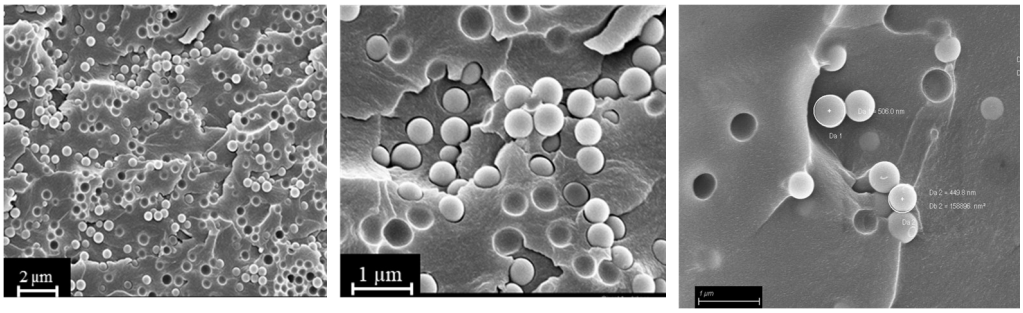

(a) (b) (c)

Figure 50. (a) Sample C30 at 1000× magnification; (b) sample C10 at 30,000× magnification; (c) sample C30 at 30,000× magnification.

3.5.5 Cytocompatibility evaluation

The AESO:IBOA (70:30) formulation containing 30 phr BG (C30) emerged as the most promising candidate for 3D printing based on its rheological profile and crosslink density. To assess cytocompatibility, human bone-marrow mesenchymal stem cells (hMSCs), chosen for their self-renewal and differentiation capacity [196], were seeded directly onto the surfaces of C30, C10 (70:30 + 10 phr BG), C0 (70:30 + 0 phr BG), A0 (50:50 + 0 phr BG), and E0 (100 % AESO, no IBOA or BG). After 24 h and 48 h, metabolic activity was quantified by resazurin assay and cell morphology by SEM and live/dead fluorescence (Figure 51a,b) .

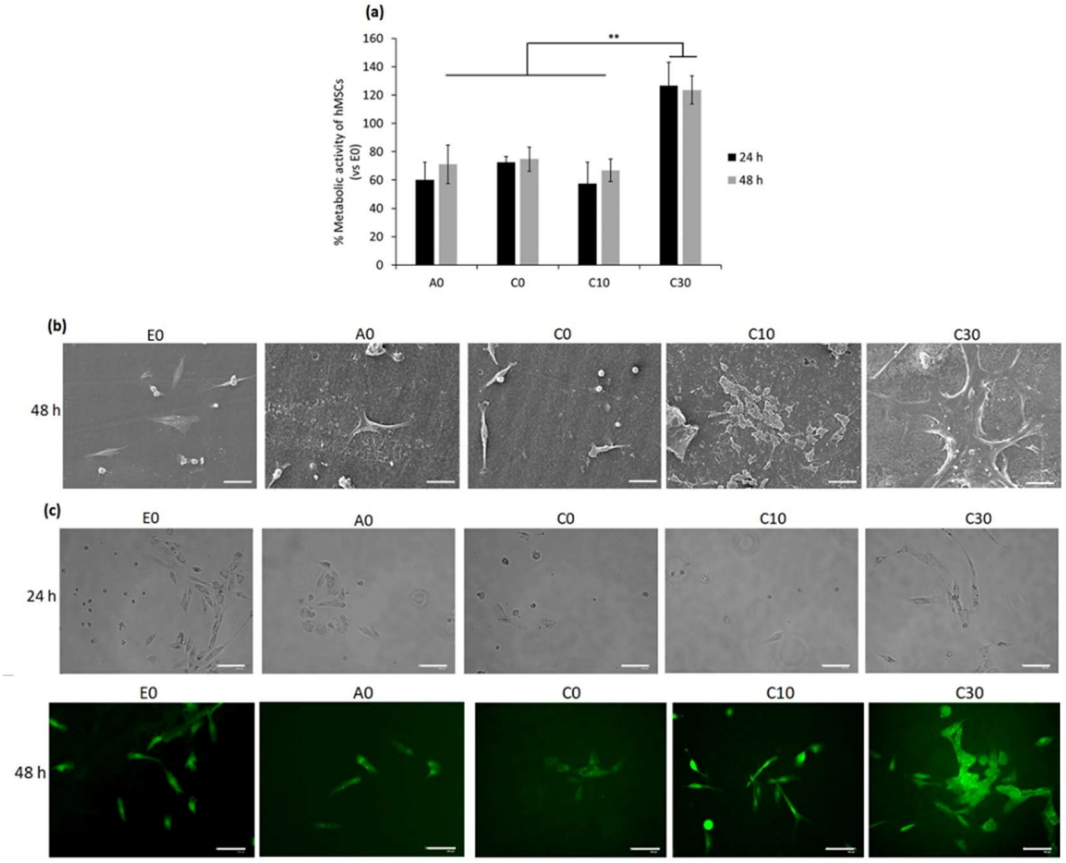

Figure 51. a) represent the Resazurin assay performed on the scaffolds formulations after 24 and 48 hours. b) and c) shows the cells SEM images, while the bottom layer reports the live/dead fluorescence.

At 24 h, relative fluorescence units (RFU) normalized to E0 indicated that hMSCs on A0, C0, and C10 exhibited reduced metabolic activity, respectively, while C30 supported activity comparable to the control. After 48 h, C30 showed significantly higher metabolic activity than A0, C0, C10, and E0 ($p < 0.01$) (Figure 51a). SEM micrographs at 48 h confirmed extensive cell spreading on C30, while fewer, more rounded cells were observed on the other formulations (Figure 51b). Live/dead staining further demonstrated a predominance of live cells, showed with the green colour on C30 compared with A0, C0, C10, and E0

To determine whether non-adherent (floating) cells remained viable, the culture medium was transferred at 24 h to fresh wells. After reseeding, floating cells from C30 adhered and proliferated, with few dead cells detected, whereas wells seeded with floating cells from A0, C0, C10, and E0 showed a larger proportion of non-viable cells (Figure 51c).

These data confirm that the C30 formulation not only possesses the flow and curing characteristics required for high-resolution 3D printing but also provides a surface favourable to hMSC attachment, viability, and proliferation. The enhanced performance of BG-reinforced formulations likely derives from the ion-release profile of bioactive glass, alkalinising the local environment and supplying Ca^{2+} and Na^{+}, which promote cell adhesion and osteogenic signalling [197–199].

3.6 Mechanical properties enhancement and bioactive glass doping. A step forward to increase functionality

Having established the beneficial properties of using bioactive glass (BG) as a reinforcement phase for hard tissue scaffolds, which combine mechanical performance with enhanced biological interactions and 3D printability, we then aimed to further improve the functionality of the composite. In particular, the previously tested formulations showed good cytocompatibility with human bone marrow mesenchymal stem cells (hMSCs), a reliable model for bone-related applications. However, FESEM analysis revealed that although the BG particles were well dispersed within the polymeric matrix, the interface between the glass and resin was not optimal, as evidenced by voids around the particles. These voids indicate poor wettability of the BG by the resin, leading to weak interfacial adhesion and limiting mechanical reinforcement (Figure 50).

To address this issue and achieve better integration between the filler and matrix, we silanised the BG particles. The silanisation process introduced aliphatic functional groups on the glass surface, promoting better interfacial bonding with the polymer matrix and enabling tuning of the mechanical properties depending on application needs. In parallel, we wanted to further enhance the biological functionality of the scaffold. For this reason, we incorporated copper doping into the BG structure. Copper ions are known to provide antimicrobial activity while also supporting angiogenesis and bone tissue repair. The resulting silanised, Cu-doped BG offers a dual role within the 3D-printed scaffold: improved mechanical performance due to enhanced matrix-filler interactions, and antibacterial effect via Cu ion release, supporting both antibacterial defence and osteogenic stimulation.

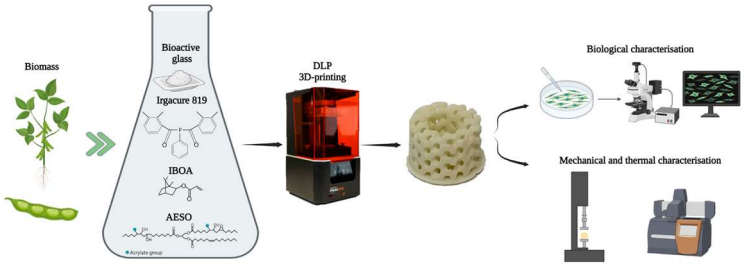

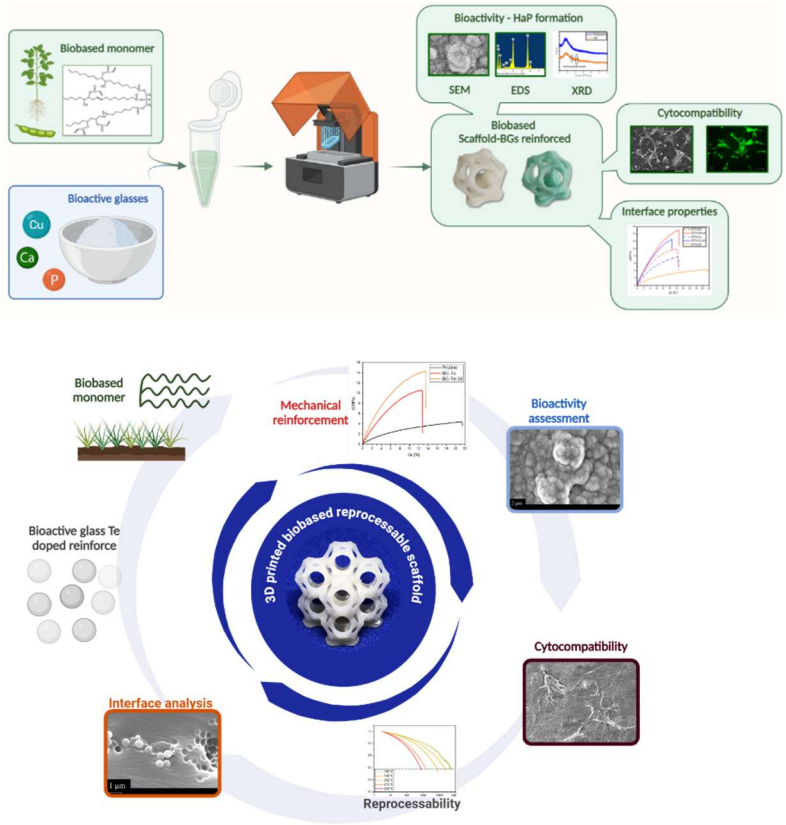

Figure 52. Project scheme related to the 3D printing of biobased scaffold reinforced with Cu-doped and silanised bioactive glass (Cu-Sil).

3.6.1 Resin composition

Following the previous study, the bio-based photocurable resin was prepared by mixing acrylated epoxidised soybean oil (AESO) with 2 wt% of the radical photoinitiator Irgacure 819 and 30 wt% of the bio-derived reactive diluent IBOA. Subsequently, 30 parts per hundred resin (phr) of bioactive glass (BG) were incorporated into the mixture.

The four components, AESO, reactive diluent, bioactive glass, and photoinitiator, were initially mixed using an Ultra-Turrax T 10 basic homogeniser to ensure uniform dispersion. To further enhance homogeneity and eliminate entrapped air, the mixture was processed using an ARE-310 Thinky mixer (Thinky Corporation, Laguna Hills, USA) following a mixing cycle composed of 3 minutes of mixing and 3 minutes of defoaming, repeated three times.

A total of nine formulations were prepared, with their compositions summarised in Table 12. All formulations were stored in a dark environment to prevent premature polymerisation due to ambient light exposure. Following storage, the resins were 3D printed using a Prusa SL1S SPEED printer and post-cured under a DYMAX ECE Flood lamp at an intensity of 130 mW/cm² for 60 seconds.

Table 12. Sample names attributed to the formulations in function of the glass doping and type.

AESO (%wt)	IBOA (%wt)	BGs (phr)	BGs type	Name
70	30	30	S4	AI
			Cu-S4	AI-Cu
			Silanised S4	AI-Sil 2h
				AI-Sil 2h pH 5
				AI-Sil 24h
			Silanised Cu-S4	AI-Cu-Sil 2h
				AI-Cu-Sil pH 5
				AI-Cu-Sil 24h
		0	-	AIref

3.6.2 Silanisation of bioactive glasses

After activating the bioactive glass surface with acetone, both the basic formulation (BGref) and Cu-doped glass compositions were immersed in a 20% (v/v) solution of 3-(trimethoxysilyl)propyl methacrylate (TMSPMA) in ethanol. TMSPMA was selected as the silanising agent based on previous studies, particularly those by Nguyen et al., which demonstrated its efficacy in enhancing particle dispersion within polymeric matrices by reducing particle agglomeration. This improved dispersion translates to superior mechanical properties in the resulting composites [200,201]. In addition, TMSPMA offers practical and

environmental advantages, as it can be used in ethanol rather than more hazardous solvents such as xylene.

The silanization mechanism proceeds through hydrolysis and condensation of the trimethoxysilane groups in TMSPMA. Upon hydrolysis, the methoxy groups (-OCH_3) are converted to silanol groups (-SiOH), which then react with hydroxyl groups on the surface of the glass particles. This reaction forms stable Si–O–Si covalent bonds that graft the silane to the glass surface. Furthermore, the remaining methacrylate group of TMSPMA remains available to participate in the photocuring process, allowing for the chemical integration of the functionalized particles into the polymeric network. This dual functionality makes TMSPMA highly effective in enhancing filler-matrix interfacial bonding and uniform dispersion within the matrix.

To identify the optimal silanisation conditions, three methods were tested: (i) 2 h magnetic stirring at room temperature, (ii) 2 h stirring with pH adjusted to 5 using acetic acid, and (iii) 24 h stirring without pH adjustment. The effectiveness of these treatments was assessed using ATR-FTIR and contact angle measurements, as shown in Figure 53 and 54.

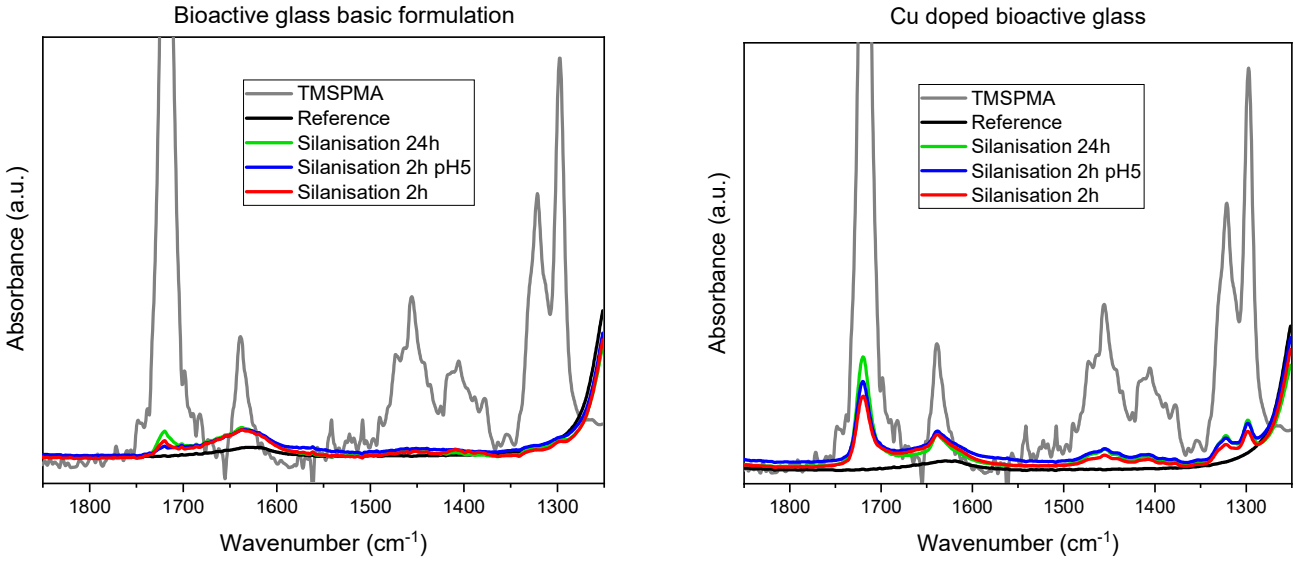

a) b)

Figure 53. a) FTIR spectra of silanised BG basic formulation (BGref). b)FTIR spectra of silanised BG Cu doped.

ATR-FTIR spectra confirmed the presence of TMSPMA functional groups on the surfaces of both silanised BGref and Cu-doped BGs, indicating successful surface modification across all tested methods. Although ATR-FTIR is qualitative, the presence of characteristic peaks corresponding to the silane and the absence of

major differences among the methods suggested comparable efficacy in grafting the silane.

Contact angle measurements provided complementary data on the surface properties. BGref were highly hydrophilic, absorbing water droplets immediately. In contrast, all silanized samples exhibited increased hydrophobicity, confirming the successful grafting of hydrophobic chains onto the BG surfaces. Among the methods tested, the 2 h treatment without pH adjustment generated the lowest hydrophobicity, particularly for BGref. Conversely, both the 2 h at pH 5 and the 24 h treatments resulted in significantly higher contact angles, indicating more effective surface modification, as shown in Figure 54.

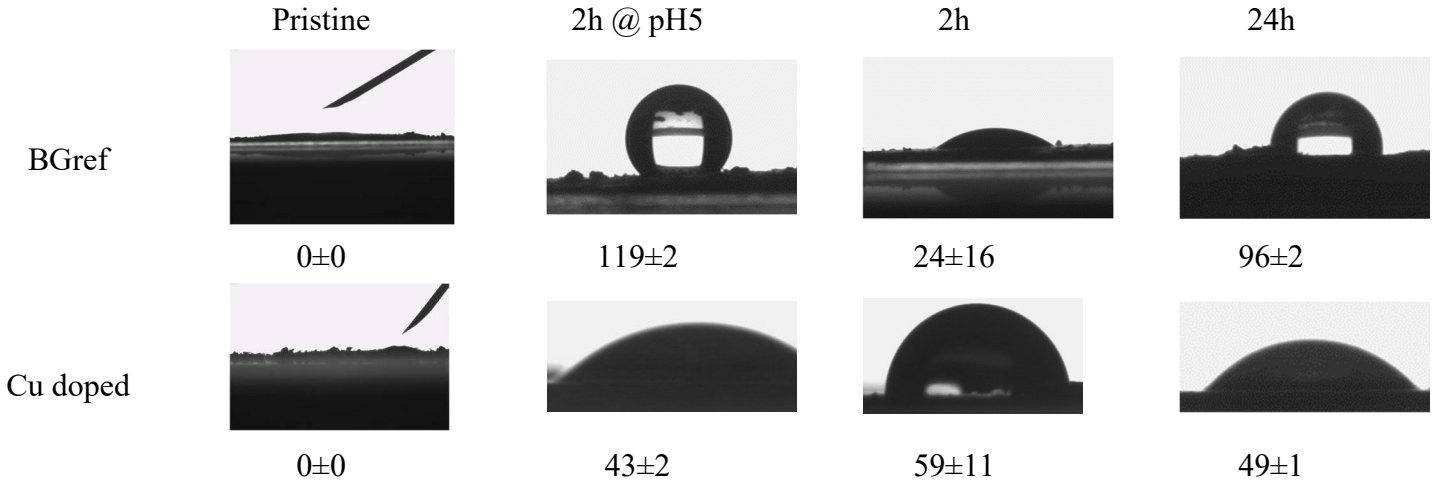

Figure 54. Contact angle measurement across all formulation, silanised and pristine.

Based on these observations, the 2 h at pH 5 and 24 h methods were selected as the most efficient. Ultimately, the 24 h method was chosen for all subsequent work, aligning with the project objective on low-impact and sustainable processing by avoiding additional chemicals like acetic acid.

However, for Cu-doped glasses, there was a potential concern regarding copper ion leaching during prolonged immersion. To address this, EDS analysis was performed post-silanisation to quantify the residual copper content. The Cu weight percentage remained consistent (4.1 wt%) for the 2 h and 2 h at pH 5 methods, and only slightly decreased (3.9 wt%) after 24 h treatment. This minor variation indicates that the 24 h method does not cause significant Cu loss and can be applied to Cu-doped BGs without compromising the copper doping.

Consequently, all bioactive glass powders incorporated into the resin composites were silanized using the 24 h method, ensuring improved matrix-filler interaction and preserving the functional properties of both BGref and Cu-doped formulations.

3.6.3 Photocuring Process

The behaviour of the bio-based photocurable resin under UV irradiation, in the presence of various bioactive glasses (BGs), was evaluated using three complementary techniques: transmission FTIR, photo-DSC, and photorheology. The BG content was fixed at 30 phr in all formulations, as established in the previous studies [186].

3.6.3.1 Transmission FTIR Analysis

Transmission Fourier-transform infrared (FTIR) spectroscopy was employed to assess the conversion of acrylate double bonds upon UV exposure by monitoring the characteristic peak decrease around 1620 cm^{-1}. Representative spectra collected during UV irradiation are shown in Figure 55 and reflect a typical trend across all tested formulations.

As previously observed, the presence of BGs led to a reduced final conversion of the acrylate double bonds. However, the slope of the conversion curves remained similar across formulations, indicating comparable reaction kinetics during the irradiation phase.

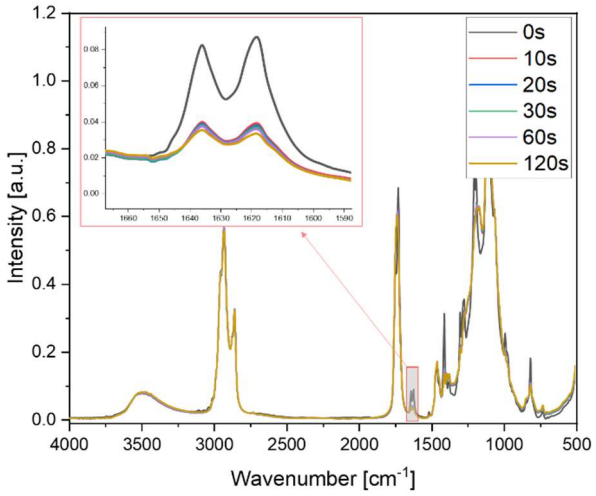

a) **b)**

Figure 55. a) Conversion curves as a function of irradiation time for the formulation A7I3 (from ATR-FTIR) as a function of time varying the different bio-glass at 30 phr content. Light intensity was set at 130 W/cm^2. b) Representative FTIR graph reproduced in all the formulations and magnification of the acrylate peak decrease.

The decrease in conversion related to the BG containing samples is attributed to the physical nature of the glass fillers, which can attenuate light transmission and

potentially compete with the photoinitiator for light absorption. The reduced light penetration and competitive light absorption hinder the formation of reactive species, lowering the efficiency of photopolymerization. Silanized BGs caused a further, although modest, reduction in final conversion. However, all values remained within the acceptable range for effective curing.

3.6.3.2 Photo-DSC Analysis

To validate the FTIR results, photo-differential scanning calorimetry (photo-DSC) was conducted. The exothermic profiles of all tested formulations are shown in Figure 56 and detailed in Table 13. The photo-DSC data validated the FTIR results, showing that the inclusion of BGs slightly diminished the total heat released during UV curing. This is consistent with the reduced double bond conversion observed. Additionally, the presence of silanised fillers led to a further decrease in exothermic response, consistent with their impact on conversion efficiency.

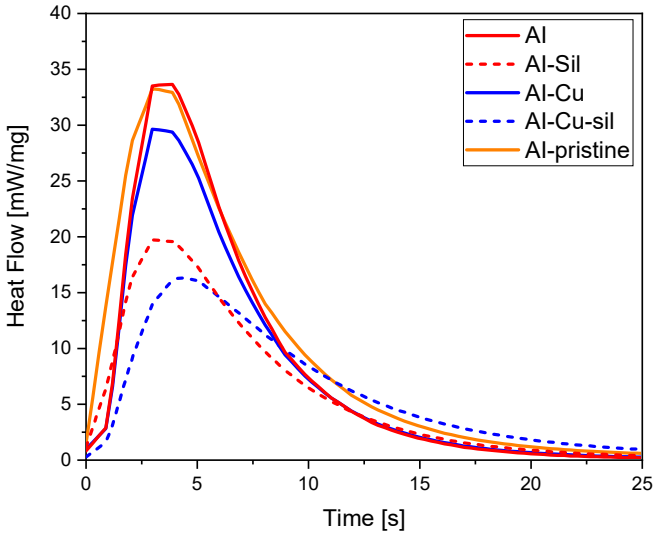

Figure 56. photoDSC measurements across all formulations.

Table 13. Heat released by photopolymerisation measured by means of photoDSC.

Sample	Integral [J/g]
AI-pristine	256 ± 33
AI	215 ± 16
AI-Sil	144 ± 25

AI-Cu	203 ± 10
AI-Cu-Sil	156 ± 5

3.6.3.3 Photorheological and Viscosity Analysis

Photoreology was performed to assess the curing kinetics and determine optimal parameters for 3D printing. The evolution of the storage modulus (G′) upon UV irradiation is shown in Figure 57a. All formulations demonstrated a rapid increase in G′, reaching a plateau within seconds, indicating the formation of a crosslinked network. Importantly, the gelation time was consistent across all formulations, approximately 5 seconds, regardless of the type of BG used. These results confirm that the silanisation of BGs does not affect the photocuring kinetics.

To evaluate printability, viscosity measurements were performed. The flow curves, shown in Figure 57b, indicate shear-thinning behaviour suitable for 3D printing. All formulations exhibited viscosities below 5 Pa·s at a shear rate of 30 s^{-1}, in accordance with the requirements for 3D printing processes reported in the literature [189,191–195,202].

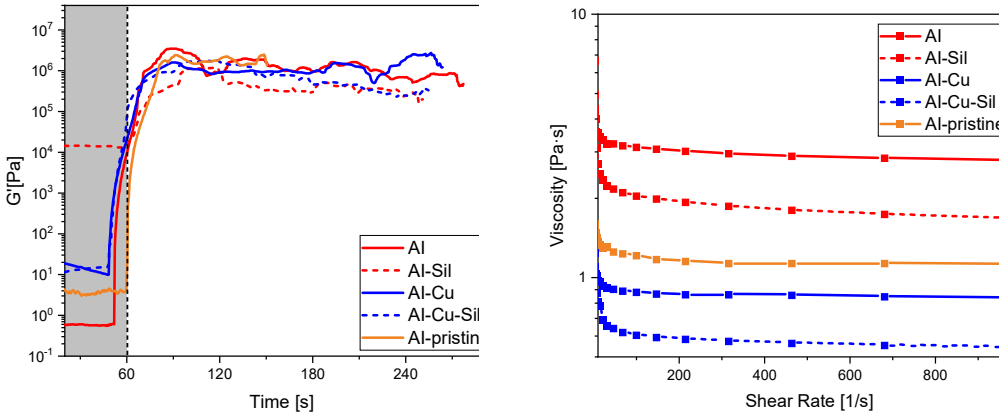

a) **b)**

Figure 57. a) Photo-rheology results of all formulations. UV-light irradiation started after 60 s. b) Rheology curves obtained for all the biobased formulations reinforced with BGs.

3.6.4 The 3D printing process

All previously characterised formulations were 3D printed using a Prusa SL1S SPEED printer via mSLA. The mSLA technique was specifically selected for its ability to produce high-resolution parts with smooth surfaces and by maintaining a uniform distribution of bioactive glass particles within the polymer matrix.

Moreover, the technique facilitates the fabrication of structures with controlled porosity, which is particularly advantageous for applications requiring bioactivity and cellular interaction.

A variety of geometries were successfully printed, including specimens for dynamic mechanical thermal analysis (DMTA), dog-bone-shaped samples for tensile testing, and square-shaped samples for compression testing. Additionally, as shown in Figure 58, more complex and hollow architectures were also fabricated, confirming the versatility of the 3D printing process. These results align with the previous studies, demonstrating the capability of this approach to fabricate complex designed structures with personalised shape and porosity for biomedical applications.

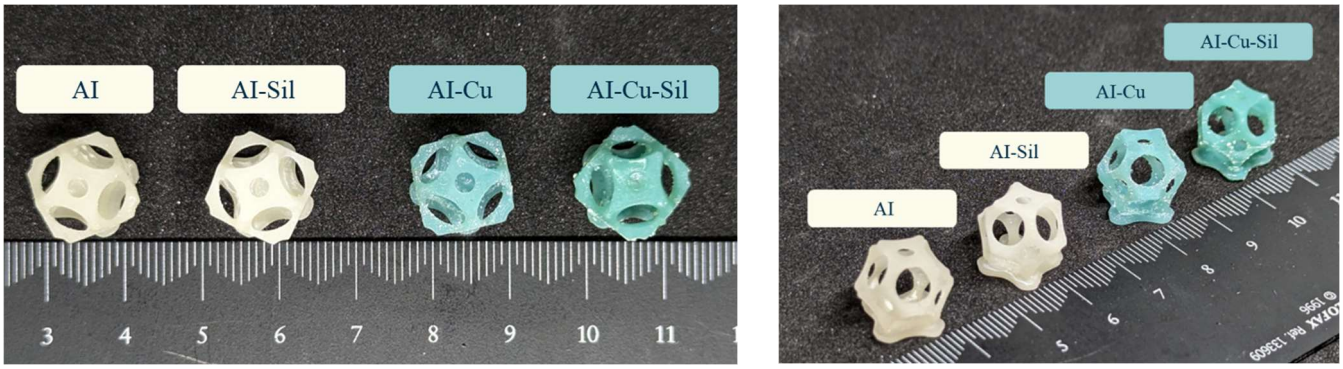

(a) (b)

Figure 58. 3D printed biobased BGs reinforced scaffolds from different points of view. The blue colour is given by the Cu doping. (a) top view, (b) side view.

3.6.5 Scaffold characterisation

Scanning Electron Microscopy (SEM) was conducted on the fracture surfaces of selected 3D-printed scaffolds to evaluate the dispersion of bioactive glass (BG) particles and the interfacial quality between the filler and the matrix. Figure 59a and 59b present SEM images of samples reinforced with BGs, both pristine and silanised, while Figures 59c and 59d show the corresponding images for scaffolds incorporating Cu-doped BGs.

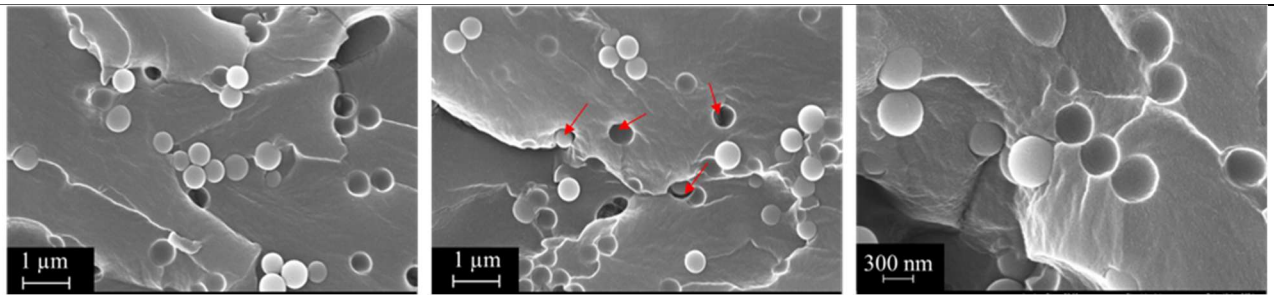

a)

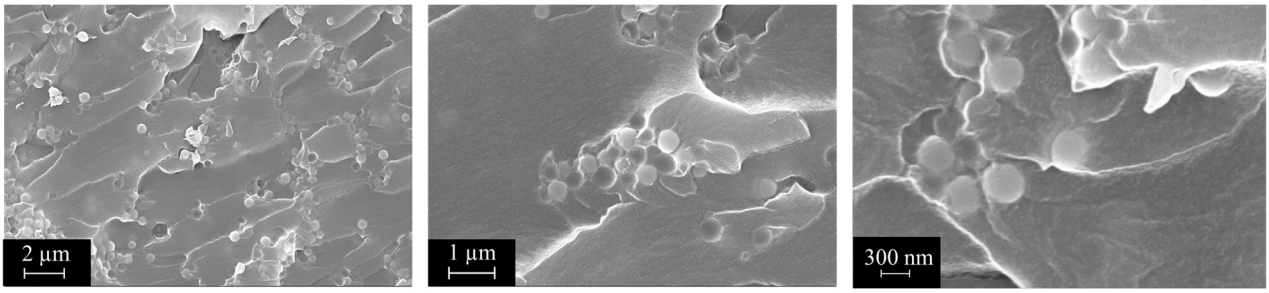

b)

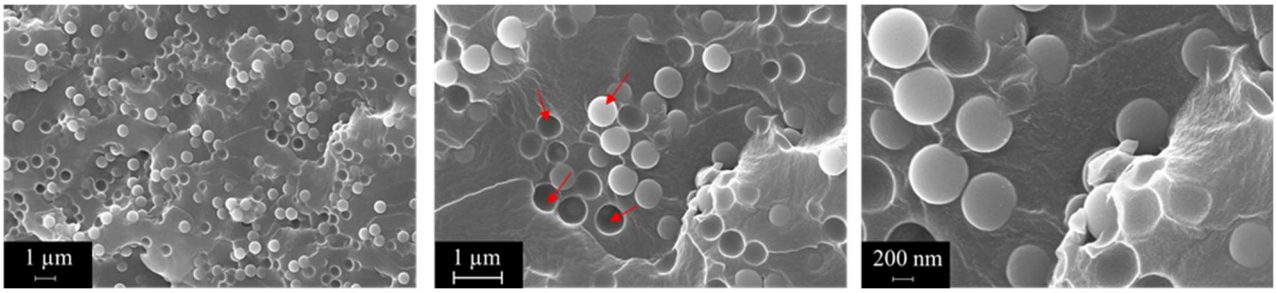

c)

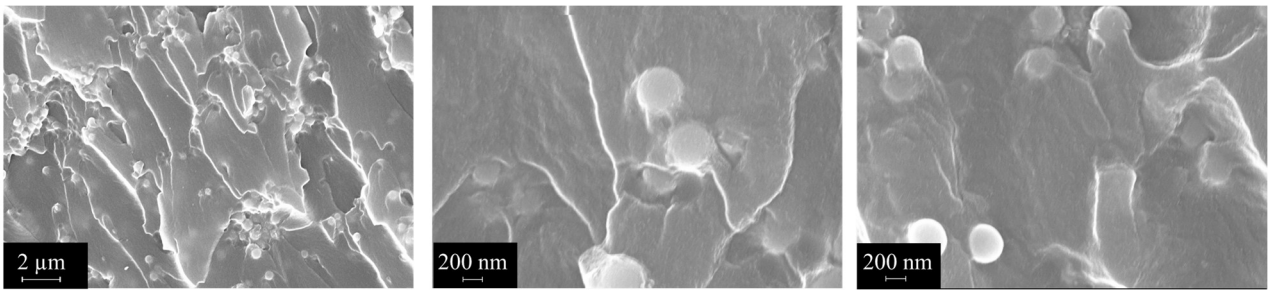

d)

Figure 59. a) a. A7I3-S4 sample surface fracture. b)A7I3-S4-sil sample surface fracture. c) A7I3-Cu sample surface fracture d) A7I3-Cu-sil sample surface fracture

All samples exhibited a uniform dispersion of BG particles throughout the polymer matrix, indicating the successful mixing protocol. Notably, comparison between silanized and non-silanized BG-containing composites reveals a substantial enhancement in interfacial adhesion in the presence of silanized glass. In non-silanized samples, visible voids around BG particles and corresponding holes left by the removal of the filler (red arrows) suggest poor matrix-filler

interaction, leading to interfacial debonding upon fracture, indicative of a weak interface.

In contrast, samples with silanized BGs exhibit no interfacial voids, indicating that fracture occurs within the polymer matrix rather than at the filler-matrix interface. This observation suggests the formation of a strong interfacial bond, likely due to the chemical linkage between the silane-modified glass surface and the acrylated matrix.

Interestingly, the SEM images of samples with silanized BGs appeared less defined compared to their non-silanized counterparts. This is attributed to the polymeric coating surrounding the BGs resulting from the stronger interfacial bonding. Since the polymeric phase has lower electrical conductivity than glass, this coating reduces electron emission, thereby diminishing image contrast under SEM and confirming, once more, the effective integration of reinforcement.

The average particle sizes of BGs embedded in the matrix were consistent with our previous findings. The BG particles exhibited a mean diameter of 482 ± 59 nm, while the Cu-doped BGs showed a slightly smaller mean diameter of 412 ± 67 nm.

3.6.6 Thermomechanical properties

DMTA was performed to assess the viscoelastic behaviour of the photocured AESO-based composites. The results, reported in Figure 60a and Table 14, highlight the influence of BG type and silanization on the glass transition temperature (T_g).

No significant variation in T_g was observed between scaffolds filled with silanized and non-silanized glasses. However, a slight decrease in T_g was observed in Cu-doped glass formulations. This may be attributed to the UV-light absorption characteristics of Cu, which imparts a blue colour to the material. The increased UV absorption may potentially interfere with the photopolymerization process, thereby reducing the overall degree of crosslinking. This hypothesis is supported by a lower conversion rate, as determined by FTIR and photo-DSC analyses.

Tensile tests were conducted on the 3D-printed scaffolds to investigate the impact of BG incorporation and silanization on mechanical performance. The results (Figure 60b and Table 14) show that the inclusion of BGs enhances overall mechanical properties, while silanization provides a further, substantial improvement.

In particular, the elastic modulus increased by ~70% in the silanized AI samples and by 40% in the silanized Cu-containing scaffolds compared to their non-silanized analogues. Similarly, the stress at break improved by 35% in both systems.

The strain at break remained largely unchanged, indicating that the composites retained their ductility.

These improvements confirm the critical role of silane coupling agents in promoting strong interfacial bonding between the polymer and the inorganic phase. The presence of aliphatic chains on the silanized glass surface likely promotes chemical bonding with the acrylated matrix, resulting in enhanced load transfer and mechanical performance.

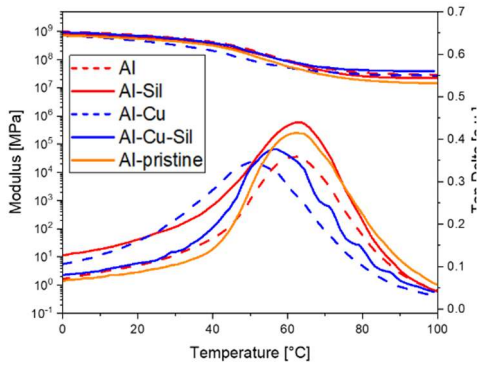

(a) (b)

Figure 60. Thermomechanical graph obtained across all formulations. (a) represents the DMTA analysis, while (b) represents the tensile tests. The dotted lines correspond to the composites containing silanised bioactive glasses.

Table 14. Glass transition temperature and mechanical data obtained from DMTA and tensile tests.

Sample	Glass transition temperature T_g [°C]	Elastic modulus [MPa]	Stress at break [MPa]	Strain at break [%]
AI-pristine	60±0	0.49±0.15	4.86±0.82	28.37±5.28
AI	61±2	0.59±0.04	9.93±0.61	12.55±0.36
AI-Sil	60±2	1.87±0.08	15.25±0.41	13.22±0.59
AI-Cu	56±0	1.17±0.21	8.20±2.49	14.88±3.56
AI-Cu-Sil	50±1	1.85±0.15	12.86±1.84	11.07±0.74

3.6.7 In vitro bioactivity test

Evaluating the scaffold response after immersion in simulated body fluid (SBF) is crucial to determine its ability to promote hydroxyapatite (HAp) formation, the precursor phase of mineralised bone.

In vitro bioactivity assessment is commonly used to predict in vivo behaviour and thus to estimate the ability of materials to bind to bone tissue. To assess its growth, AI-Cu scaffolds were immersed in SBF at 37 °C for 28 days. Cu-doped formulations were specifically chosen due to the possible inhibitory effect of copper ions on HAp formation [203].

FESEM images performed on the sample surface (Figure 61a–c) reveal the presence of early-stage HAp crystal nucleation by day 7, and well-developed HAp lamellae by day 28. Energy-dispersive spectroscopy (EDS) confirmed a Ca/P ratio of 1.65, matching the theoretical value of 1.67, thus supporting the identification of HAp [204]. X-ray diffraction (XRD) analysis further corroborated these results, showing all characteristic diffraction peaks associated with HAp in the sample immersed for 28 days (Figure 61d) [205].

These findings indicate that copper does not inhibit bioactivity in the tested formulation, in agreement with previous studies on other Cu-doped bioactive glasses [206–208].

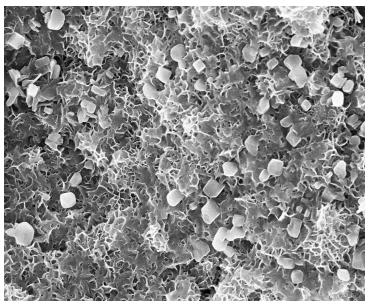

a)

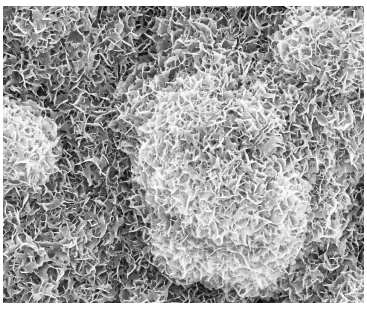

b)

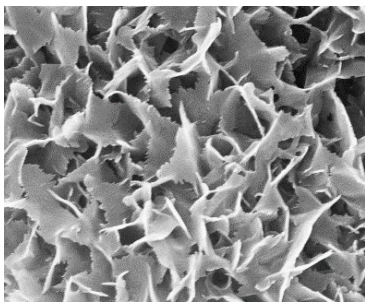

c)

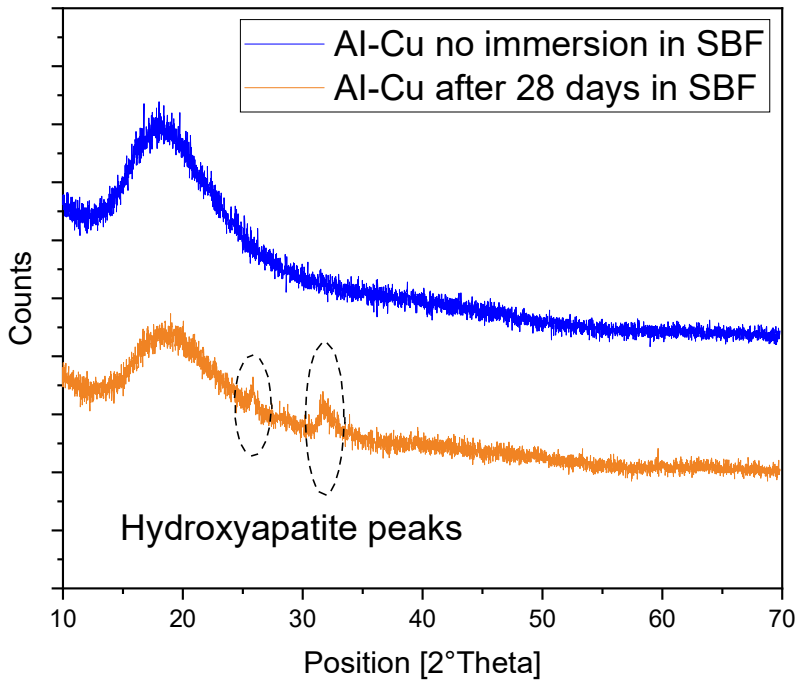

d)

Figure 61. Image of a) Crystal of HAp formed after 7 days, b) crystallized structure of HAp formed after 28 days, c) magnification of crystallized structure of HAp formed after 28 days. d) XRD of a A7I3-Cu sample not immersed in SBF (reference) and another sample immersed in SBF for 28 days. It is visually evident that the sample immersed in SBF for 28 days (orange line) contains the HAp peaks.

3.6.8 Cytocompatibility evaluation

Following the confirmation of successful silanization, copper doping and the possibility to favour the HAp growth, cytocompatibility was evaluated by human bone-marrow mesenchymal stem cell (hbMSC) attachment and spreading. hbMSCs, chosen for their capacity to differentiate into osteoblasts [209], were seeded directly onto scaffold surfaces and incubated for 24 h at 37 °C. Metabolic activity was quantified by the alamarBlue assay, and cell morphology was examined by SEM. AI-pristine served as the control.

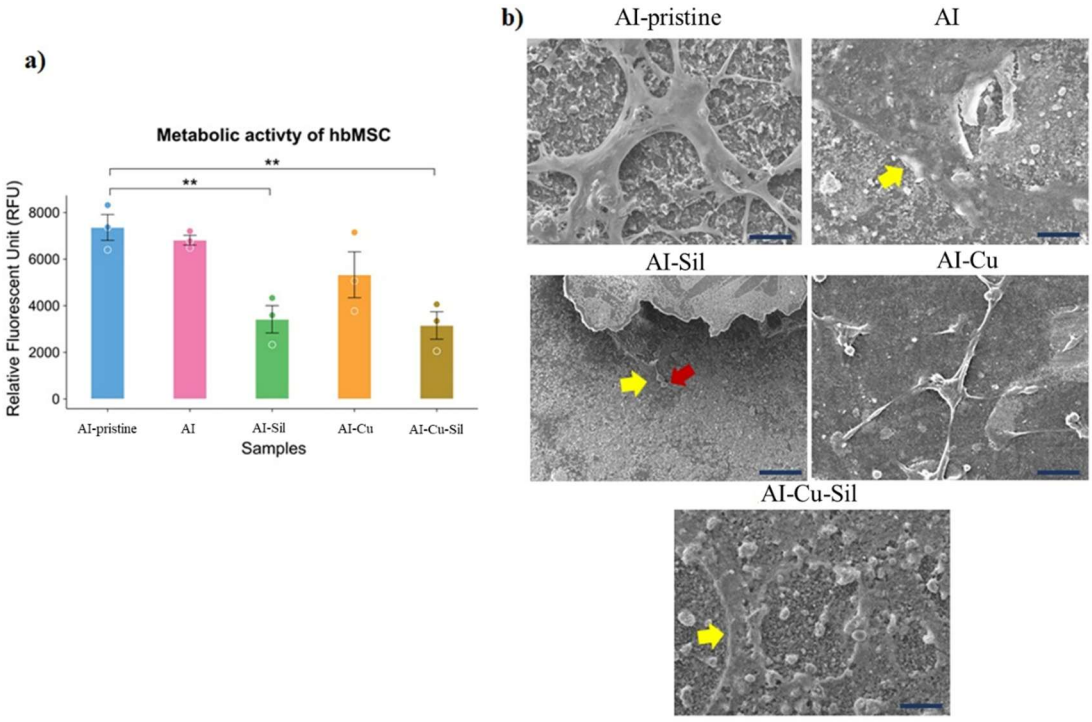

Figure 62. (a) represent the metabolic activity graph of hbMSC cells, while (b) shows SEM images of the same cells focusing on their morphology after 24h incubation at 37°C.

As shown in Figure 62a, hbMSC metabolic activity on AI and AI-Cu was comparable to the control ($p > 0.05$). In contrast, both silanized surfaces (AI-Sil and AI-Cu-Sil) lead to a significantly lower activity ($p < 0.01$), indicating either reduced cell adhesion or diminished cellular metabolism. SEM images (Figure 62b) confirmed that AI-pristine, AI, and AI-Cu supported well-spread cell morphologies, whereas AI-Sil exhibited fewer adherent cells (red arrows) and a less typical bar shape (yellow arrows). Although AI-Cu-Sil displayed spread cells, its metabolic activity remained low, suggesting that surface chemistry limits cell proliferation.

These observations correlate with contact-angle measurements: silanisation made the silanised BG surface hydrophobic ($96 \pm 2°$), compared to complete wetting (0°) of untreated BG. Increased hydrophobicity weakens protein adsorption and cell adhesion, explaining the reduced cell coverage and metabolic readings.

3.6.9 In Vitro Antibacterial Evaluation

To evaluate antimicrobial efficacy, *Staphylococcus aureus* (MRSA) bacteria were chosen as representative Gram-positive pathogens. Bacterial suspensions were inoculated directly onto scaffold surfaces (AI-pristine, AI, AI-Sil, AI-Cu, and

AI-Cu-Sil) and incubated for 24 h at 37 °C. Metabolic activity (alamarBlue), viable counts (CFU), and SEM imaging assessed bacterial adhesion and biofilm formation (Figure 64).

AlamarBlue results (Figure 63a) showed a significant reduction in metabolic activity on silanized surfaces compared to both AI-pristine and AI ($p < 0.05$). While AI-Cu also trended lower, this did not reach statistical significance. CFU assays (Figure 63b) indicated that AI-Sil, AI-Cu, and AI-Cu-Sil each supported ~57% fewer viable bacteria than control surfaces. SEM images (Figure 63c) revealed dense microcolonies on AI-pristine and AI surfaces, while treated surfaces exhibited only scattered single cells and minimal aggregates.

Quantitative analysis of 3D-reconstructed SEM data (Figure 64) demonstrated that untreated and non-silanised surfaces had ~13–14% surface coverage and up to ~4.5 µm biofilm thickness (3–4 bacterial layers). In contrast, Cu-doped and/or silanised surfaces displayed only 8–9% coverage and 2.5 µm maximum height, indicating disruption of multilayer biofilm formation. This single-cell distribution enhances bacterial exposure to antimicrobial agents.

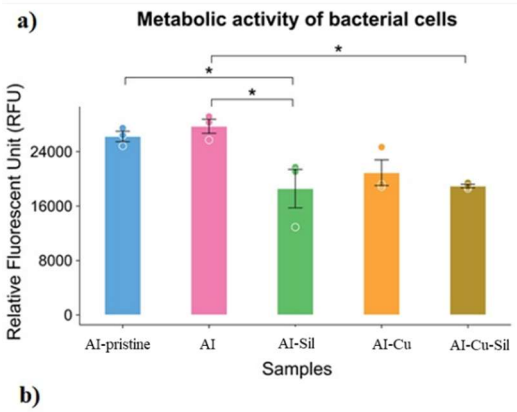

b)

Viable surface-adhered bacterial colonies count

Name of the samples	Number of colonies (×5×10⁶)	Reduction (%)
AI-pristine	3.5 (±0.7)	control
AI	3.5 (±0.7)	0
AI-Sil	1.5 (±2)	57
AI-Cu	1.5 (±0.7)	57
AI-Cu-Sil	1.5 (±2)	57

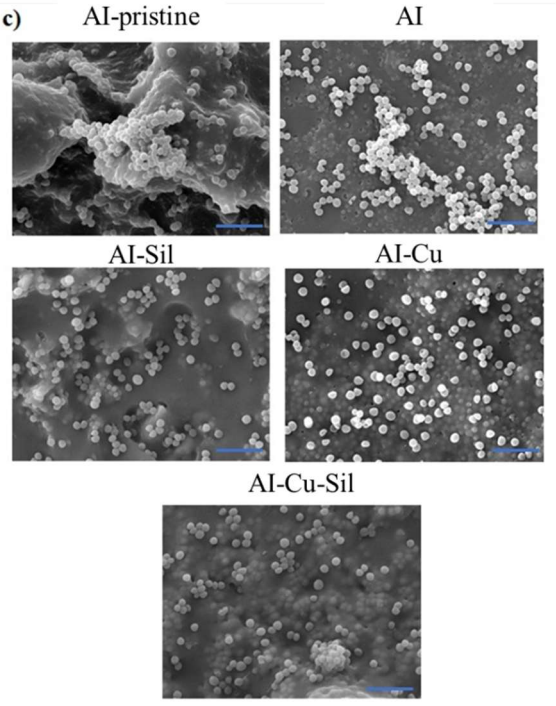

Figure 63. (a) represent the *Staphylococcus aureus* (MRSA) bacteria metabolic activity. (b) number of bacterial colonies and percentage reduction respect to control sample, chosen as the AI-pristine. (c) shows the SEM images of bacteria on top of all the samples taken in consideration.

a)

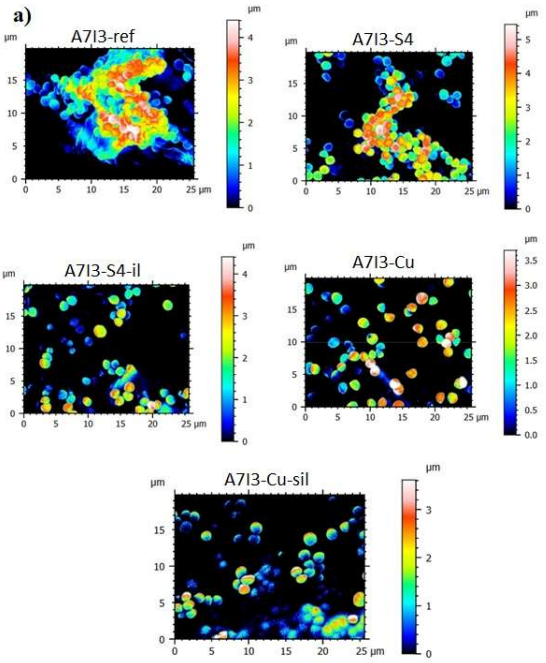

b)

Name of the samples	Occupied area (%)	Z-maximum (µm)
A7I3-ref	13	4.4
A7I3-S4	13.7	4.5
A7I3-S4-sil	9	3
A7I3-Cu	8	2.5
A7I3-Cu-sil	8.4	2.5

Figure 64. Quantitative analysis of 3D-reconstructed SEM data (a), and relative percentage of occupied area.

The pronounced antibacterial effect of Cu-doping is consistent with Cu-ion–mediated disruption of bacterial membranes, generation of reactive oxygen species, and enzymatic inhibition [210] as documented for Cu-doped bioactive glasses [211]. Silanisation further modulates surface wettability and may reduce initial bacterial adhesion. Taken together, these modifications yield scaffolds that resist biofilm formation while maintaining cytocompatibility.

3.7 Enhancing sustainability: hard tissue engineering scaffolds with increased functionality and reprocessability

Having demonstrated that silanisation and copper doping enhance both the mechanical and antimicrobial performance of the AESO-based scaffolds, the next research lies in giving these materials a dynamic covalent network, adding reprocessability properties to the final material. Traditional thermosets, even when bioactive and antibacterial, remain permanently crosslinked and cannot be reshaped or repaired once cured. To overcome this limitation, we then turned to dynamic covalent chemistry: by incorporating dynamic covalent bonds into the AESO/BG composite network, it becomes possible to combine the high performance and biofunctionality achieved thus far with the reprocessability of covalent adaptable networks. This can allow the material at the end of life to be recycled or reshaped, or, when necessary, it can be possible to achieve a repair in the final material. Moreover, as already seen in the first section of this chapter in the hydrogel-related work and in the Cu silanised work, the Te doping and the silanisation bring an optimal duo in enhancing the antibactericity of the material and improving the mechanical properties. To reach a fully sustainable scaffold, the aim is to recycle the scaffold at the end of its life or reshape it once the patient needs other shapes or after failure. In the following section, we explore the formulation and characterisation of a 3D-printed, tellurium-doped and silanised BG that will be used as a filler phase in AESO vitrimer scaffold, thereby coupling our scaffold design strategy with the dynamic covalent exchange mechanisms introduced in Chapter 2.

3.7.1 Resin formulation

Building upon the promising results obtained with the Cu and silane-modified scaffolds, we aimed to extend the functionality of our system by integrating exchangeable covalent network behaviour into the resin network. Vitrimers offer a unique advantage over conventional thermosets by introducing dynamic covalent exchange reactions, which allow for reprocessability, self-healing, and long-term structural adaptability, features particularly valuable in tissue engineering applications where scaffold remodelling may be beneficial. Following our previous work, the scaffold formulation was based on a 70:30 weight ratio of acrylated epoxidised soybean oil (AESO) and reactive diluent to reduce viscosity and ensure printability, in this case, acrylated eugenol (AEUG). The resin was loaded with 30 phr of tellurium-doped (BG-Te) and silanised bioactive glass (BG-Te-Sil) to confer

osteoinductive properties and 2 phr of phenylbis(2,4,6-trimethylbenzoyl)phosphine oxide as a photoinitiator. Finally, the transesterification reaction catalyst (eugenol phosphate EUGP) was introduced at a percentage of 10 phr. The formulation was first treated in an ultrasonic bath at 50 °C to ensure complete dissolution of the photoinitiator, followed by homogenization using a planetary mixer (Thinky Mixer ARE-250, Tokyo, Japan) to achieve uniform BG dispersion. 3D printing was done using a Prusa SL1S SPEED stereolithography printer (Czech Republic) equipped with a 405 nm UV light source. The initial layer was exposed for 120 s to ensure strong adhesion to the build platform, while subsequent layers were cured with 5 s exposures. Post-processing included ultrasonic cleaning in isopropanol for 15 minutes to remove uncured resin, followed by UV post-curing for 30 minutes using a Phrozen Cure Kit (Taiwan).

3.7.2 Photopolymerisation kinetics

The photoreactivity of AESO-based vitrimeric formulations was evaluated by Fourier-transform infrared spectroscopy (FTIR), photo-differential scanning calorimetry (Photo-DSC), and photorheology, as previously done in previous works. The values obtained for the investigated formulations are summarised in Table 15. The reference (pristine) formulation consisted of AESO and AEUG in a 70:30 ratio. To assess the effect of filler incorporation, two additional formulations were prepared by adding 30 phr of either tellurium-doped bioactive glass (BG-Te) or its silanized counterpart (BG-Te-Sil). All formulations included 10 phr of a bio-based transesterification catalyst, eugenol phosphate (EUGP), to promote dynamic covalent network formation. The catalyst content was optimised in preliminary stress-relaxation tests to ensure vitrimeric behaviour [212].

The conversion of acrylic double bonds during UV exposure was monitored by FTIR spectroscopy by following the reduction of the C=C stretching peak at 1640 cm^{-1} over time. Figure 65 presents the real-time conversion curves and representative spectra, while Table 15 reports the final conversions after 2 minutes of irradiation. The pristine formulation achieved a high conversion of ~86%, while the incorporation of BG-Te reduced the conversion to ~80%. A more pronounced decrease was observed with BG-Te-Sil, where the final conversion dropped to ~54%. This reduction in reactivity is attributed to a dual effect: (i) competition for light absorption between the photoinitiator and the bioactive glass particles and (ii) scattering of UV light caused by the micrometric dimensions of the filler, which limits the penetration of radiation through the resin.

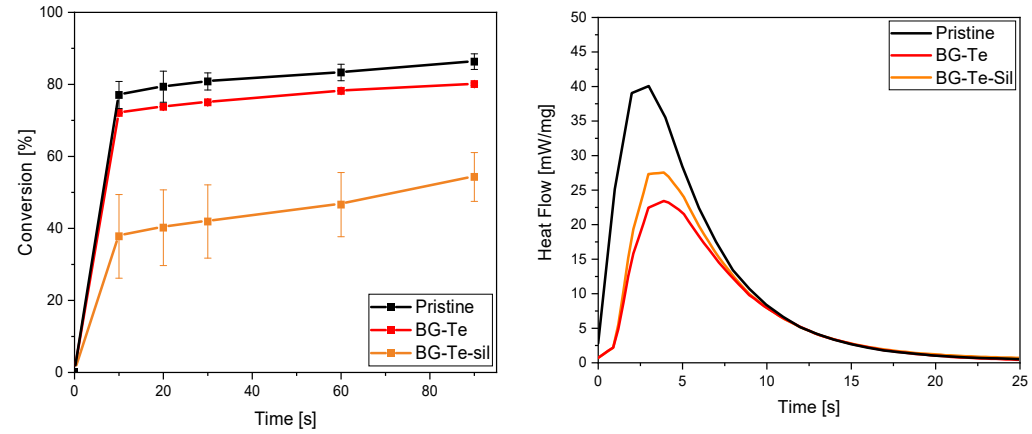

(a) (b)

Figure 65. (a) FTIR conversion curves obtained by following the acrylate peak decrease. (b) Heat released by the photocuring reaction measured by photoDSC.

Table 15. Conversion and heat flow measured by FTIR and photoDSC.

Formulation	**Conversion [%]**	**Heat Flow [J/g]²**
AESO-AEUG 70:30 (**Pristine**)	86±2	215.4±16.4
Pristine + 30 phr BG-Te (**BG-Te**)	80±0.3	175.5±17.5
Pristine + 30 phr BG-Te-Sil (**BG-Te-Sil**)	54±6.8	189.5±1.2

Photo-DSC experiments, reported in Figure 65b, further integrate the FTIR findings. The total heat released during polymerisation was highest for the pristine formulation (~215 J/g), and decreased upon filler incorporation to 175 J/g (BG-Te) and 189 J/g (BG-Te-Sil). Moreover, both filled formulations exhibited an increase in the time required to reach the maximum heat flow, indicating a slower polymerisation process. Interestingly, despite the significantly lower FTIR conversion observed for the BG-Te-Sil formulation, its heat flow was comparable to BG-Te. This discrepancy is attributed to the presence of methacrylate groups in the silanizing agent, which are thermally reactive but not detected in the monitored

FTIR band. In contrast, Photo-DSC captures the total exothermic signal, regardless of functional group identity, accounting for this divergence.

Photorheology experiments were conducted to confirm the curing efficiency and to monitor gelation dynamics. As shown in Figure 66, all formulations exhibited a sharp increase in storage modulus (G') upon light exposure, reaching a plateau within approximately 20 seconds. This rapid modulus increase confirms effective photoinitiator activation and network formation in all cases, including the filled formulations.

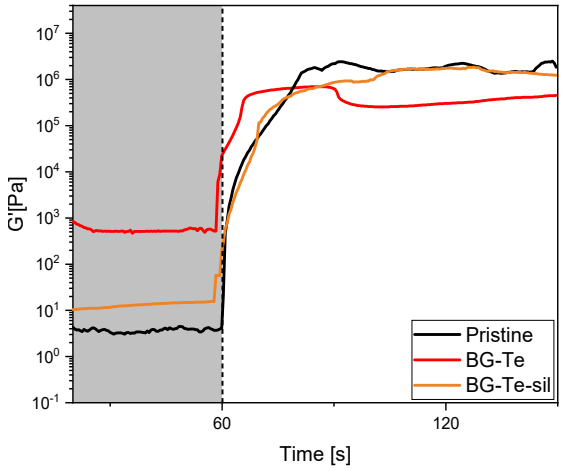

Figure 66. Photorheology measurement performed across all Te-BG filled formulations.

3.7.3 3D printing

Having optimised resin rheology and photo-curing, all formulations were printed into three-dimensional scaffolds using a Prusa SL1S SPEED stereolithography printer equipped with a 405 nm light source. Viscosity measurements confirmed Newtonian behaviour through the relevant shear range, with viscosities within the 0.5–2 Pa·s window recommended for SLA/DLP printing [213,214].

Printing parameters were set to a 120 s exposure for the first layer (to ensure adhesion) and 5 s for subsequent layers. Rectangular DMTA specimens, tensile "dog-bone" samples, compression cubes, and complex hollow structures were successfully produced from both the pristine AESO/AEUG resin and the BG-Te and BG-Te-Sil composites. An example structure (Figure 67) illustrates the high fidelity and resolution achievable, even with 30 phr inorganic loading.

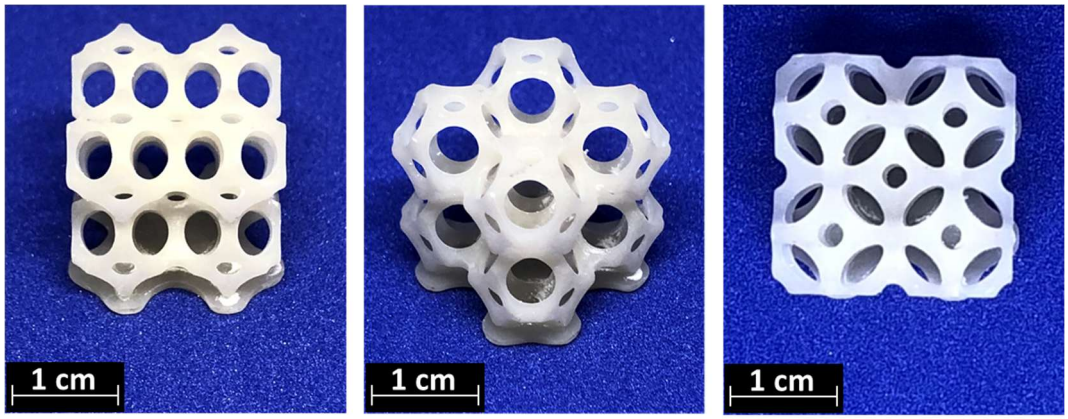

Figure 67. 3D printed structures obtained for the BG-Te filled formulation.

3.7.4 Thermomechanical properties

Viscoelastic properties were measured by DMTA in tensile mode from –20 °C to 150 °C at 1 Hz. Storage modulus (E′) and tan δ curves appear in Figure 68, with T_g values summarised in Table 16. The unfilled resin exhibited T_g of 68 °C, while BG-Te and BG-Te-Sil composites displayed lower T_g (61 °C and 64 °C, respectively). The reduction in T_g correlates with the modest decrease in double-bond conversion upon filler addition. Silanisation partially reduced this drop, likely by promoting better crosslinking near the particle interface, but overall, the inorganic particles slightly increase the mobility of the network.

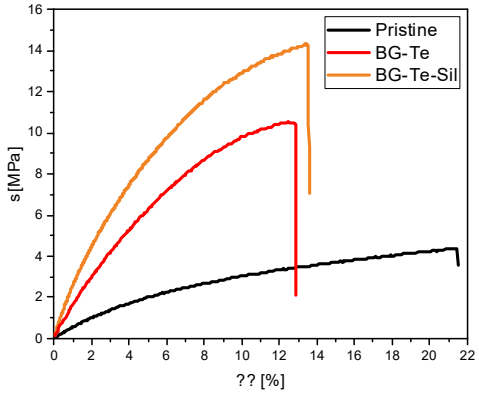

(a) (b)

Figure 68. (a) represent the DMTA graph obtained across all formulations, while (b) corresponds to the tensile tests.

Table 16. Value obtained from tensile test across all formulations.

Formulation	T_g [°C]	Young modulus (E) [MPa]	Stress at break (σb) [MPa]	Strain at break (εb) [%]
(**Pristine**)	68±2	0.5±0.1	4.8±0.8	28±5
(**BG-Te**)	61±1	1.4±0.0	10.5±0.0	10±0
(**BG-Te-sil**)	64±1	1.5±0.0	14.0±0.0	13±2

Mechanical properties of the 3D-printed scaffolds were evaluated by uniaxial tensile testing. Stress–strain curves for the pristine, BG-Te, and BG-Te-Sil samples are presented in Figure 69, and Young's modulus (E), ultimate tensile strength (σ_n), and elongation at break (ε_b) are summarised in Table 16.

Silanisation produced a clear enhancement in mechanical performance: compared to BG-Te, the BG-Te-Sil scaffolds exhibited significantly higher stiffness and strength. This improvement derives from stronger filler–matrix adhesion imparted by the methacrylate groups on the silane-modified glass surface, as evidenced by FESEM images of fractured surfaces (Figure 70), which show voids (red arrows) and particle pull-out in BG-Te but complete encapsulation of BG-Te-Sil particles by the polymer matrix.

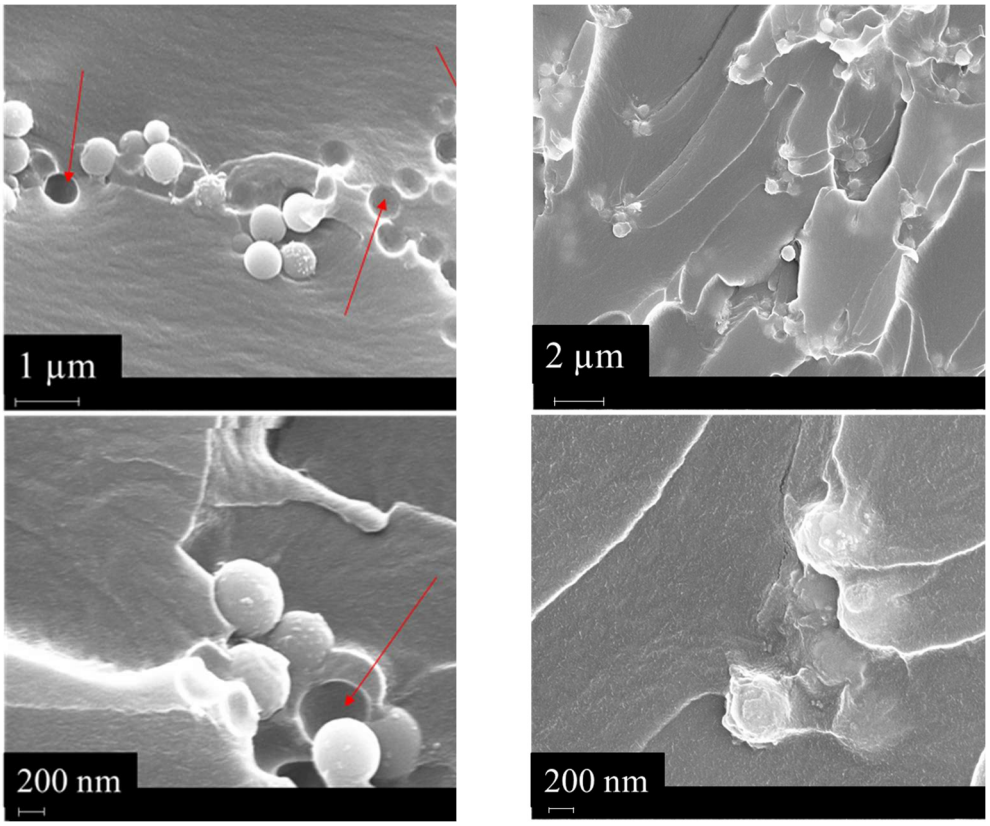

Figure 69. (a) FESEM image of BG-Te surface and (b) FESEM image of BG-Te-Sil surface.

In native tissues, trabecular bone modulus ranges from 10 to 3000 MPa [215]. In a scaffold, it is important to meet the mechanical properties of the tissue replacement. Although these materials lie at the lower end of this range, 3D printing structures, particularly pore architecture and structure density, offer a route to enhance the effective stiffness [216]. Moreover, in vivo remodelling and tissue ingrowth typically increase composite stiffness over in vitro values [217].

The versatility of these composites also extends to soft tissues: human skin exhibits Young's moduli between 0.3 and 20 MPa along the tibial axis [218] , overlapping with the properties of our scaffolds and suggesting broader applicability across different tissue-engineering contexts.

3.7.5 Stress relaxation measurements

In the previous chapter, it was shown that the reprocessability of the thermoset can be allowed by the dynamic covalent network. Here, thanks to the chemical

structure of AESO, it is possible to obtain again this property, since the AESO monomer possesses both -OH groups and ester groups, which together are used in the transesterification reactions, allowing the material to be reshaped or recycled at the end of life. Having introduced the bio-based AESO/AEUG matrix and demonstrated its reinforcement and bioactivity, we now assess whether these 3D-printed composites truly exhibit dynamic covalent network properties.

Stress-relaxation experiments were performed on 3D-printed scaffolds containing 30 phr Te-doped bioactive glass (BG-Te) and 10 phr eugenol phosphate catalyst (EUGP), the catalyst loading optimised in the previous chapter, to enable rapid exchange. Samples were first pre-equilibrated at each test temperature (150–220 °C, below their degradation onset), then subjected to a constant 3% strain while monitoring the decay of the relaxation modulus G(t) over time. The normalised modulus follows an exponential decay.

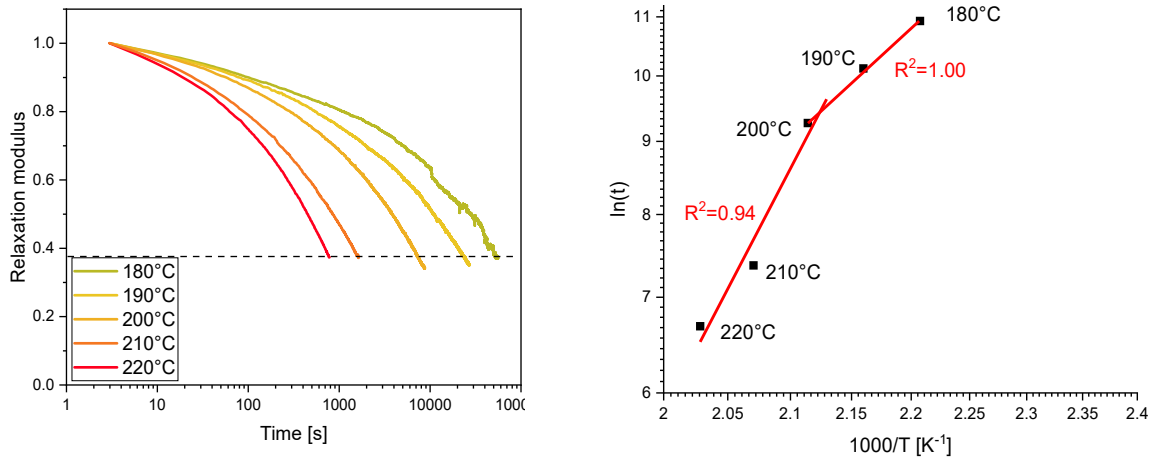

(a) (b)

Figure 70. (a) Stress relaxation curves obtained for BG-Te-Sil and its relative Arrhenius plot (b)

Figure 70a shows that at 180 °C, these composites reach the relaxation within several minutes, and τ, the time needed to reach the 1/e of the initial G(t), decreases further at higher temperatures. Plotting the ln(τ) against 1000/T [K^{-1}] yields the Arrhenius relationship characteristic of associative exchange mechanisms (Figure 72b). Notably, the data exhibit two distinct linear regimes, mirroring the double-slope behaviour first reported by Hubbard et al. in our first vitrimer study [212,219], indicating a change in the rate-limiting step from chain mobility at lower temperatures to bond exchange at higher temperatures.

By demonstrating both rapid stress relaxation above 180 °C and an Arrhenius-governed temperature dependence, these results confirm that the 3D-printed AESO/AEUG–BG-Te composites can be used as reprocessable thermosets. This

stress-relaxation behaviour provides a direct bridge between the covalent adaptable network concepts introduced in Chapter 2 and the bioactive, mechanically robust scaffolds developed in this chapter, unifying dynamic reprocessability with personalised scaffold performance.

3.7.6 Biological evaluation
In vitro bioactivity test

To determine hydroxyapatite (HAp) formation, the bone precursor mineral phase, scaffolds were immersed in Kokubo's SBF solution at 37 °C for 28 days. FESEM images (Figure 71a–b) show the typical in vitro grown HAp morphology and extensive HAp lamellae by 28 days on both BG-Te and BG-Te-Sil surfaces. It is evident that the typical HAp formation in vitro is present on the scaffold surface, indicating that if placed in vivo, these materials can support human bone formation by growing first their precursor.

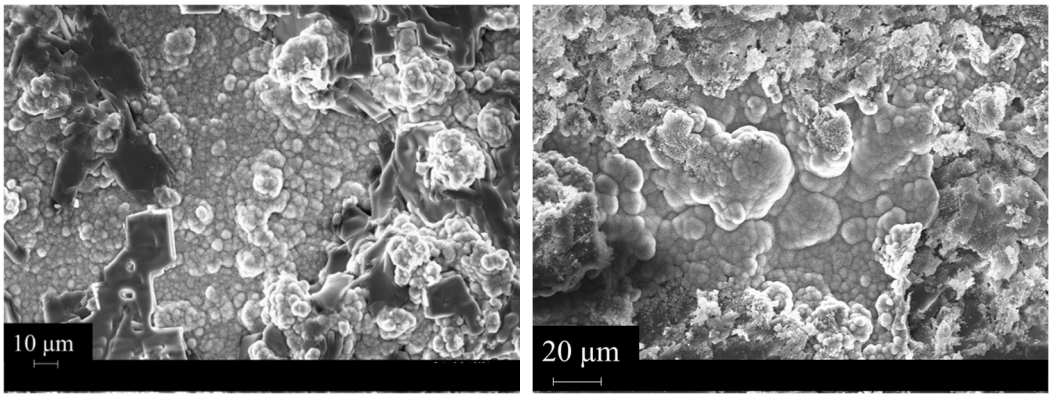

a) b)

Figure 71. (a) FESEM image of BG-Te surface after 28 days of SBF soaking and b) FESEM image of BG-Te-Sil surface after 28 days of SBF soaking.

Cytocompatibility of 3D-Printed Scaffolds

Human bone-marrow mesenchymal stem cells (hBMSCs) were used to assess direct cytocompatibility, given their relevance to bone regeneration [220]. Cells were seeded directly onto pristine, BG-Te, and BG-Te-Sil scaffolds and incubated for 24 h at 37 °C. Metabolic activity was quantified by alamarBlue (RFU; Figure 72a), and cytotoxicity was evaluated via LDH release following ISO 10993-5. All samples maintained > 70% viability with respect to the pristine material (Figure 72 b), indicating non-toxic behaviour. SEM and dual live/dead (green)/NucBlue (blue) fluorescence imaging (Figure72c) confirmed extensive cell

attachment and spreading, with negligible cell death. These results align with prior findings that a 70:30 AESO:IBOA resin containing 30 phr BG is highly cytocompatible [186], and demonstrate that substituting Te-doped and silanized Te-doped glasses does not compromise hBMSC viability or morphology.

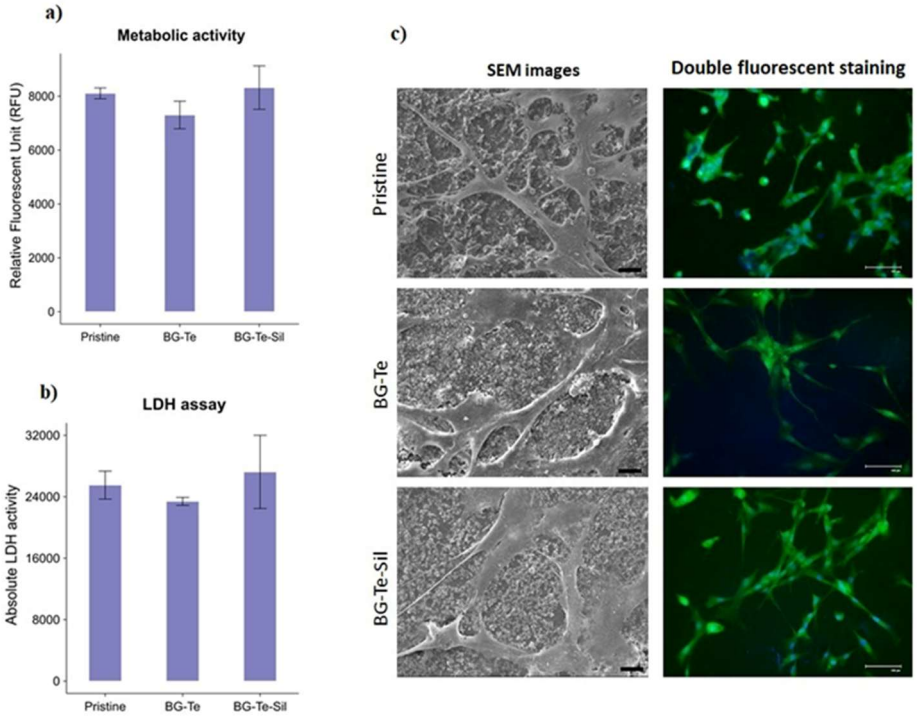

Figure 72. Metabolic activity measured by (a) alamar blue assay, (b) LDH release. (c) reports the SEM images and the stained cells.

Antibacterial Activity of 3D-Printed Scaffolds

The antibacterial efficacy of the Te-containing scaffolds, given by the Te effect, was evaluated against *Staphylococcus aureus* via direct contact and 24 h incubation at 37 °C. Metabolic activity (alamarBlue), CFU counts, and SEM morphology are shown in Figure 73. BG-Te scaffolds reduced bacterial metabolic activity relative to pristine and BG-Te-Sil samples, though not significantly ($p > 0.05$; Figure 73a). CFU analysis (Figure 73b) revealed that BG-Te surfaces had 87% fewer bacteria than pristine controls and 54% fewer than BG-Te-Sil. SEM images (Figure 73c), with bacteria highlighted in orange via SMILE VIEW™, show dense micro-biofilms on pristine and BG-Te-Sil, whereas BG-Te surfaces exhibit only scattered single cells.

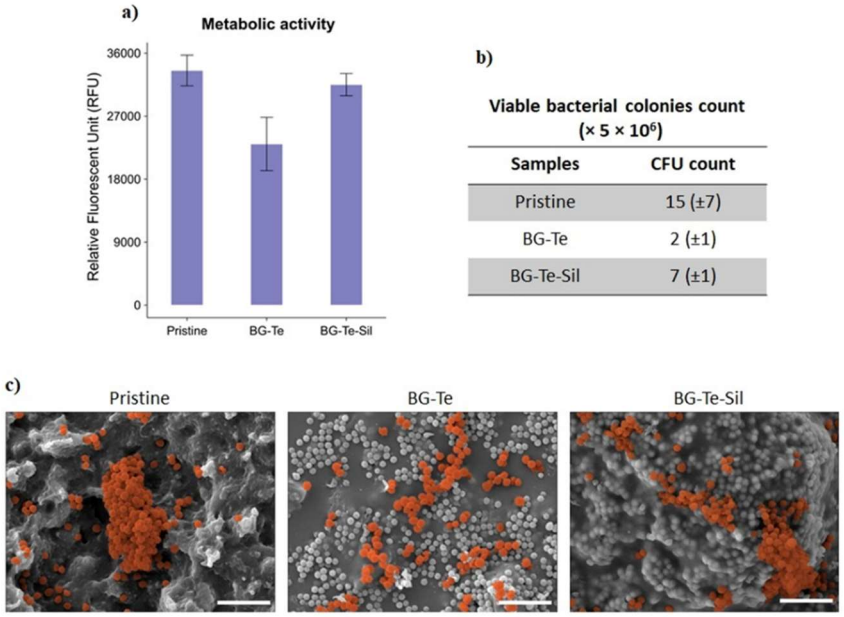

Figure 73. Metabolic activity of bacteria seeded on the scaffold (a). (b) is the relative data of viable bacterial colonies and (c) represent the SEM images of samples containing bacteria, shown in red.

The diminished efficacy of BG-Te-Sil is attributed to silane coverage of Te sites, which likely hinders bacterial uptake of Te and its antimicrobial mechanisms. This interpretation is consistent with literature demonstrating dose-dependent antibacterial effects of Te-containing bioactive glasses against Gram-positive pathogens and with studies showing that intracellular Te disrupts key bacterial enzymes and biofilm formation [135,221].

3.8 Comparison of developed bio-based scaffolds relative to literature tissue engineering systems

The bio-based composite scaffolds developed in this thesis possess a combination of mechanical stiffness, porosity, bioactivity and biological function, reflecting the diverse requirements of soft-to-hard tissue regeneration. To contextualise these systems within the framework of contemporary tissue engineering platforms, a comprehensive comparative analysis is presented across all four scaffold platforms developed: methacrylated chitosan hydrogels reinforced with tellurium-doped bioactive glasses, thiol-ene polyHIPE foams, 3D-printed acrylated epoxidised soybean oil (AESO) composites reinforced with Cu/Te-doped bioactive glasses,

and reprocessable AESO scaffolds incorporating dynamic transesterification chemistry.

3.8.1 Chitosan-based hydrogels for soft tissue engineering, comparative analysis

The methacrylated chitosan (MCHIT) formulations developed in this work achieve compression moduli of 87 ± 25 kPa (pristine) to 246 ± 51 kPa (MCHIT3), placing them within the traditional performance for chitosan-based tissue engineering scaffolds. Unmodified chitosan hydrogels reported in the literature typically achieve compression moduli in the same order of magnitude, ranging from kPa, while chitosan reinforced with bioactive glass nanoparticles demonstrates moduli spanning hundreds of kPa, consistent with the present results.[222–224]

The key distinguishing feature of the MCHIT-Te-Sil system is the incorporation of tellurium-doped, silanized bioactive glass, which combines osteoconductive bioactivity with antimicrobial properties rarely achieved in standard chitosan-BG composites. The antibacterial efficacy against Staphylococcus aureus (inhibition of>80%) makes these hydrogels applicable to various applications where infection prevention is as critical as tissue regeneration. The cytocompatibility and anti-inflammatory profile (minimal upregulation of pro-inflammatory genes, including IL-1β, TNF-α, and IFN-γ) aligns favourably with published chitosan-BG composites, confirming that tellurium doping and silanization do not compromise cellular tolerance. The swelling behaviour (~58–65%) is consistent with literature chitosan hydrogels and supports adequate nutrient diffusion and cell infiltration. This intermediate mechanical and biological profile makes MCHIT-Te-Sil systems particularly well-suited for applications in soft tissue interfaces.

3.8.2 Thiol-ene polyHIPE scaffolds, comparative analysis

The UV-initiated thiol-ene polymerisation of acrylated epoxidised soybean oil (AESO) and Trimethylolpropane tris(3-mercaptopropionate) (TMPTMP) via high internal phase emulsion (HIPE) templating yielded scaffolds with high porosity and pore sizes of 8–10 μm, closely resembling the morphology of cancellous bone. The compression moduli achieved in this work (pristine: 64 ± 5 kPa; PHI15: 136 ± 16 kPa; PHI30: 174 ± 25 kPa) match the lower range of cancellous bone (0.1–1000 MPa), and align with reported polyHIPE systems incorporating bioactive fillers. These values are substantially similar to those of rigid ceramic scaffolds with the same porosity (hydroxyapatite/collagen composites: kPa modulus range) and

comparable to those of pure elastomeric polyHIPE foams without reinforcement, reflecting the favourable mechanical balance of the AESO-TMPTMP platform for scaffolding applications.[225–227]

The metabolic activity results (Resazurin assay, Figure 43) demonstrate robust cell proliferation and metabolic function on pristine and BG-reinforced scaffolds, with trends consistent with those observed in published polyHIPE systems. Mineralisation assays (Figure 45) demonstrate positive mineral deposition (hydroxyapatite formation) at 28 days, confirming the bioactivity conferred by bioactive glass reinforcement and validating the suitability of this platform for osteogenic applications.

3.8.3 3D-printed AESO-BG scaffolds, comparative analysis

The progression from HIPE-templated foams to 3D-printed AESO composites reinforced with Cu- and Te-doped, silanized bioactive glasses (A7I3-Cu-Sil, A7I3-Te-Sil) represents an advancement in scaffold control: additive manufacturing enables precise tuning of pore size, interconnectivity, and geometry to achieve patient-specific or anatomically optimised manufacts. The tensile Young's modulus of 3D-printed AESO-BG scaffolds achieved in this work (0.5–2 MPa range) represents a favourable intermediate mechanical window between soft polymeric foams and rigid ceramic composites. Lebedevaite et al. reported that "acrylated epoxidised soybean oil (AESO)-based composites show improved mechanical properties and glass transition temperatures with filler loading", consistent with the present findings, where Cu/Te-doped BG incorporation enhanced both stiffness and thermal stability. The glass transition temperature range achieved (T_g 60–70 °C) aligns with literature data for AESO-based systems; Zhang et al. noted that "BG/cellulose scaffolds have compressive strength values of 4.54–27.0 ± 1.65 MPa, satisfying the strength requirement of human trabecular bone (2–12 MPa),". The present AESO-BG moduli (0.5–2 MPa) fall within the lower end of the trabecular bone range, which is suitable for intermediate-stiffness applications. This higher stiffness and T_g, if compared to polyHIPE foams (which achieved 64–174 kPa), reflect a transition toward load-bearing applications. The modulus range (0.5–2 MPa) remains substantially lower than that of rigid ceramic-reinforced scaffolds, thereby suggesting a specific application suitable for cartilage and intermediate tissue interfaces. The elemental doping strategy (Cu for angiogenic promotion, Te for antimicrobial activity) introduces multifunctionality beyond the inherent bioactivity of the base glass composition, distinguishing these scaffolds from conventional BG-reinforced polymeric systems that lack such enhanced biological properties. In vitro bioactivity testing (SBF immersion, Figure 61) demonstrates

hydroxyapatite crystallization at 28 days, confirming that the polymer matrix and Cu/Te doping do not weaken glass bioactivity. Cytocompatibility with human bone marrow–derived mesenchymal stem cells (hbMSCs, Figure 62) and antibacterial activity against MRSA (Figure 63) are consistent with or exceed literature values for 3D-printed bioactive scaffolds. Relative to alternative 3D printing approaches for bone tissue engineering (SLS of ceramics, FDM of PCL/PLGA, SLA of synthetic acrylates), the AESO-BG platform combines the advantages of UV-curing (rapid, high resolution, low temperature process), bio-based feedstock (100% AESO content), and integrated bioactivity (Cu/Te-doped BG) in a single material system. [228–233]

Conclusions

In summary, this chapter demonstrates the fabrication and potential of scaffolds derived from biobased monomers and photocured. The first work related to hydrogel showed the potential of chitosan and the bioactive glass reinforcement in soft tissue applications. Starting from soft tissue and moving to hard tissue, the use of acrylated-epoxidized soybean oil (AESO)-based scaffolds, whether formulated as thiol–ene polyHIPE foams or vat-photopolymerized constructs, has demonstrated a versatile combination of sustainability, processability, and biofunctionality. By adapting the reactive diluent content (IBOA or eugenol derivatives) and dispersing sol–gel-derived bioactive glasses, including silanized, copper-doped, or tellurium-doped variants, these materials rapidly cure under low-intensity UV light into networks where porosity, mechanical stiffness, and surface chemistry can be independently tuned.

The AESO formulations can achieve rapid photocuring, with over 80 per cent double-bond conversion within seconds, as confirmed by ATR-FTIR, photo-DSC, and photorheology, supporting high-resolution 3D printing without the need for added photoabsorbers.

Moreover, they present controlled mechanical properties by incorporation of 10–30 phr bioactive glass, which increases tensile and compressive moduli into the MPa range, with silanization further enhancing polymer–glass adhesion to boost strength by up to 70 per cent.

The bioactivity and antimicrobial function of both Cu- and Te-doped glasses have been shown. The bioactive glasses catalyse rapid hydroxyapatite nucleation in SBF and reduce *S. aureus* biofilm formation, while maintaining hBMSC viability and spreading, thereby merging osteoconductivity with infection resistance.

Finally, the dynamic reprocessability was shown: AESO/AEUG composites with eugenol-based transesterification catalysts display Arrhenius-type

stress-relaxation above 180 °C, enabling reshaping and recycling without compromising network integrity.

Together, these projects position AESO-based scaffolds as promising candidates for patient-specific bone repair, as their renewable origin and low-energy UV processing meet sustainability requirements, while their customizable architecture, mechanical properties, and integrated bioactive/antimicrobial functions meet clinical demands for complex defect regeneration.

The work described in this chapter has been published and is available at the following references:

[186] Bergoglio, M.; Najmi, Z.; Cochis, A.; Miola, M.; Vernè, E.; Sangermano, M. UV-Cured Bio-Based Acrylated Soybean Oil Scaffold Reinforced with Bioactive Glasses. Polymers (Basel) 2023, 15, doi:10.3390/polym15204089.

[187]Bergoglio, M.; Najmi, Z.; Cochis, A.; Miola, M.; Vernè, E.; Sangermano, M. Silanized and Cu-Doped Bioactive Glass as Filler for Biobased Photocurable 3D Printed Scaffolds. Mater Today Chem 2025, 44, 102559, doi:10.1016/J.MTCHEM.2025.102559.

[188] Bergoglio, M.; Kriehuber, M.; Sölle, B.; Rossegger, E.; Schlögl, S.; Najmi, Z.; Cochis, A.; Ferla, F.; Miola, M.; Vernè, E.; et al. 3D-Printed Acrylated Soybean Oil Scaffolds with Vitrimeric Properties Reinforced by Tellurium-Doped Bioactive Glass. Polymers (Basel) 2024, 16, 3614, doi:10.3390/polym16243614.

[234] Bergoglio, M.; Najmi, Z.; Ferla, F.; Scalia, A.C.; Cochis, A.; Rimondini, L.; Vernè, E.; Sangermano, M.; Miola, M. Tellurium-Doped Silanised Bioactive Glass–Chitosan Hydrogels: A Dual Action for Antimicrobial and Osteoconductive Platforms. *Polymers (Basel)* **2025**, *17*, 1651, doi:10.3390/polym17121651.

[235] Bergoglio, M.; Miola, M.; Vernè, E.; Sangermano, M.; Cameron, Neil R. 3D-Printed Biobased Porous Polymer Scaffolds Reinforced with Bioactive Glasses by High Internal Phase Emulsion Polymerization. Biomacromolecules **2025,** doi: 10.1021/acs.biomac.5c01413.

Chapter 4: Conclusion

The work presented in this thesis focuses on a dual challenge: the need for sustainable thermoset polymeric materials and the demand for advanced functional systems in both industrial and biomedical applications. The research was framed within the principles of green chemistry, focusing on renewable monomers, environmentally friendly UV curing techniques, and functional enhancement through network design and advanced fillers like carbon nanotubes and bioactive glasses. The approach was articulated into two main research lines, each corresponding to a thematic chapter of the thesis, but interconnected by a common conceptual focus: the design of bio-based thermosets with tailored properties for demanding applications.

The first part of the work was dedicated to the development of biobased vitrimeric epoxy networks using epoxidised castor oil as the primary bioderived monomer. By introducing a suitable transesterification catalyst and at a certain condition of temperature and pressure, the epoxy systems were able to activate the covalent adaptable networks (CANs), enabling reprocessing and reshaping while maintaining the thermoset nature of the material. This fundamental shift from traditional irreversibility to controlled dynamic exchange reactions provided a sustainable solution to the waste problem typically associated with thermosets. Beyond their reprocessability, these systems were further engineered by incorporating multiwalled carbon nanotubes (MWCNTs), creating composites with both reprocessability and electrical conductivity. This opened opportunities in areas such as smart coatings, conductive adhesives, and structural components where repairability and multifunctionality are critical. Importantly, the results demonstrated that high levels of bio-based content can meet the demand of advanced functional performance, changing the perception that sustainability requires weak material properties.

The second part of the thesis moved from the industrially oriented vitrimeric coating networks to bio-derived scaffolds for tissue engineering, representing a direct application of sustainable materials in the biomedical field. The work began with the development of chitosan-based hydrogels incorporating tellurium-doped and silanized bioactive glasses (BGs). These multifunctional hydrogels combined

the intrinsic biocompatibility of chitosan with the osteoconductive and antimicrobial properties of the modified BGs, producing systems that could potentially address both regeneration and infection control in soft tissue repair.

Building on this first work, the focus shifted to high internal phase emulsion (HIPE) templating as a route to generate highly porous polyHIPE scaffolds starting from the biobased acrylated epoxidised soybean oil (AESO) in combination with trimethylolpropane tris(3-mercaptopropionate) (TMPTMP) via thiol–ene photopolymerization. The resulting interconnected pore structure, comparable with the cancellous bone, was ideal for supporting cell adhesion, proliferation, and nutrient diffusion. These scaffolds were reinforced again with BG to stimulate and induce bone formation while maintaining the cells' proliferation, as demonstrated by Resazurin assay, cell staining, and Osteoimage assay performed on the scaffolds. Furthermore, the adoption of 3D printing manufacturing method enabled the fabrication of scaffolds with custom geometries, allowing patient-specific designs and controlled porosity gradients.

The exploration of BGs went beyond conventional formulations: Cu-doping was introduced for enhanced antimicrobial activity, Te-doping for combined antimicrobial and antioxidant functions, and silanization to improve filler–matrix interfacial bonding. The last work merged the concepts from both chapters: AESO-based scaffolds BGs reinforced with vitrimeric properties, enabling reprocessing of 3D-printed scaffolds without compromising their structural integrity or porosity. This achievement symbolically and technically “closed the loop” between the industrial and biomedical research lines, demonstrating that the principles of reprocessability and circular economy can be applied even to biomaterials used for scaffolds.

In summary, this thesis has shown that it is possible to merge renewable monomers, dynamic covalent chemistry, functional fillers, and advanced manufacturing techniques to produce thermosets and composites that are not only sustainable but also designed for specific applications. The results bridge the gap between sustainability and performance, offering concrete pathways towards circular economy models in both industrial and biomedical sectors.

Looking ahead, future research could focus on scaling up the synthesis and processing methods, exploring self-healing, shape-memory, or stimuli-responsive behaviours in vitrimeric systems, which could be used as a matrix for further multifunctional composites, and conducting in vivo testing after having optimised in terms of BGs quantity and mechanical properties the most promising scaffold formulations. Such developments would not only validate the laboratory findings

but also accelerate the translation of these sustainable, multifunctional materials into real-world applications, reinforcing the idea that high-performance polymer science and environmental sustainability can coexist.

Appendix A

A1 List of publications

Related to the PhD project

1) Bergoglio, M.; Reisinger, D.; Schlögl, S.; Griesser, T.; Sangermano, M. Sustainable Bio-Based UV-Cured Epoxy Vitrimer from Castor Oil. Polymers 2023, 15, 1024. https://doi.org/10.3390/polym15041024
2) M. Sangermano, M. Bergoglio, S. Schögl, Biobased Vitrimeric Epoxy Networks. Macromol. Mater. Eng. 2024, 309, 2300371. https://doi.org/10.1002/mame.202300371
3) Matteo Bergoglio, Gabriele Palazzo, David Reisinger, Matilde Porcarello, Galder Kortaberria, Sandra Schlögl, Marco Sangermano, Cationic UV-curing of bio-based epoxidized castor oil vitrimers with electrically conductive properties, Reactive and Functional Polymers, Volume 200, 2024, 105936, ISSN 1381-5148, https://doi.org/10.1016/j.reactfunctpolym.2024.105936.
4) Bergoglio, M.; Najmi, Z.; Ferla, F.; Scalia, A.C.; Cochis, A.; Rimondini, L.; Vernè, E.; Sangermano, M.; Miola, M. Tellurium-Doped Silanised Bioactive Glass–Chitosan Hydrogels: A Dual Action for Antimicrobial and Osteoconductive Platforms. Polymers 2025, 17, 1651. https://doi.org/10.3390/polym17121651
5) Bergoglio, M.; Najmi, Z.; Cochis, A.; Miola, M.; Vernè, E.; Sangermano, M. UV-Cured Bio-Based Acrylated Soybean Oil Scaffold Reinforced with Bioactive Glasses. Polymers 2023, 15, 4089. https://doi.org/10.3390/polym15204089
6) Matteo Bergoglio, Ziba Najmi, Andrea Cochis, Marta Miola, Enrica Vernè, Marco Sangermano, Silanized and Cu-doped bioactive glass as filler for biobased photocurable 3D printed scaffolds, Materials Today Chemistry, Volume 44, 2025, 102559, ISSN 2468-5194, https://doi.org/10.1016/j.mtchem.2025.102559.
7) Bergoglio M, Kriehuber M, Sölle B, Rossegger E, Schlögl S, Najmi Z, Cochis A, Ferla F, Miola M, Vernè E, Sangermano M. 3D-Printed Acrylated Soybean Oil Scaffolds with Vitrimeric Properties Reinforced by Tellurium-

Doped Bioactive Glass. Polymers (Basel). 2024 Dec 23;16(24):3614. doi: 10.3390/polym16243614. PMID: 39771465; PMCID: PMC11679437.

8) Bergoglio, M.; Miola, M.; Vernè, E.; Sangermano, M.; Cameron, N.R. 3D-Printed Biobased Porous Polymer Scaffolds Reinforced with Bioactive Glasses by High Internal Phase Emulsion Polymerization. *Biomacromolecules* 2025, *26*, 8548–8559, doi:10.1021/acs.biomac.5c01413.

Unrelated to the PhD project

1) S. Subramaniyan, M. Bergoglio, M. Sangermano, M. Hakkarainen, Vanillin-Derived Thermally Reprocessable and Chemically Recyclable Schiff-Base Epoxy Thermosets. Global Challenges 2023, 7, 2200234. https://doi.org/10.1002/gch2.202200234
2) Bergoglio, M.; Rossegger, E.; Schlögl, S.; Griesser, T.; Waly, C.; Arbeiter, F.; Sangermano, M. Multi-Material 3D Printing of Biobased Epoxy Resins. Polymers 2024, 16, 1510. https://doi.org/10.3390/polym16111510
3) Alarcon, R.T.; Bergoglio, M.; Cavalheiro, É.T.G.; Sangermano, M. Thiol-Ene Photopolymerization and 3D Printing of Non-Modified Castor Oil Containing Bio-Based Cellulosic Fillers. Polymers 2025, 17, 587. https://doi.org/10.3390/polym17050587

A2 Conferences attended

1) Polymer Meeting 15 (PM15), Bratislava (Slovakia). (Poster session: Sustainable bio-based UV-cured epoxy vitrimer from castor oil)
2) EUPOC 2023, Dynamic Polymer Networks, Bertinoro (Italy). (Poster session: Sustainable Bio-Based UV-Cured Epoxy Vitrimer from Castor Oil)
3) ESPS 2024, 8th European Symposium of photopolymer science, Stresa (Italy). (Oral presentation: Exploiting 3D Printing For Bioactive Glass Reinforced Scaffolds)
4) 1st SURE-POLY Workshop, Leoben (Austria). (Oral presentation: Biobased epoxy monomer: Photocurable formulation with vitrimeric characteristics and enhanced electrical conductivity)
5) European Polymer Congress EPF 2025, Groningen (Netherlands). (Poster session: UV-Cured bio-based vitrimeric scaffold reinforced with Te-doped bioactive glasses)
6) XXV convegno nazionale, AIM, Napoli (Italy). (Poster session: UV-Cured bio-based scaffold reinforced with bioactive glasses)

7) XVIII edizione Congresso AIMAT25, Ischia (Italy). (Oral presentation: 3D printed polyHIPE scaffolds bioactive glass reinforced)
8) Photopolymerization fundamentals, Boulder (United States of America). (Oral presentation: 3D printed polyHIPE scaffolds bioactive glass reinforced)

A3 Research period abroad

1) Research period in the Polymer Competence Centre Leoben (PCCL) and Montanuniversität Leoben (MUL), Austria, from 11/2022 to 12/2022
2) Research period in Luxinergy GmbH, Leoben, Austria from 9/23 to 11/23
3) Research period in Monash University, Clayton, Australia, from 1/2025 to 5/2025

Bibliography

1. https://www-statista-com.ezproxy.biblio.polito.it/statistics/282732/global-production-of-plastics-since-1950/ Annual Production of Plastics Worldwide from 1950 to 2023.
2. https://www.statista.com/statistics/1535533/global-bioplastic-production-by-type/ Distribution of Bio-Based Plastic Production Worldwide in 2023, by Type.
3. Shen, L.; Worrell, E.; Patel, M. Present and Future Development in Plastics from Biomass. *Biofuels, Bioproducts and Biorefining* 2010, *4*, 25–40, doi:10.1002/bbb.189.
4. Zhu, Y.; Romain, C.; Williams, C.K. Sustainable Polymers from Renewable Resources. *Nature* 2016, *540*, 354–362, doi:10.1038/nature21001.
5. Gandini, A.; Lacerda, T.M. From Monomers to Polymers from Renewable Resources: Recent Advances. *Prog Polym Sci* 2015, *48*, 1–39, doi:10.1016/j.progpolymsci.2014.11.002.
6. Montarnal, D.; Capelot, M.; Tournilhac, F.; Leibler, L. Silica-Like Malleable Materials from Permanent Organic Networks. *Science (1979)* 2011, *334*, 965–968, doi:10.1126/science.1212648.
7. Altuna, F.I.; Pettarin, V.; Williams, R.J.J. Self-Healable Polymer Networks Based on the Cross-Linking of Epoxidised Soybean Oil by an Aqueous Citric Acid Solution. *Green Chemistry* 2013, *15*, 3360, doi:10.1039/c3gc41384e.
8. Fertier, L.; Koleilat, H.; Stemmelen, M.; Giani, O.; Joly-Duhamel, C.; Lapinte, V.; Robin, J.-J. The Use of Renewable Feedstock in UV-Curable Materials – A New Age for Polymers and Green Chemistry. *Prog Polym Sci* 2013, *38*, 932–962, doi:10.1016/j.progpolymsci.2012.12.002.
9. Bowman, C.N.; Kloxin, C.J. Toward an Enhanced Understanding and Implementation of Photopolymerization Reactions. *AIChE Journal* 2008, *54*, 2775–2795, doi:10.1002/aic.11678.
10. Yagci, Y.; Jockusch, S.; Turro, N.J. Photoinitiated Polymerization: Advances, Challenges, and Opportunities. *Macromolecules* 2010, *43*, 6245–6260, doi:10.1021/ma1007545.
11. Baret, V.; Gandini, A.; Rousset, E. Photodimerization of Heteroarylene-Vinylenes. *J Photochem Photobiol A Chem* 1997, *103*, 169–175, doi:10.1016/S1010-6030(96)04525-X.

12. Peters, M.V.; Stoll, R.S.; Kühn, A.; Hecht, S. Photoswitching of Basicity. *Angewandte Chemie International Edition* 2008, *47*, 5968–5972, doi:10.1002/anie.200802050.
13. Krompiec, S.; Bujak, P.; Malarz, J.; Krompiec, M.; Skórka, Ł.; Pluta, T.; Danikiewicz, W.; Kania, M.; Kusz, J. An Isomerization—1,3-Dipolar Cycloaddition Tandem Reaction towards the Synthesis of 3-Aryl-4-Methyl-5-O-Substituted Isoxazolines from O-Allyl Compounds. *Tetrahedron* 2012, *68*, 6018–6031, doi:10.1016/j.tet.2012.05.027.
14. Ding, L.; Chen, Y.F.; Zhong, Z.; Lu, F.; Du, Y.; Liu, L.; Huang, Y. Preparation of the Flexible Soybean Oil-based Material via [2 + 2] Cycloaddition Photo-polymerization. *J Appl Polym Sci* 2021, *138*, doi:10.1002/app.49925.
15. Kiskan, B.; Yagci, Y. Thermally Curable Benzoxazine Monomer with a Photodimerizable Coumarin Group. *J Polym Sci A Polym Chem* 2007, *45*, 1670–1676, doi:10.1002/pola.21934.
16. Decker, C. Kinetic Study and New Applications of UV Radiation Curing. *Macromol Rapid Commun* 2002, *23*, 1067–1093, doi:10.1002/marc.200290014.
17. Crivello, J. V.; Lam, J.H.W. Diaryliodonium Salts. A New Class of Photoinitiators for Cationic Polymerization. *Macromolecules* 1977, *10*, 1307–1315, doi:10.1021/ma60060a028.
18. Joseph R. Lakowicz *Principles of Fluorescence Spectroscopy*; Third Edition.; Springer: Baltimore, Maryland, USA, 2006;
19. Tripathy, R.; Crivello, J. V.; Faust, R. Photoinitiated Polymerization of Acrylate, Methacrylate, and Vinyl Ether End-functional Polyisobutylene Macromonomers. *J Polym Sci A Polym Chem* 2013, *51*, 305–317, doi:10.1002/pola.26379.
20. Tehfe, M.; Louradour, F.; Lalevée, J.; Fouassier, J.-P. Photopolymerization Reactions: On the Way to a Green and Sustainable Chemistry. *Applied Sciences* 2013, *3*, 490–514, doi:10.3390/app3020490.
21. Khudyakov, I. V. Fast Photopolymerization of Acrylate Coatings: Achievements and Problems. *Prog Org Coat* 2018, *121*, 151–159, doi:10.1016/j.porgcoat.2018.04.030.
22. Tiwari, A., P.A. *Photocured Materials*; 2014; Vol. ISBN 178262001X;
23. Decker, C.; Elzaouk, B.; Decker, D. Kinetic Study of Ultrafast Photopolymerization Reactions. *Journal of Macromolecular Science, Part A* 1996, *33*, 173–190, doi:10.1080/10601329608010861.

24. Fındık, V.; Degirmenci, I.; Çatak, Ş.; Aviyente, V. Theoretical Investigation of Thiol-Ene Click Reactions: A DFT Perspective. *Eur Polym J* 2019, *110*, 211–220, doi:10.1016/j.eurpolymj.2018.11.030.
25. Hoyle, C.E.; Lee, T.Y.; Roper, T. Thiol–Enes: Chemistry of the Past with Promise for the Future. *J Polym Sci A Polym Chem* 2004, *42*, 5301–5338, doi:10.1002/pola.20366.
26. Lowe, A.B. Thiol-Ene "Click" Reactions and Recent Applications in Polymer and Materials Synthesis. *Polym. Chem.* 2010, *1*, 17–36, doi:10.1039/B9PY00216B.
27. Cramer, N.B.; Reddy, S.K.; O'Brien, A.K.; Bowman, C.N. Thiol−Ene Photopolymerization Mechanism and Rate Limiting Step Changes for Various Vinyl Functional Group Chemistries. *Macromolecules* 2003, *36*, 7964–7969, doi:10.1021/ma034667s.
28. Decker, C. The Use of UV Irradiation in Polymerization. *Polym Int* 1998, *45*, 133–141, doi:10.1002/(SICI)1097-0126(199802)45:2<133::AID-PI969>3.0.CO;2-F.
29. Crivello, J. V. Cationic Polymerization — Iodonium and Sulfonium Salt Photoinitiators. In *Initiators — Poly-Reactions — Optical Activity*; Springer-Verlag: Berlin/Heidelberg; pp. 1–48.
30. Crivello, J. V. The Discovery and Development of Onium Salt Cationic Photoinitiators. *J Polym Sci A Polym Chem* 1999, *37*, 4241–4254, doi:10.1002/(SICI)1099-0518(19991201)37:23<4241::AID-POLA1>3.0.CO;2-R.
31. Decker, C.; Moussa, K. Kinetic Study of the Cationic Photopolymerization of Epoxy Monomers. *J Polym Sci A Polym Chem* 1990, *28*, 3429–3443, doi:10.1002/pola.1990.080281220.
32. Crivello, J. V.; Narayan, R. Novel Epoxynorbornane Monomers. 2. Cationic Photopolymerization. *Macromolecules* 1996, *29*, 439–445, doi:10.1021/ma951056u.
33. Yagci, Y.; Yildirim, S.; Onen, A. A Novel Bifunctional Addition-Fragmentation Agent for Photoinitiated Cationic Polymerization. *Macromol Chem Phys* 2001, *202*, 527–531, doi:10.1002/1521-3935(20010201)202:4<527::AID-MACP527>3.0.CO;2-2.
34. Onen, A.; Yagci, Y. The Effect of the Heteroatom Moiety of Allylic Salts on the Addition Fragmentation Initiation of Cationic Polymerization. *Macromol Chem Phys* 2001, *202*, 1950–1954, doi:10.1002/1521-3935(20010601)202:9<1950::AID-MACP1950>3.0.CO;2-U.

35. Gomurashvili, Z.; Crivello, J. V. Monomeric and Polymeric Phenothiazine Photosensitizers for Photoinitiated Cationic Polymerization. *Macromolecules* 2002, *35*, 2962–2969, doi:10.1021/ma0119272.
36. Ngo, T.D.; Kashani, A.; Imbalzano, G.; Nguyen, K.T.Q.; Hui, D. Additive Manufacturing (3D Printing): A Review of Materials, Methods, Applications and Challenges. *Compos B Eng* 2018, *143*, 172–196, doi:10.1016/j.compositesb.2018.02.012.
37. Chu, H.; Yang, W.; Sun, L.; Cai, S.; Yang, R.; Liang, W.; Yu, H.; Liu, L. 4D Printing: A Review on Recent Progresses. *Micromachines (Basel)* 2020, *11*, 796, doi:10.3390/mi11090796.
38. Al Rashid, A.; Khan, S.A.; G. Al-Ghamdi, S.; Koç, M. Additive Manufacturing: Technology, Applications, Markets, and Opportunities for the Built Environment. *Autom Constr* 2020, *118*, 103268, doi:10.1016/j.autcon.2020.103268.
39. Bernal, P.N.; Delrot, P.; Loterie, D.; Li, Y.; Malda, J.; Moser, C.; Levato, R. Volumetric Bioprinting of Complex Living-Tissue Constructs within Seconds. *Advanced Materials* 2019, *31*, doi:10.1002/adma.201904209.
40. Yilmaz, B.; Al Rashid, A.; Mou, Y.A.; Evis, Z.; Koç, M. Bioprinting: A Review of Processes, Materials and Applications. *Bioprinting* 2021, *23*, e00148, doi:10.1016/j.bprint.2021.e00148.
41. Manapat, J.Z.; Chen, Q.; Ye, P.; Advincula, R.C. 3D Printing of Polymer Nanocomposites via Stereolithography. *Macromol Mater Eng* 2017, *302*, doi:10.1002/mame.201600553.
42. Ho, C.M.B.; Ng, S.H.; Li, K.H.H.; Yoon, Y.-J. 3D Printed Microfluidics for Biological Applications. *Lab Chip* 2015, *15*, 3627–3637, doi:10.1039/C5LC00685F.
43. Bernal, P.N.; Delrot, P.; Loterie, D.; Li, Y.; Malda, J.; Moser, C.; Levato, R. Volumetric Bioprinting of Complex Living-Tissue Constructs within Seconds. *Advanced Materials* 2019, *31*, doi:10.1002/adma.201904209.
44. Kelly, B.E.; Bhattacharya, I.; Heidari, H.; Shusteff, M.; Spadaccini, C.M.; Taylor, H.K. Volumetric Additive Manufacturing via Tomographic Reconstruction. *Science (1979)* 2019, *363*, 1075–1079, doi:10.1126/science.aau7114.
45. Karakurt, I.; Lin, L. 3D Printing Technologies: Techniques, Materials, and Post-Processing. *Curr Opin Chem Eng* 2020, *28*, 134–143, doi:10.1016/j.coche.2020.04.001.
46. Monneret, S.; Loubere, V.; Corbel, S. Microstereolithography Using a Dynamic Mask Generator and a Noncoherent Visible Light Source.;

Courtois, B., Crary, S.B., Ehrfeld, W., Fujita, H., Karam, J.M., Markus, K.W., Eds.; March 10 1999; p. 553.
47. Sun, C.; Fang, N.; Wu, D.M.; Zhang, X. Projection Micro-Stereolithography Using Digital Micro-Mirror Dynamic Mask. *Sens Actuators A Phys* 2005, *121*, 113–120, doi:10.1016/j.sna.2004.12.011.
48. Mou, Y.A.; Koc, M. Dimensional Capability of Selected 3DP Technologies. *Rapid Prototyp J* 2019, *25*, 915–924, doi:10.1108/RPJ-03-2019-0061.
49. Xie, R.; Li, D.; Chao, S. An Inexpensive Stereolithography Technology with High Power UV-LED Light. *Rapid Prototyp J* 2011, *17*, 441–450, doi:10.1108/13552541111184170.
50. Kaufmann, B.K.; Rudolph, M.; Pechtl, M.; Wildenburg, G.; Hayden, O.; Clausen-Schaumann, H.; Sudhop, S. MSLAb – An Open-Source Masked Stereolithography (MSLA) Bioprinter. *HardwareX* 2024, *19*, e00543, doi:10.1016/J.OHX.2024.E00543.
51. Orozco-Osorio, Y.A.; Gaita-Anturi, A.V.; Ossa-Orozco, C.P.; Arias-Acevedo, M.; Uribe, D.; Paucar, C.; Vasquez, A.F.; Saldarriaga, W.; Ramirez, J.G.; Lopera, A.; et al. Utilization of Additive Manufacturing Techniques for the Development of a Novel Scaffolds with Magnetic Properties for Potential Application in Enhanced Bone Regeneration. *Small* 2024, *20*, doi:10.1002/smll.202402419.
52. Mustapha, R.; Rahmat, A.R.; Abdul Majid, R.; Mustapha, S.N.H. Vegetable Oil-Based Epoxy Resins and Their Composites with Bio-Based Hardener: A Short Review. *Polymer-Plastics Technology and Materials* 2019, *58*, 1311–1326, doi:10.1080/25740881.2018.1563119.
53. Miao, S.; Wang, P.; Su, Z.; Zhang, S. Vegetable-Oil-Based Polymers as Future Polymeric Biomaterials. *Acta Biomater* 2014, *10*, 1692–1704, doi:10.1016/j.actbio.2013.08.040.
54. Mondal, D.; Srinivasan, A.; Comeau, P.; Toh, Y.-C.; Willett, T.L. Acrylated Epoxidized Soybean Oil/Hydroxyapatite-Based Nanocomposite Scaffolds Prepared by Additive Manufacturing for Bone Tissue Engineering. *Materials Science and Engineering: C* 2021, *118*, 111400, doi:https://doi.org/10.1016/j.msec.2020.111400.
55. Miao, S.; Zhu, W.; Castro, N.J.; Nowicki, M.; Zhou, X.; Cui, H.; Fisher, J.P.; Zhang, L.G. 4D Printing Smart Biomedical Scaffolds with Novel Soybean Oil Epoxidized Acrylate. *Sci Rep* 2016, *6*, 27226, doi:10.1038/srep27226.
56. Barkane, A.; Platnieks, O.; Jurinovs, M.; Gaidukovs, S. Thermal Stability of UV-Cured Vegetable Oil Epoxidized Acrylate-Based Polymer System for

3D Printing Application. *Polym Degrad Stab* 2020, *181*, 109347, doi:10.1016/j.polymdegradstab.2020.109347.

57. Barkane, A.; Jurinovs, M.; Briede, S.; Platnieks, O.; Onufrijevs, P.; Zelca, Z.; Gaidukovs, S. Biobased Resin for Sustainable Stereolithography: 3D Printed Vegetable Oil Acrylate Reinforced with Ultra-Low Content of Nanocellulose for Fossil Resin Substitution. *3D Print Addit Manuf* 2023, *10*, 1272–1286, doi:10.1089/3dp.2021.0294.
58. Barkane, A.; Platnieks, O.; Jurinovs, M.; Kasetaite, S.; Ostrauskaite, J.; Gaidukovs, S.; Habibi, Y. UV-Light Curing of 3D Printing Inks from Vegetable Oils for Stereolithography. *Polymers (Basel)* 2021, *13*, 1195, doi:10.3390/polym13081195.
59. Vazquez-Martel, C.; Becker, L.; Liebig, W. V.; Elsner, P.; Blasco, E. Vegetable Oils as Sustainable Inks for Additive Manufacturing: A Comparative Study. *ACS Sustain Chem Eng* 2021, *9*, 16840–16848, doi:10.1021/acssuschemeng.1c06784.
60. Noè, C.; Cosola, A.; Tonda-Turo, C.; Sesana, R.; Delprete, C.; Chiappone, A.; Hakkarainen, M.; Sangermano, M. DLP-Printable Fully Biobased Soybean Oil Composites. *Polymer (Guildf)* 2022, *247*, 124779, doi:10.1016/j.polymer.2022.124779.
61. Wang, D.; Xiong, Y.; Zhang, B.; Zhang, Y.-F.; Rosen, D.; Ge, Q. Design Framework for Mechanically Tunable Soft Biomaterial Composites Enhanced by Modified Horseshoe Lattice Structures. *Soft Matter* 2020, *16*, 1473–1484, doi:10.1039/C9SM02119A.
62. Kloxin, C.J.; Scott, T.F.; Adzima, B.J.; Bowman, C.N. Covalent Adaptable Networks (CANs): A Unique Paradigm in Cross-Linked Polymers. *Macromolecules* 2010, *43*, 2643–2653, doi:10.1021/ma902596s.
63. Bergoglio, M.; Reisinger, D.; Schlögl, S.; Griesser, T.; Sangermano, M. Sustainable Bio-Based UV-Cured Epoxy Vitrimer from Castor Oil. *Polymers (Basel)* 2023, *15*, doi:10.3390/polym15041024.
64. Montarnal, D.; Capelot, M.; Tournilhac, F.; Leibler, L. Silica-Like Malleable Materials from Permanent Organic Networks. *Science (1979)* 2011, *334*, 965–968, doi:10.1126/science.1212648.
65. Dutta, K.; Karak, N. Exchangeable Disulfide Bond Containing Highly Flexible Epoxy Vitrimers with Shape-memory, Self-healing, and <scp>UV</Scp> Shielding Attributes. *Polym Adv Technol* 2024, *35*, doi:10.1002/pat.6286.
66. Vilanova-Pérez, A.; Moradi, S.; Konuray, O.; Ramis, X.; Roig, A.; Fernández-Francos, X. Harnessing Disulfide and Transesterification Bond

Exchange Reactions for Recyclable and Reprocessable 3D-Printed Vitrimers. *React Funct Polym* 2024, *195*, 105825, doi:10.1016/J.REACTFUNCTPOLYM.2023.105825.

67. Vilanova-Pérez, A.; Moradi, S.; Konuray, O.; Ramis, X.; Roig, A.; Fernández-Francos, X. Harnessing Disulfide and Transesterification Bond Exchange Reactions for Recyclable and Reprocessable 3D-Printed Vitrimers. *React Funct Polym* 2024, *195*, 105825, doi:10.1016/J.REACTFUNCTPOLYM.2023.105825.
68. Wang, F.; Lu, X.; Xin, Z. Self-Healing Biobased Polybenzoxazine Vitrimers for Anticorrosion Application. *Prog Org Coat* 2025, *203*, 109168, doi:10.1016/J.PORGCOAT.2025.109168.
69. Dutta, K.; Karak, N. Exchangeable Disulfide Bond Containing Highly Flexible Epoxy Vitrimers with Shape-memory, Self-healing, and <scp>UV</Scp> Shielding Attributes. *Polym Adv Technol* 2024, *35*, doi:10.1002/pat.6286.
70. Sölle, B.; Schmallegger, M.; Schlögl, S.; Rossegger, E. Wavelength-Dependent Dynamic Behavior in Thiol–Ene Networks Based on Disulfide Exchange. *J Am Chem Soc* 2024, *146*, 34152–34157, doi:10.1021/jacs.4c13735.
71. Subramaniyan, S.; Bergoglio, M.; Sangermano, M.; Hakkarainen, M. Vanillin-Derived Thermally Reprocessable and Chemically Recyclable Schiff-Base Epoxy Thermosets. *Global Challenges* 2023, *n/a*, 2200234, doi:https://doi.org/10.1002/gch2.202200234.
72. Zhu, Z.; West, S.; Chen, H.; Lai, G.-H.; Uenuma, S.; Ito, K.; Kotaki, M.; Sue, H.-J. Mechanically Interlocked Vitrimer Based on Polybenzoxazine and Polyrotaxane. *ACS Appl Polym Mater* 2023, *5*, 3971–3978, doi:10.1021/acsapm.3c00196.
73. Tripathi, S.; H., S.; Bose, S. A Designer Schiff Based Motif Offered Dual Dynamic Exchangeable Bonds, Faster Curing and Closed-loop Circularity in Epoxy Vitrimers. *SPE Polymers* 2024, *5*, 136–150, doi:10.1002/pls2.10114.
74. Miao, P.; Leng, X.; Liu, J.; Song, G.; He, M.; Li, Y. Regulating the Dynamic Behaviors of Transcarbamoylation-Based Vitrimers via Mono-Variation in Density of Exchangeable Hydroxyl. *Macromolecules* 2022, *55*, 4956–4966, doi:10.1021/acs.macromol.2c00127.
75. Hu, J.; Gao, Y.; Hang, G.; Wang, H.; Zhang, T.; Zheng, S. Crosslinking of Polyethylene with Polysilsesquioxane via Carbamate Linkages: Synthesis, Shape Recovery, and Reprocessing Properties. *Journal of Polymer Science* 2024, *62*, 2945–2960, doi:10.1002/pol.20240175.

76. Bautista-Anguís, D.; Reiner, L.; Röper, F.; Maar, S.; Wolfahrt, M.; Wolfberger, A.; Schlögl, S. Synthesis and Characterization of Rebondable Polyurethane Adhesives Relying on Thermo-Activated Transcarbamoylation. *Polymers (Basel)* 2024, *16*, 2799, doi:10.3390/polym16192799.
77. Schwarzer, L.; Agarwal, S. Adaptable Polyurethane Networks Containing Tertiary Amines as Intrinsic Bond Exchange Catalyst. *Macromol Chem Phys* 2024, *225*, doi:10.1002/macp.202400072.
78. Telatin, T.; De la Flor, S.; Montané, X.; Serra, À. Chemically Degradable Vitrimers Based on Divanillin Imine Diepoxy Monomer and Aliphatic Diamines for Enhanced Carbon Fiber Composite Applications. *Polymers (Basel)* 2024, *16*, 2754, doi:10.3390/polym16192754.
79. Tran, H.T.T.; Radjef, R.; Nikzad, M.; Bjekovic, R.; Fox, B. A Vanillin-Based Vitrimer Matrix for Recyclable and Sustainable Carbon Fibre-Reinforced Composites. *J Clean Prod* 2024, *483*, 144289, doi:10.1016/J.JCLEPRO.2024.144289.
80. Vilanova-Pérez, A.; Surós, M.; Serra, À.; De la Flor, S.; Roig, A. Custom-Shaped Malleable, Recyclable and Reversible Structural Adhesives Based on Vanillin Polyimine Vitrimers. *React Funct Polym* 2025, *206*, 106109, doi:10.1016/J.REACTFUNCTPOLYM.2024.106109.
81. Schütz, P.; Weerathaworn, S.; Jürgensen, C.; Hankiewicz, B.; Abetz, V. Nanocomposites from Au-Doped Vinylogous Urethane Vitrimers Based on Different Block Copolymers and Their Recyclability in Combination with Plasmonic Heating. *Macromol Rapid Commun* 2025, doi:10.1002/marc.202401027.
82. Lucherelli, M.A.; Duval, A.; Avérous, L. Biobased Vitrimers: Towards Sustainable and Adaptable Performing Polymer Materials. *Prog Polym Sci* 2022, *127*, 101515, doi:https://doi.org/10.1016/j.progpolymsci.2022.101515.
83. Zhao, B.; Mei, H.; Hang, G.; Li, L.; Zheng, S. Shape Recovery and Reprocessable Polyurethanes Crosslinked with Double Decker Silsesquioxane via Diels-Alder Reaction. *Polymer (Guildf)* 2021, *230*, 124042, doi:10.1016/J.POLYMER.2021.124042.
84. Orozco, F.; Li, J.; Ezekiel, U.; Niyazov, Z.; Floyd, L.; Lima, G.M.R.; Winkelman, J.G.M.; Moreno-Villoslada, I.; Picchioni, F.; Bose, R.K. Diels-Alder-Based Thermo-Reversibly Crosslinked Polymers: Interplay of Crosslinking Density, Network Mobility, Kinetics and Stereoisomerism. *Eur Polym J* 2020, *135*, 109882, doi:10.1016/J.EURPOLYMJ.2020.109882.

85. Gao, L.; Wang, H.; Yao, X.; Zheng, Z.; Wang, L.; Wang, Z.; Wang, Y.; Zhang, B.; Jing, X.; Wu, J. High-Performance Epoxy Vitrimer from Commercial Epoxy-Anhydride with Reprocessable and Chemical Degradable Properties. *Front Mater* 2025, *12*, doi:10.3389/fmats.2025.1552713.
86. Santiago, D.; Guzmán, D.; Padilla, J.; Verdugo, P.; De la Flor, S.; Serra, À. Recyclable and Reprocessable Epoxy Vitrimer Adhesives. *ACS Appl Polym Mater* 2023, *5*, 2006–2015, doi:10.1021/acsapm.2c02063.
87. Vidil, T.; Llevot, A. Fully Biobased Vitrimers: Future Direction toward Sustainable Cross-Linked Polymers. *Macromol Chem Phys* 2022, *223*, doi:10.1002/macp.202100494.
88. Chong, K.L.; Lai, J.C.; Rahman, R.A.; Adrus, N.; Al-Saffar, Z.H.; Hassan, A.; Lim, T.H.; Wahit, M.U. A Review on Recent Approaches to Sustainable Bio-Based Epoxy Vitrimer from Epoxidized Vegetable Oils. *Ind Crops Prod* 2022, *189*, 115857, doi:10.1016/j.indcrop.2022.115857.
89. Shaukat, U.; Sölle, B.; Rossegger, E.; Rana, S.; Schlögl, S. Vat Photopolymerization 3D-Printing of Dynamic Thiol-Acrylate Photopolymers Using Bio-Derived Building Blocks. *Polymers (Basel)* 2022, *14*, 5377, doi:10.3390/polym14245377.
90. Zhang, Y. hong; Zhai, M. jiao; Shi, L.; Lei, Q. yang; Zhang, S. tong; Zhang, L.; Lyu, B.; Zhao, S. hua; Ma, J. zhong; Thakur, V.K. Sustainable Castor Oil-Based Vitrimers: Towards New Materials with Reprocessability, Self-Healing, Degradable and UV-Blocking Characteristics. *Ind Crops Prod* 2023, *193*, 116210, doi:10.1016/J.INDCROP.2022.116210.
91. Chauke, N.P.; Mukaya, H.E.; Nkazi, D.B. Chemical Modifications of Castor Oil: A Review. *Sci Prog* 2019, *102*, 199–217, doi:10.1177/0036850419859118.
92. Yuan, H.; Dong, Z.; He, J.; Wang, Y.; Zhang, H. Surface Characterization of Sulfated Zirconia and Its Catalytic Activity for Epoxidation Reaction of Castor Oil. *Chem Eng Commun* 2019, *206*, 1618–1627, doi:10.1080/00986445.2018.1560274.
93. Liu, C.; Wang, C.; Hu, Y.; Zhang, F.; Shang, Q.; Lei, W.; Zhou, Y.; Cai, Z. Castor Oil-Based Polyfunctional Acrylate Monomers: Synthesis and Utilization in UV-Curable Materials. *Prog Org Coat* 2018, *121*, 236–246, doi:10.1016/J.PORGCOAT.2018.04.020.
94. Li, M.; Xia, J.; Mao, W.; Yang, X.; Xu, L.; Huang, K.; Li, S. Preparation and Properties of Castor Oil-Based Dual Cross-Linked Polymer Networks with

Polyurethane and Polyoxazolidinone Structures. *ACS Sustain Chem Eng* 2017, *5*, 6883–6893, doi:10.1021/acssuschemeng.7b01103.

95. CHAKRAPANI, S.; CRIVELLO*, J. V. Synthesis and Photoinitiated Cationic Polymerization Of Epoxidized Castor Oil and Its Derivatives. *Journal of Macromolecular Science, Part A* 1998, *35*, 1–20, doi:10.1080/10601329808001959.
96. Pradhan, S.; Rajamani, S.; Agrawal, G.; Dash, M.; Samal, S.K. NMR, FT-IR and Raman Characterization of Biomaterials. In *Characterization of Polymeric Biomaterials*; Elsevier, 2017; pp. 147–173.
97. Kazarian, S.G.; Chan, K.L.A. FTIR Imaging of Polymeric Materials. In *Polymer Morphology*; Wiley, 2016; pp. 118–130.
98. Schick, C. Calorimetry. In *Polymer Science: A Comprehensive Reference*; Elsevier, 2012; pp. 793–823.
99. Gahleitner, M.; Grein, C.; Bernreitner, K.; Knogler, B.; Hebesberger, E. The Use of DMTA for Predicting Standard Mechanical Properties of Developmental Polyolefins. *J Therm Anal Calorim* 2009, *98*, 623–628, doi:10.1007/s10973-009-0506-5.
100. Wetton, R.E.; Marsh, R.D.L.; Van-de-Velde, J.G. Theory and Application of Dynamic Mechanical Thermal Analysis. *Thermochim Acta* 1991, *175*, 1–11, doi:10.1016/0040-6031(91)80240-J.
101. Saba, N.; Jawaid, M.; Sultan, M.T.H. An Overview of Mechanical and Physical Testing of Composite Materials. *Mechanical and Physical Testing of Biocomposites, Fibre-Reinforced Composites and Hybrid Composites* 2019, 1–12, doi:10.1016/B978-0-08-102292-4.00001-1.
102. Alasfar, R.H.; Ahzi, S.; Barth, N.; Kochkodan, V.; Khraisheh, M.; Koç, M. A Review on the Modeling of the Elastic Modulus and Yield Stress of Polymers and Polymer Nanocomposites: Effect of Temperature, Loading Rate and Porosity. *Polymers (Basel)* 2022, *14*, 360, doi:10.3390/polym14030360.
103. Prime, R.B.; Bair, H.E.; Vyazovkin, S.; Gallagher, P.K.; Riga, A. Thermogravimetric Analysis (TGA). In *Thermal Analysis of Polymers*; Wiley, 2009; pp. 241–317.
104. Bottom, R. Thermogravimetric Analysis. In *Principles and Applications of Thermal Analysis*; Wiley, 2008; pp. 87–118.
105. Pandey, J.C.; Singh, M. Dielectric Polymer Nanocomposites: Past Advances and Future Prospects in Electrical Insulation Perspective. *SPE Polymers* 2021, *2*, 236–256, doi:10.1002/pls2.10059.

106. Capelot, M.; Montarnal, D.; Tournilhac, F.; Leibler, L. Metal-Catalyzed Transesterification for Healing and Assembling of Thermosets. *J Am Chem Soc* 2012, *134*, 7664–7667, doi:10.1021/ja302894k.
107. Winne, J.M.; Leibler, L.; Du Prez, F.E. Dynamic Covalent Chemistry in Polymer Networks: A Mechanistic Perspective. *Polym Chem* 2019, *10*, 6091–6108, doi:10.1039/C9PY01260E.
108. Alabiso, W.; Schlögl, S. The Impact of Vitrimers on the Industry of the Future: Chemistry, Properties and Sustainable Forward-Looking Applications. *Polymers (Basel)* 2020, *12*, 1660, doi:10.3390/polym12081660.
109. Wang, H.; Li, J.; Zhang, X.; Ouyang, Z.; Li, Q.; Su, Z.; Wei, G. Synthesis, Characterization and Drug Release Application of Carbon Nanotube-Polymer Nanosphere Composites. *RSC Adv* 2013, *3*, 9304, doi:10.1039/c3ra40997j.
110. Pham, V.G.; Pham, N.T.; Tran, L.D.; Dinh, T.H.; Vrublevsky, I.; Charniakova, K.; Le, H.V. Insight into the Effect of Zinc Oxide Nanoparticles Coated Multi-Walled Carbon Nanotubes (ZnO/MWCNTs) on the Thermal Conductivity of Epoxy Nanocomposite as an Electrical-Insulating Coating. *Journal of the Australian Ceramic Society* 2021, *57*, 1445–1452, doi:10.1007/s41779-021-00646-6.
111. Alemour, B.; Badran, O.; Hassan, M.R. A Review of Using Conductive Composite Materials in Solving Lightening Strike and Ice Accumulation Problems in Aviation. *Journal of Aerospace Technology and Management* 2019, doi:10.5028/jatm.v11.1022.
112. Zhang, Y.; Zhai, M.; Shi, L.; Lei, Q.; Zhang, S.; Zhang, L.; Lyu, B.; Zhao, S.; Ma, J.; Thakur, V.K. Sustainable Castor Oil-Based Vitrimers: Towards New Materials with Reprocessability, Self-Healing, Degradable and UV-Blocking Characteristics. *Ind Crops Prod* 2023, *193*, 116210, doi:10.1016/j.indcrop.2022.116210.
113. Zhang, Y.; Zhang, S.; Zhai, M.; Wei, B.; Lyu, B.; Liu, L. Self-Healing and Recyclable Castor Oil-Based Epoxy Vitrimer Based on Dual Dynamic Bonds of Disulfide and Ester Bonds. *ACS Appl Polym Mater* 2024, *6*, 8399–8408, doi:10.1021/acsapm.4c01208.
114. Zhao, Y.; Zhang, Y.; Bai, X.; Wang, Y.; Li, Y.; Yang, S. Sustainable Epoxy Vitrimer Materials with Imine and Disulfide Bonds Prepared from Epoxidized Soybean Oils. *Ind Crops Prod* 2025, *225*, 120435, doi:10.1016/j.indcrop.2024.120435.

115. Hale, A.; Macosko, C.W.; Bair, H.E. Glass Transition Temperature as a Function of Conversion in Thermosetting Polymers. *Macromolecules* 1991, *24*, 2610–2621, doi:10.1021/ma00009a072.
116. Santiago, D.; Guzmán, D.; Padilla, J.; Verdugo, P.; De la Flor, S.; Serra, À. Recyclable and Reprocessable Epoxy Vitrimer Adhesives. *ACS Appl Polym Mater* 2023, *5*, 2006–2015, doi:10.1021/acsapm.2c02063.
117. Mu, Q.; Wang, L.; Dunn, C.K.; Kuang, X.; Duan, F.; Zhang, Z.; Qi, H.J.; Wang, T. Digital Light Processing 3D Printing of Conductive Complex Structures. *Addit Manuf* 2017, *18*, 74–83, doi:10.1016/j.addma.2017.08.011.
118. Di Mauro, C.; Malburet, S.; Genua, A.; Graillot, A.; Mija, A. Sustainable Series of New Epoxidized Vegetable Oil-Based Thermosets with Chemical Recycling Properties. *Biomacromolecules* 2020, *21*, 3923–3935, doi:10.1021/acs.biomac.0c01059.
119. Lee, C.L.; A. Bakar, B.F.; Chin, K.L.; Chuah Abdullah, L. A Review on the Formulation and Performance of Epoxidized Vegetable Oil-Based Vitrimer: Stoichiometric Calculations, Curing Agent Functionalities and Catalyst Efficiency. *R Soc Open Sci* 2025, *12*, doi:10.1098/rsos.250612.
120. Sangermano, M.; Bergoglio, M.; Schögl, S. Biobased Vitrimeric Epoxy Networks. *Macromol Mater Eng* 2023, doi:10.1002/mame.202300371.
121. Bergoglio, M.; Palazzo, G.; Reisinger, D.; Porcarello, M.; Kortaberria, G.; Schlögl, S.; Sangermano, M. Cationic UV-Curing of Bio-Based Epoxidized Castor Oil Vitrimers with Electrically Conductive Properties. *React Funct Polym* 2024, *200*, 105936, doi:10.1016/j.reactfunctpolym.2024.105936.
122. Kokubo, T.; Kim, H.-M.; Kawashita, M. Novel Bioactive Materials with Different Mechanical Properties. *Biomaterials* 2003, *24*, 2161–2175, doi:https://doi.org/10.1016/S0142-9612(03)00044-9.
123. Motameni, A.; Çardaklı, İ.S.; Gürbüz, R.; Alshemary, A.Z.; Razavi, M.; Farukoğlu, Ö.C. Bioglass-Polymer Composite Scaffolds for Bone Tissue Regeneration: A Review of Current Trends. *International Journal of Polymeric Materials and Polymeric Biomaterials* 2023, 1–20, doi:10.1080/00914037.2023.2186864.
124. KARAGEORGIOU, V.; KAPLAN, D. Porosity of 3D Biomaterial Scaffolds and Osteogenesis. *Biomaterials* 2005, *26*, 5474–5491, doi:10.1016/j.biomaterials.2005.02.002.
125. Freyman, T.M.; Yannas, I.V.; Gibson, L.J. Cellular Materials as Porous Scaffolds for Tissue Engineering. *Prog Mater Sci* 2001, *46*, 273–282, doi:10.1016/S0079-6425(00)00018-9.

126. Deliormanli, A.M.; Ensoylu, M.; ALMisned, G.; Tekin, H.O. Two-Dimensional Molybdenum Disulfide/Polymer-Coated Bioactive Glass Scaffolds for Tissue Engineering: Fabrication, Structural, Mechanical, Bioactivity, and Radiation Interaction Properties. *Ceram Int* 2023, *49*, 22861–22874, doi:10.1016/j.ceramint.2023.04.110.
127. Cao, W.; Hench, L.L. Bioactive Materials. *Ceram Int* 1996, *22*, 493–507, doi:10.1016/0272-8842(95)00126-3.
128. Drago, L.; Toscano, M.; Bottagisio, M. Recent Evidence on Bioactive Glass Antimicrobial and Antibiofilm Activity: A Mini-Review. *Materials* 2018, *11*, 326, doi:10.3390/ma11020326.
129. Rivadeneira, J.; Gorustovich, A. Bioactive Glasses as Delivery Systems for Antimicrobial Agents. *J Appl Microbiol* 2017, *122*, 1424–1437, doi:10.1111/jam.13393.
130. Sergi, R.; Bellucci, D.; Cannillo, V. A Review of Bioactive Glass/Natural Polymer Composites: State of the Art. *Materials* 2020, *13*, 5560, doi:10.3390/ma13235560.
131. Zhang, Y.; Hu, M.; Zhang, W.; Zhang, X. Construction of Tellurium-Doped Mesoporous Bioactive Glass Nanoparticles for Bone Cancer Therapy by Promoting ROS-Mediated Apoptosis and Antibacterial Activity. *J Colloid Interface Sci* 2022, *610*, 719–730, doi:10.1016/j.jcis.2021.11.122.
132. Shakibaie, M.; Adeli-Sardou, M.; Mohammadi-Khorsand, T.; ZeydabadiNejad, M.; Amirafzali, E.; Amirpour-Rostami, S.; Ameri, A.; Forootanfar, H. Antimicrobial and Antioxidant Activity of the Biologically Synthesized Tellurium Nanorods; A Preliminary In Vitro Study. *Iran J Biotechnol* 2017, *15*, 268–276, doi:10.15171/ijb.1580.
133. Zhong, C.L.; Qin, B.Y.; Xie, X.Y.; Bai, Y. Antioxidant and Antimicrobial Activity of Tellurium Dioxide Nanoparticles Sols. *Journal of Nano Research* 2013, *25*, 8–15, doi:10.4028/www.scientific.net/JNanoR.25.8.
134. Ba, L.A.; Döring, M.; Jamier, V.; Jacob, C. Tellurium: An Element with Great Biological Potency and Potential. *Org Biomol Chem* 2010, *8*, 4203, doi:10.1039/c0ob00086h.
135. Miola, M.; Massera, J.; Cochis, A.; Kumar, A.; Rimondini, L.; Vernè, E. Tellurium: A New Active Element for Innovative Multifunctional Bioactive Glasses. *Materials Science and Engineering: C* 2021, *123*, 111957, doi:10.1016/j.msec.2021.111957.
136. Cao, B.; Zheng, Y.; Xi, T.; Zhang, C.; Song, W.; Burugapalli, K.; Yang, H.; Ma, Y. Concentration-Dependent Cytotoxicity of Copper Ions on Mouse Fibroblasts in Vitro: Effects of Copper Ion Release from TCu380A vs

TCu220C Intra-Uterine Devices. *Biomed Microdevices* 2012, *14*, 709–720, doi:10.1007/s10544-012-9651-x.
137. Kozon, D.; Zheng, K.; Boccardi, E.; Liu, Y.; Liverani, L.; Boccaccini, A. Synthesis of Monodispersed Ag-Doped Bioactive Glass Nanoparticles via Surface Modification. *Materials* 2016, *9*, 225, doi:10.3390/ma9040225.
138. Marsh, A.C.; Mellott, N.P.; Crimp, M.; Wren, A.; Hammer, N.; Chatzistavrou, X. Ag-Doped Bioactive Glass-Ceramic 3D Scaffolds: Microstructural, Antibacterial, and Biological Properties. *J Eur Ceram Soc* 2021, *41*, 3717–3730, doi:10.1016/j.jeurceramsoc.2021.01.011.
139. Hench, L.L. The Story of Bioglass®. *J Mater Sci Mater Med* 2006, *17*, 967–978, doi:10.1007/s10856-006-0432-z.
140. Jones, J.R. Review of Bioactive Glass: From Hench to Hybrids. *Acta Biomater* 2013, *9*, 4457–4486, doi:10.1016/j.actbio.2012.08.023.
141. Mohammadi Zerankeshi, M.; Bakhshi, R.; Alizadeh, R. Polymer/Metal Composite 3D Porous Bone Tissue Engineering Scaffolds Fabricated by Additive Manufacturing Techniques: A Review. *Bioprinting* 2022, *25*, e00191, doi:10.1016/j.bprint.2022.e00191.
142. Taboas, J.M.; Maddox, R.D.; Krebsbach, P.H.; Hollister, S.J. Indirect Solid Free Form Fabrication of Local and Global Porous, Biomimetic and Composite 3D Polymer-Ceramic Scaffolds. *Biomaterials* 2003, *24*, 181–194, doi:10.1016/S0142-9612(02)00276-4.
143. Venugopal, J.R.; Low, S.; Choon, A.T.; Kumar, A.B.; Ramakrishna, S. Nanobioengineered Electrospun Composite Nanofibers and Osteoblasts for Bone Regeneration. *Artif Organs* 2008, *32*, 388–397, doi:10.1111/j.1525-1594.2008.00557.x.
144. Szymczyk-Ziółkowska, P.; Łabowska, M.B.; Detyna, J.; Michalak, I.; Gruber, P. A Review of Fabrication Polymer Scaffolds for Biomedical Applications Using Additive Manufacturing Techniques. *Biocybern Biomed Eng* 2020, *40*, 624–638, doi:10.1016/j.bbe.2020.01.015.
145. Martelli, A.; Bellucci, D.; Cannillo, V. Additive Manufacturing of Polymer/Bioactive Glass Scaffolds for Regenerative Medicine: A Review. *Polymers (Basel)* 2023, *15*, 2473, doi:10.3390/polym15112473.
146. Hollister, S.J. Porous Scaffold Design for Tissue Engineering. *Nat Mater* 2005, *4*, 518–524, doi:10.1038/nmat1421.
147. O'Brien, F.J. Biomaterials & Scaffolds for Tissue Engineering. *Materials Today* 2011, *14*, 88–95, doi:10.1016/S1369-7021(11)70058-X.

148. Ratner, B.D.; Bryant, S.J. Biomaterials: Where We Have Been and Where We Are Going. *Annu Rev Biomed Eng* 2004, *6*, 41–75, doi:10.1146/annurev.bioeng.6.040803.140027.
149. Hutmacher, D.W. Scaffolds in Tissue Engineering Bone and Cartilage. *Biomaterials* 2000, *21*, 2529–2543, doi:10.1016/S0142-9612(00)00121-6.
150. Langer, R.; Vacanti, J.P. Tissue Engineering. *Science (1979)* 1993, *260*, 920–926, doi:10.1126/science.8493529.
151. Kroeze, R.J.; Helder, M.N.; Govaert, L.E.; Smit, T.H. Biodegradable Polymers in Bone Tissue Engineering. *Materials* 2009, *2*, 833–856, doi:10.3390/ma2030833.
152. Guo, B.; Ma, P.X. Synthetic Biodegradable Functional Polymers for Tissue Engineering: A Brief Review. *Sci China Chem* 2014, *57*, 490–500, doi:10.1007/s11426-014-5086-y.
153. Iqbal, N.; Khan, A.S.; Asif, A.; Yar, M.; Haycock, J.W.; Rehman, I.U. Recent Concepts in Biodegradable Polymers for Tissue Engineering Paradigms: A Critical Review. *International Materials Reviews* 2019, *64*, 91–126, doi:10.1080/09506608.2018.1460943.
154. Martina, M.; Hutmacher, D.W. Biodegradable Polymers Applied in Tissue Engineering Research: A Review. *Polym Int* 2007, *56*, 145–157, doi:10.1002/pi.2108.
155. Eglin, D.; Maalheem, S.; Livage, J.; Coradin, T. In Vitro Apatite Forming Ability of Type I Collagen Hydrogels Containing Bioactive Glass and Silica Sol-Gel Particles. *J Mater Sci Mater Med* 2006, *17*, 161–167, doi:10.1007/s10856-006-6820-6.
156. Demirtaş, T.T.; Irmak, G.; Gümüşderelioğlu, M. A Bioprintable Form of Chitosan Hydrogel for Bone Tissue Engineering. *Biofabrication* 2017, *9*, 035003, doi:10.1088/1758-5090/aa7b1d.
157. Aldhaher, A.; Shahabipour, F.; Shaito, A.; Al-Assaf, S.; Elnour, A.A.M.; Sallam, E.B.; Teimourtash, S.; Elfadil, A.A. 3D Hydrogel/ Bioactive Glass Scaffolds in Bone Tissue Engineering: Status and Future Opportunities. *Heliyon* 2023, *9*, e17050, doi:10.1016/j.heliyon.2023.e17050.
158. Roy, I.; Gupta, M.N. Smart Polymeric Materials. *Chem Biol* 2003, *10*, 1161–1171, doi:10.1016/j.chembiol.2003.12.004.
159. Chelu, M.; Popa, M.; Calderón Moreno, J.M. Applications of Hydrogels in Emergency Therapy. *Gels* 2025, *11*, 234, doi:10.3390/gels11040234.
160. Phattanee, N.; Meesane, J.; Kwanyuang, A.; Srifa, P.; Churuangsuk, C.; Juncheed, K. An Overview of the Biomaterials Used in Hydrogel Fabrication

for Chronic Wound Healing Applications. *Trends in Sciences* 2025, *22*, 9392, doi:10.48048/tis.2025.9392.
161. Calderón Moreno, J.M.; Chelu, M.; Popa, M. Eco-Friendly Conductive Hydrogels: Towards Green Wearable Electronics. *Gels* 2025, *11*, 220, doi:10.3390/gels11040220.
162. Harish Prashanth, K.V.; Tharanathan, R.N. Chitin/Chitosan: Modifications and Their Unlimited Application Potential—an Overview. *Trends Food Sci Technol* 2007, *18*, 117–131, doi:10.1016/j.tifs.2006.10.022.
163. El Knidri, H.; Belaabed, R.; Addaou, A.; Laajeb, A.; Lahsini, A. Extraction, Chemical Modification and Characterization of Chitin and Chitosan. *Int J Biol Macromol* 2018, *120*, 1181–1189, doi:10.1016/j.ijbiomac.2018.08.139.
164. Berroci, M.; Vallejo, C.; Lizundia, E. Environmental Impact Assessment of Chitin Nanofibril and Nanocrystal Isolation from Fungi, Shrimp Shells, and Crab Shells. *ACS Sustain Chem Eng* 2022, *10*, 14280–14293, doi:10.1021/acssuschemeng.2c04417.
165. Sesia, R.; Ferraris, S.; Sangermano, M.; Spriano, S. UV-Cured Chitosan-Based Hydrogels Strengthened by Tannic Acid for the Removal of Copper Ions from Water. *Polymers (Basel)* 2022, *14*, 4645, doi:10.3390/polym14214645.
166. Baggio, A.; Doan, H.N.; Vo, P.P.; Kinashi, K.; Sakai, W.; Tsutsumi, N.; Fuse, Y.; Sangermano, M. Chitosan-Functionalized Recycled Polyethylene Terephthalate Nanofibrous Membrane for Sustainable On-Demand Oil-Water Separation. *Global Challenges* 2021, *5*, doi:10.1002/gch2.202000107.
167. Noè, C.; Zanon, M.; Arencibia, A.; López-Muñoz, M.-J.; Fernández de Paz, N.; Calza, P.; Sangermano, M. UV-Cured Chitosan and Gelatin Hydrogels for the Removal of As(V) and Pb(II) from Water. *Polymers (Basel)* 2022, *14*, 1268, doi:10.3390/polym14061268.
168. Silverstein, M.S. PolyHIPEs: Recent Advances in Emulsion-Templated Porous Polymers. *Prog Polym Sci* 2014, *39*, 199–234, doi:10.1016/J.PROGPOLYMSCI.2013.07.003.
169. Stubenrauch, C.; Menner, A.; Bismarck, A.; Drenckhan, W. Emulsion and Foam Templating—Promising Routes to Tailor-Made Porous Polymers. *Angewandte Chemie International Edition* 2018, *57*, 10024–10032, doi:10.1002/anie.201801466.
170. Zhang, T.; Sanguramath, R.A.; Israel, S.; Silverstein, M.S. Emulsion Templating: Porous Polymers and Beyond. *Macromolecules* 2019, *52*, 5445–5479, doi:10.1021/acs.macromol.8b02576.

171. Foudazi, R. HIPEs to PolyHIPEs. *React Funct Polym* 2021, *164*, 104917, doi:10.1016/j.reactfunctpolym.2021.104917.
172. Bergoglio, M.; Kriehuber, M.; Sölle, B.; Rossegger, E.; Schlögl, S.; Najmi, Z.; Cochis, A.; Ferla, F.; Miola, M.; Vernè, E.; et al. 3D-Printed Acrylated Soybean Oil Scaffolds with Vitrimeric Properties Reinforced by Tellurium-Doped Bioactive Glass. *Polymers (Basel)* 2024, *16*, 3614, doi:10.3390/polym16243614.
173. Sölle, B.; Shaukat, U.; Rossegger, E.; Schlögl, S. Synthesis and Characterization of Bio-Based Transesterification Catalysts for Green 3D-Printable Dynamic Photopolymers. *Polym Chem* 2023, *14*, 4994–5003, doi:10.1039/D3PY00989K.
174. Shaukat, U.; Sölle, B.; Rossegger, E.; Rana, S.; Schlögl, S. Vat Photopolymerization 3D-Printing of Dynamic Thiol-Acrylate Photopolymers Using Bio-Derived Building Blocks. *Polymers (Basel)* 2022, *14*, 5377, doi:10.3390/polym14245377.
175. El-Rashidy, A.A.; Waly, G.; Gad, A.; Hashem, A.A.; Balasubramanian, P.; Kaya, S.; Boccaccini, A.R.; Sami, I. Preparation and in Vitro Characterization of Silver-Doped Bioactive Glass Nanoparticles Fabricated Using a Sol-Gel Process and Modified Stöber Method. *J Non Cryst Solids* 2018, *483*, 26–36, doi:10.1016/j.jnoncrysol.2017.12.044.
176. Kokubo, T.; Takadama, H. How Useful Is SBF in Predicting in Vivo Bone Bioactivity? *Biomaterials* 2006, *27*, 2907–2915, doi:https://doi.org/10.1016/j.biomaterials.2006.01.017.
177. Huang, C.; Shi, S.; Qin, M.; Rong, X.; Ding, Z.; Fu, X.; Zeng, W.; Luo, L.; Wang, D.; Luo, Z.; et al. A Composite Hydrogel Functionalized by Borosilicate Bioactive Glasses and VEGF for Critical-Size Bone Regeneration. *Advanced Science* 2024, *11*, doi:10.1002/advs.202400349.
178. Zhang, F.; Zhou, L.; Zhou, Z.; Dai, C.; Fan, L.; Li, C.; Xiao, C.; Ning, C.; Liu, Y.; Du, J.; et al. Bioactive Glass Functionalized Chondroitin Sulfate Hydrogel with Proangiogenic Properties. *Biopolymers* 2019, *110*, doi:10.1002/bip.23328.
179. Lu, X.; Mestres, G.; Singh, V.; Effati, P.; Poon, J.-F.; Engman, L.; Ott, M. Selenium- and Tellurium-Based Antioxidants for Modulating Inflammation and Effects on Osteoblastic Activity. *Antioxidants* 2017, *6*, 13, doi:10.3390/antiox6010013.
180. Li, F.; Zhang, J.; Xiong, H.; Min, L.; Gou, L. Electrospun Photothermal Tellurium Nanosheet-Loaded Polycaprolactone/Gelatin Nanofibers to

Promote Wound Healing. *J Innov Opt Health Sci* 2024, doi:10.1142/S179354582442001X.

181. Du, S.; Huynh, T.; Lu, Y.-Z.; Parker, B.J.; Tham, S.K.; Thissen, H.; Martino, M.M.; Cameron, N.R. Bioactive Polymer Composite Scaffolds Fabricated from 3D Printed Negative Molds Enable Bone Formation and Vascularization. *Acta Biomater* 2024, *186*, 260–274, doi:10.1016/j.actbio.2024.07.038.
182. Lee, A.; Langford, C.R.; Rodriguez-Lorenzo, L.M.; Thissen, H.; Cameron, N.R. Bioceramic Nanocomposite Thiol-Acrylate PolyHIPE Scaffolds for Enhanced Osteoblastic Cell Culture in 3D. *Biomater Sci* 2017, *5*, 2035–2047, doi:10.1039/C7BM00292K.
183. Busby, W.; Cameron, N.R.; Jahoda, C.A.B. Emulsion-Derived Foams (PolyHIPEs) Containing Poly(ε-Caprolactone) as Matrixes for Tissue Engineering. *Biomacromolecules* 2001, *2*, 154–164, doi:10.1021/bm0000889.
184. Aldemir Dikici, B.; Malayeri, A.; Sherborne, C.; Dikici, S.; Paterson, T.; Dew, L.; Hatton, P.; Ortega Asencio, I.; MacNeil, S.; Langford, C.; et al. Thiolene- and Polycaprolactone Methacrylate-Based Polymerized High Internal Phase Emulsion (PolyHIPE) Scaffolds for Tissue Engineering. *Biomacromolecules* 2022, *23*, 720–730, doi:10.1021/acs.biomac.1c01129.
185. Du, S.; Huynh, T.; Lu, Y.-Z.; Parker, B.J.; Tham, S.K.; Thissen, H.; Martino, M.M.; Cameron, N.R. Bioactive Polymer Composite Scaffolds Fabricated from 3D Printed Negative Molds Enable Bone Formation and Vascularization. *Acta Biomater* 2024, *186*, 260–274, doi:10.1016/j.actbio.2024.07.038.
186. Bergoglio, M.; Najmi, Z.; Cochis, A.; Miola, M.; Vernè, E.; Sangermano, M. UV-Cured Bio-Based Acrylated Soybean Oil Scaffold Reinforced with Bioactive Glasses. *Polymers (Basel)* 2023, *15*, doi:10.3390/polym15204089.
187. Bergoglio, M.; Najmi, Z.; Cochis, A.; Miola, M.; Vernè, E.; Sangermano, M. Silanized and Cu-Doped Bioactive Glass as Filler for Biobased Photocurable 3D Printed Scaffolds. *Mater Today Chem* 2025, *44*, 102559, doi:10.1016/J.MTCHEM.2025.102559.
188. Bergoglio, M.; Kriehuber, M.; Sölle, B.; Rossegger, E.; Schlögl, S.; Najmi, Z.; Cochis, A.; Ferla, F.; Miola, M.; Vernè, E.; et al. 3D-Printed Acrylated Soybean Oil Scaffolds with Vitrimeric Properties Reinforced by Tellurium-Doped Bioactive Glass. *Polymers (Basel)* 2024, *16*, 3614, doi:10.3390/polym16243614.

189. Liu, S.; Mo, L.; Bi, G.; Chen, S.; Yan, D.; Yang, J.; Jia, Y.-G.; Ren, L. DLP 3D Printing Porous β-Tricalcium Phosphate Scaffold by the Use of Acrylate/Ceramic Composite Slurry. *Ceram Int* 2021, *47*, 21108–21116, doi:10.1016/j.ceramint.2021.04.114.
190. Yao, Y.; Sha, N.; Zhao, Z. Highly Concentrated Hydroxyapatite Suspension for DLP Printing. *IOP Conf Ser Mater Sci Eng* 2019, *678*, 012016, doi:10.1088/1757-899X/678/1/012016.
191. Rossegger, E.; Höller, R.; Hrbinič, K.; Sangermano, M.; Griesser, T.; Schlögl, S. 3D Printing of Soft Magnetoactive Devices with Thiol-Click Photopolymer Composites. *Adv Eng Mater* 2023, *25*, doi:10.1002/adem.202200749.
192. Hinczewski, C.; Corbel, S.; Chartier, T. Ceramic Suspensions Suitable for Stereolithography. *J Eur Ceram Soc* 1998, *18*, 583–590, doi:10.1016/S0955-2219(97)00186-6.
193. Melchels, F.P.W.; Feijen, J.; Grijpma, D.W. A Poly(d,l-Lactide) Resin for the Preparation of Tissue Engineering Scaffolds by Stereolithography. *Biomaterials* 2009, *30*, 3801–3809, doi:10.1016/j.biomaterials.2009.03.055.
194. Mondschein, R.J.; Kanitkar, A.; Williams, C.B.; Verbridge, S.S.; Long, T.E. Polymer Structure-Property Requirements for Stereolithographic 3D Printing of Soft Tissue Engineering Scaffolds. *Biomaterials* 2017, *140*, 170–188, doi:10.1016/j.biomaterials.2017.06.005.
195. Camargo, I.L. de; Morais, M.M.; Fortulan, C.A.; Branciforti, M.C. A Review on the Rheological Behavior and Formulations of Ceramic Suspensions for Vat Photopolymerization. *Ceram Int* 2021, *47*, 11906–11921, doi:10.1016/j.ceramint.2021.01.031.
196. Costa, B.N.L.; Adão, R.M.R.; Maibohm, C.; Accardo, A.; Cardoso, V.F.; Nieder, J.B. Cellular Interaction of Bone Marrow Mesenchymal Stem Cells with Polymer and Hydrogel 3D Microscaffold Templates. *ACS Appl Mater Interfaces* 2022, *14*, 13013–13024, doi:10.1021/acsami.1c23442.
197. Alhashimi, R.A.; Mannocci, F.; Sauro, S. Bioactivity, Cytocompatibility and Thermal Properties of Experimental Bioglass-Reinforced Composites as Potential Root-Canal Filling Materials. *J Mech Behav Biomed Mater* 2017, *69*, 355–361, doi:10.1016/j.jmbbm.2017.01.022.
198. Sauro, S.; Osorio, R.; Fulgêncio, R.; Watson, T.F.; Cama, G.; Thompson, I.; Toledano, M. Remineralisation Properties of Innovative Light-Curable Resin-Based Dental Materials Containing Bioactive Micro-Fillers. *J Mater Chem B* 2013, *1*, 2624, doi:10.1039/c3tb00205e.

199. Kargozar, S.; Mozafari, M.; Hill, R.G.; Brouki Milan, P.; Taghi Joghataei, M.; Hamzehlou, S.; Baino, F. Synergistic Combination of Bioactive Glasses and Polymers for Enhanced Bone Tissue Regeneration. *Mater Today Proc* 2018, *5*, 15532–15539, doi:10.1016/j.matpr.2018.04.160.
200. Dao, P.H.; Nguyen, T.C.; Phung, T.L.; Nguyen, T.D.; Nguyen, A.H.; Vu, T.N.L.; Vu, Q.T.; Vu, D.H.; Tran, T.K.N.; Thai, H. Assessment of Some Characteristics and Properties of Zirconium Dioxide Nanoparticles Modified with 3-(Trimethoxysilyl) Propyl Methacrylate Silane Coupling Agent. *J Chem* 2021, *2021*, 1–10, doi:10.1155/2021/9925355.
201. Nguyen, T.-C.; Nguyen, T.-D.; Vu, D.-T.; Dinh, D.-P.; Nguyen, A.-H.; Ly, T.-N.-L.; Dao, P.-H.; Nguyen, T.-L.; Bach, L.-G.; Thai, H. Modification of Titanium Dioxide Nanoparticles with 3-(Trimethoxysilyl)Propyl Methacrylate Silane Coupling Agent. *J Chem* 2020, *2020*, 1–10, doi:10.1155/2020/1381407.
202. Yao, Y.; Sha, N.; Zhao, Z. Highly Concentrated Hydroxyapatite Suspension for DLP Printing. *IOP Conf Ser Mater Sci Eng* 2019, *678*, 012016, doi:10.1088/1757-899X/678/1/012016.
203. Bejarano, J.; Caviedes, P.; Palza, H. Sol–Gel Synthesis and *in Vitro* Bioactivity of Copper and Zinc-Doped Silicate Bioactive Glasses and Glass-Ceramics. *Biomedical Materials* 2015, *10*, 025001, doi:10.1088/1748-6041/10/2/025001.
204. Raynaud, S.; Champion, E.; Bernache-Assollant, D. Calcium Phosphate Apatites with Variable Ca/P Atomic Ratio II. Calcination and Sintering. *Biomaterials* 2002, *23*, 1073–1080, doi:10.1016/S0142-9612(01)00219-8.
205. Shahabi, S.; Najafi, F.; Majdabadi, A.; Hooshmand, T.; Haghbin Nazarpak, M.; Karimi, B.; Fatemi, S.M. Effect of Gamma Irradiation on Structural and Biological Properties of a PLGA-PEG-Hydroxyapatite Composite. *The Scientific World Journal* 2014, *2014*, 1–9, doi:10.1155/2014/420616.
206. Bejarano, J.; Caviedes, P.; Palza, H. Sol–Gel Synthesis and *in Vitro* Bioactivity of Copper and Zinc-Doped Silicate Bioactive Glasses and Glass-Ceramics. *Biomedical Materials* 2015, *10*, 025001, doi:10.1088/1748-6041/10/2/025001.
207. Kapoor, S.; Brazete, D.; Pereira, I.C.; Bhatia, G.; Kaur, M.; Santos, L.F.; Banerjee, D.; Goel, A.; Ferreira, J.M.F. Impact of Transition Metal Ions on the Structure and Bioactivity of Alkali-Free Bioactive Glasses. *J Non Cryst Solids* 2019, *506*, 98–108, doi:10.1016/j.jnoncrysol.2018.12.003.
208. Kargozar, S.; Mozafari, M.; Ghodrat, S.; Fiume, E.; Baino, F. Copper-Containing Bioactive Glasses and Glass-Ceramics: From Tissue

Regeneration to Cancer Therapeutic Strategies. *Materials Science and Engineering: C* 2021, *121*, 111741, doi:10.1016/j.msec.2020.111741.
209. Ramesh, T. Osteogenic Differentiation Potential of Human Bone Marrow-derived Mesenchymal Stem Cells Enhanced by <scp>bacoside-A</Scp>. *Cell Biochem Funct* 2021, *39*, 148–158, doi:10.1002/cbf.3596.
210. Božić Cvijan, B.; Korać Jačić, J.; Bajčetić, M. The Impact of Copper Ions on the Activity of Antibiotic Drugs. *Molecules* 2023, *28*, 5133, doi:10.3390/molecules28135133.
211. Lallukka, M.; Miola, M.; Najmi, Z.; Cochis, A.; Spriano, S.; Rimondini, L.; Verné, E. Cu-Doped Bioactive Glass with Enhanced in Vitro Bioactivity and Antibacterial Properties. *Ceram Int* 2024, *50*, 5091–5103, doi:10.1016/j.ceramint.2023.11.253.
212. Bergoglio, M.; Reisinger, D.; Schlögl, S.; Griesser, T.; Sangermano, M. Sustainable Bio-Based UV-Cured Epoxy Vitrimer from Castor Oil. *Polymers (Basel)* 2023, *15*, doi:10.3390/polym15041024.
213. Goswami, A.; K, A.; Balashanmugam, N.; Umarji, A.M.; Madras, G. Optimization of Rheological Properties of Photopolymerizable Alumina Suspensions for Ceramic Microstereolithography. *Ceram Int* 2014, *40*, 3655–3665, doi:10.1016/j.ceramint.2013.09.059.
214. Mu, Q.; Wang, L.; Dunn, C.K.; Kuang, X.; Duan, F.; Zhang, Z.; Qi, H.J.; Wang, T. Digital Light Processing 3D Printing of Conductive Complex Structures. *Addit Manuf* 2017, *18*, 74–83, doi:10.1016/j.addma.2017.08.011.
215. Morgan, E.F.; Unnikrisnan, G.U.; Hussein, A.I. Bone Mechanical Properties in Healthy and Diseased States. *Annu Rev Biomed Eng* 2018, *20*, 119–143, doi:10.1146/annurev-bioeng-062117-121139.
216. Lee, J.; Cha, H. Do; Shim, J.; Jung, J.W.; Kim, J.Y.; Cho, D. Effect of Pore Architecture and Stacking Direction on Mechanical Properties of Solid Freeform Fabrication-based Scaffold for Bone Tissue Engineering. *J Biomed Mater Res A* 2012, *100A*, 1846–1853, doi:10.1002/jbm.a.34149.
217. Roshan-Ghias, A.; Lambers, F.M.; Gholam-Rezaee, M.; Müller, R.; Pioletti, D.P. In Vivo Loading Increases Mechanical Properties of Scaffold by Affecting Bone Formation and Bone Resorption Rates. *Bone* 2011, *49*, 1357–1364, doi:10.1016/j.bone.2011.09.040.
218. A, K.; A, L. Mechanical Behaviour of Skin: A Review. *Journal of Material Science & Engineering* 2016, *5*, doi:10.4172/2169-0022.1000254.
219. Earp, B.; Hubbard, J.; Tracy, A.; Sakoda, D.; Luhrs, C. Electrical Behavior of CNT Epoxy Composites under In-Situ Simulated Space Environments. *Compos B Eng* 2021, *219*, 108874, doi:10.1016/j.compositesb.2021.108874.

220. Zhang, S.; Luo, X.; Guo, C.; Huang, K.; Ding, S.; Li, L.; Zhou, C.; Li, H. Tissue Engineered Bone via Templated HBMSCs Mineralization and Its Application for Bone Repairing. *Biomaterials Advances* 2022, *139*, 212937, doi:10.1016/j.bioadv.2022.212937.
221. Turner, R.J.; Borghese, R.; Zannoni, D. Microbial Processing of Tellurium as a Tool in Biotechnology. *Biotechnol Adv* 2012, *30*, 954–963, doi:10.1016/j.biotechadv.2011.08.018.
222. Kumar, B.Y.S.; Isloor, A.M.; Kumar, G.C.M.; Inamuddin; Asiri, A.M. Nanohydroxyapatite Reinforced Chitosan Composite Hydrogel with Tunable Mechanical and Biological Properties for Cartilage Regeneration. *Sci Rep* 2019, *9*, 15957, doi:10.1038/s41598-019-52042-7.
223. Lemos, E.M.F.; Patrício, P.S.O.; Pereira, M.M. 3D NANOCOMPOSITE CHITOSAN/BIOACTIVE GLASS SCAFFOLDS OBTAINED USING TWO DIFFERENT ROUTES: AN EVALUATION OF THE POROUS STRUCTURE AND MECHANICAL PROPERTIES. *Quim Nova* 2016, doi:10.5935/0100-4042.20160047.
224. Islam, Md.M.; Shahruzzaman, Md.; Biswas, S.; Nurus Sakib, Md.; Rashid, T.U. Chitosan Based Bioactive Materials in Tissue Engineering Applications-A Review. *Bioact Mater* 2020, *5*, 164–183, doi:10.1016/j.bioactmat.2020.01.012.
225. Owen, R.; Sherborne, C.; Paterson, T.; Green, N.H.; Reilly, G.C.; Claeyssens, F. Emulsion Templated Scaffolds with Tunable Mechanical Properties for Bone Tissue Engineering. *J Mech Behav Biomed Mater* 2016, *54*, 159–172, doi:10.1016/j.jmbbm.2015.09.019.
226. McKenzie, T.J.; Ayres, N. Synthesis and Applications of Elastomeric Polymerized High Internal Phase Emulsions (PolyHIPEs). *ACS Omega* 2023, *8*, 20178–20195, doi:10.1021/acsomega.3c01265.
227. Kane, R.J.; Weiss-Bilka, H.E.; Meagher, M.J.; Liu, Y.; Gargac, J.A.; Niebur, G.L.; Wagner, D.R.; Roeder, R.K. Hydroxyapatite Reinforced Collagen Scaffolds with Improved Architecture and Mechanical Properties. *Acta Biomater* 2015, *17*, 16–25, doi:10.1016/j.actbio.2015.01.031.
228. Bejarano, J.; Caviedes, P.; Palza, H. Sol–Gel Synthesis and *in Vitro* Bioactivity of Copper and Zinc-Doped Silicate Bioactive Glasses and Glass-Ceramics. *Biomedical Materials* 2015, *10*, 025001, doi:10.1088/1748-6041/10/2/025001.
229. Lallukka, M.; Miola, M.; Najmi, Z.; Cochis, A.; Spriano, S.; Rimondini, L.; Verné, E. Cu-Doped Bioactive Glass with Enhanced in Vitro Bioactivity and

Antibacterial Properties. *Ceram Int* 2024, *50*, 5091–5103, doi:10.1016/j.ceramint.2023.11.253.

230. Mu, Q.; Wang, L.; Dunn, C.K.; Kuang, X.; Duan, F.; Zhang, Z.; Qi, H.J.; Wang, T. Digital Light Processing 3D Printing of Conductive Complex Structures. *Addit Manuf* 2017, *18*, 74–83, doi:10.1016/j.addma.2017.08.011.
231. Lebedevaite, M.; Gineika, A.; Talacka, V.; Baltakys, K.; Ostrauskaite, J. Development and Optical 3D Printing of Acrylated Epoxidized Soybean Oil-Based Composites with Functionalized Calcium Silicate Hydrate Filler Derived from Aluminium Fluoride Production Waste. *Compos Part A Appl Sci Manuf* 2022, *157*, 106929, doi:10.1016/j.compositesa.2022.106929.
232. Li, L.; Lu, P.; Liu, Y.; Yang, J.; Li, S. Three-Dimensional-Bioprinted Bioactive Glass/Cellulose Composite Scaffolds with Porous Structure towards Bone Tissue Engineering. *Polymers (Basel)* 2023, *15*, 2226, doi:10.3390/polym15092226.
233. Vilanova-Pérez, A.; De la Flor, S.; Fernández-Francos, X.; Serra, À.; Roig, A. Biobased Imine Vitrimers Obtained by Photo and Thermal Curing Procedures─Promising Materials for 3D Printing. *ACS Appl Polym Mater* 2024, *6*, 3364–3372, doi:10.1021/acsapm.3c03234.
234. Bergoglio, M.; Najmi, Z.; Ferla, F.; Scalia, A.C.; Cochis, A.; Rimondini, L.; Vernè, E.; Sangermano, M.; Miola, M. Tellurium-Doped Silanised Bioactive Glass–Chitosan Hydrogels: A Dual Action for Antimicrobial and Osteoconductive Platforms. *Polymers (Basel)* 2025, *17*, 1651, doi:10.3390/polym17121651.
235. Bergoglio, M.; Miola, M.; Vernè, E.; Sangermano, M.; Cameron, N.R. 3D-Printed Biobased Porous Polymer Scaffolds Reinforced with Bioactive Glasses by High Internal Phase Emulsion Polymerization. *Biomacromolecules* 2025, *26*, 8548–8559, doi:10.1021/acs.biomac.5c01413.